UNIVERSITAT POLITÈCNICA DE CATALUNYA BARCELONATECH

Multiscale mechanical and microstructural characterization of titanium and zirconium carbonitride hard coatings

Idriss El Azhari

Multiscale mechanical and microstructural characterization of titanium and zirconium carbonitride hard coatings

Idriss El Azhari

Department of Materials Science and Engineering,
Universitat Politècnica de Catalunya, BarcelonaTech, Spain

Part of
The Joint European Doctoral Programme in Materials Science and Engineering (DocMASE)
in collaboration with
Chair of Functional Materials (FuWe), Department of Materials Science, Saarland University, Germany

Thesis presented by compendium of publications

2019

بِسۡمِ ٱللَّهِ ٱلرَّحۡمَٰنِ ٱلرَّحِيمِ

﴿ٱقۡرَأۡ بِٱسۡمِ رَبِّكَ ٱلَّذِي خَلَقَ ١ خَلَقَ ٱلۡإِنسَٰنَ مِنۡ عَلَقٍ ٢ ٱقۡرَأۡ وَرَبُّكَ ٱلۡأَكۡرَمُ ٣ ٱلَّذِي عَلَّمَ بِٱلۡقَلَمِ ٤ عَلَّمَ ٱلۡإِنسَٰنَ مَا لَمۡ يَعۡلَمۡ ٥﴾

[سُورَةُ العَلَقِ: 1-5]

Preface

The work presented in this dissertation is the result of my doctoral studies within the frame of the Erasmus Mundus Joint European Doctoral Program in Materials Science and Engineering (DocMASE), between 2014 and 2019. Research activities were carried out at the Chair of Functional Materials (FuWe) at Saarland University (UDS, Saarbrücken, Germany), at the Center for Structural Integrity, Reliability and Micromechanics of Materials (Ciefma) at Universitat Politècnica de Catalunya (UPC, Barcelona, Spain), and in a close collaboration with AB Sandvik Coromant (Stockholm, Sweden).

The results of this dissertation are published in peer-review scientific journals, which are appended at the end of this manuscript.

Idriss EL AZHARI,

Saarbrücken, 2019

Abstract

The present dissertation is an in-depth investigation from the macro to atomic scale of industrial wear-resistant CVD hard coatings deposited on cemented carbides for cutting tool applications. Micro-compression tests at the micro-scale and contact damage induced by means of millimetric spherical indentation were deployed to study deformation mechanisms of two systems consisting of a defined cemented carbide substrate coated with two different films: Ti(C,N) and Zr(C,N). The latter system exhibited a superior tool life in comparison to the conventional Ti(C,N) one. Several characterization techniques were used: confocal microscopy, scanning electron microscopy, focused ion beam, electron back scattered diffraction, X-ray synchrotron and atom probe tomography.

It was found that remnant structural integrity related to the absence of an extensive cracking network for Zr(C,N) - in the as deposited state - is one of the main reasons that could explain better performance in interrupted cutting. Adapted coefficient of thermal expansion toward the substrate, plastic deformation and better cohesive strength at the grain boundaries (which renders more toughness) are factors that contribute not only to this preserved structural integrity but also to the extended tool life during in-service interrupted cutting.

Resumen

En esta tesis doctoral se presenta una investigación extensa y detallada, desde la escala macroscópica hasta la atómica, de recubrimientos industriales - duros y resistentes al desgaste - depositados por CVD sobre carburos cementados para su aplicación como herramientas de corte. El estudio se realizó en dos sistemas recubiertos empleando diferentes capas cerámicas - Ti(C,N) y Zr(C,N) - pero sin variar el carburo cementado empleado como sustrato. Los mecanismos de deformación de ambos sistemas se evaluaron mediante ensayos de micro-compresión de pilares, así como de indentación esférica (con bolas de radios milimétricos), estos últimos buscando inducir daño de forma controlada a nivel superficial y subsuperficial. El sistema recubierto con la capa de Zr(C,N) exhibió una vida útil superior al más convencional - Ti(C,N). El estudio incluyó la implementación de varias técnicas de caracterización: microscopía confocal, microscopía electrónica de barrido, haz de iones focalizados, difracción de electrones retrodispersados, sincrotrón de rayos X, y tomografía con sonda atómica.

Se encontró que la elevada integridad estructural remanente relacionada con la ausencia de fisuración interconectada en el caso de Zr(C,N) – justo después de ser depositado – es alguna de las principales razones para explicar el mayor rendimiento de este sistema recubierto en operaciones de mecanizado que involucran corte interrumpido. La adecuación del coeficiente de expansión térmica, relativo al que exhibe el sustrato, la capacidad de absorber deformación plástica, y la relevante resistencia cohesiva en los bordes de granos (lo que proporciona una mayor tenacidad) son factores que contribuyen no sólo a preservar la integridad estructural,

sino también a prolongar la vida útil de la herramienta durante condiciones de servicio que conlleven corte interrumpido.

Zusammenfassung

Die vorliegende Dissertation ist eine eingehende Untersuchung vom makro- bis zu der atomaren Skala von industrieller verschleißfester CVD-Hartschichten auf Hartmetallschneidwerkzeugen abgeschieden. Mikrodruckversuche und Kontaktschädigung ausgelöst durch millimetergenaue Kugel Eindruck wurden eingesetzt, um Verformungsmechanismen von zwei Systemen, bestehend aus einem definierten Hartmetallsubstrat, das mit zwei verschiedenen Schichten beschichtet ist: Ti(C,N) und Zr(C,N). Letzteres System zeigt eine höhere Standzeit als das herkömmliche Ti(C,N). Es wurden eine Vielzahl von Charakterisierungstechniken eingesetzt: Konfokale Mikroskopie, Rasterelektronenmikroskopie, fokussierter Ionenstrahl, Elektronenrückstreubeugung, Synchrotron und Atomsonden-Tomographie.

Es wurde festgestellt, dass die erhaltene strukturelle Integrität in Bezug auf das Fehlen eines ausgedehnten Rissnetzwerks für Zr(C,N) - im abgeschiedenen Zustand - einer der Hauptgründe ist, der die bessere Leistung beim unterbrochenen Schnitt Verfahren erklären könnte. Angepasste Wärmeausdehnungskoeffizienten entgegen das Substrat, plastische Verformung und bessere Korngrenzen-Kohäsion (was zu mehr Zähigkeit führt) sind Faktoren, die nicht nur zu dieser erhaltenen strukturellen Integrität beitragen, sondern auch zu einer verlängerten Standzeit beim Fräsen im Einsatz.

Included papers

Paper 1: Investigations on micro-mechanical properties of polycrystalline Ti(C,N) and Zr(C,N) coatings

I. El Azhari, J. García, M. Zamanzade, F. Soldera, C. Pauly, L. Llanes, F. Mücklich, Acta Materialia. 149 (2018) 364–376. https://doi.org/10.1016/j.actamat.2018.02.053

Paper 2: Atom Probe Tomography investigations on grain boundary segregation in polycrystalline Ti(C,N) and Zr(C,N) CVD coatings

I. El Azhari, J. Barrirero, J. García, F. Soldera, L. Llanes, F. Mücklich, Scripta Materialia. 162 (2019) 335–340. https://doi.org/10.1016/j.scriptamat.2018.11.041

Paper 3: Micromechanical investigations of CVD coated WC-Co cemented carbide by micropillar compression

I. El Azhari, J. García, M. Zamanzade, F. Soldera, C. Pauly, C. Motz, L. Llanes, F. Mücklich, Materials & Design. 186 (2020) 108283. https://doi.org/10.1016/j.matdes.2019.108283

Paper 4: Contact damage investigation of CVD carbonitride hard coatings deposited on cemented carbides

I. El Azhari, J. García, F. Soldera, S. Suarez, E. Jiménez-Piqué, F. Mücklich, L. Llanes, International Journal of Refractory Metals and Hard Materials. 86 (2020) 105050. https://doi.org/10.1016/j.ijrmhm.2019.105050

In the papers listed above, I. El Azhari led the design and planning of the experimental activities, performed all the mechanical testing and carried out most of the characterization investigations, conducted the analysis and discussion of the results and finally wrote all the manuscripts.

Abbreviations

AD: Angle dispersive

Al_2O_3: Aluminium oxide / Alumina

APT: Atom probe tomography

B1: Rock salt structure

BEKD: Backscatter electron Kikuchi diffraction

BKD: Backscatter Kikuchi diffraction

BSE: Backscattered electrons

C_2H_2: Acetylene.

CH_3CN: Acetonitrile

CH_4: Methane

Cl: Chlorine

CLSM: Confocal laser scanning microscopy

Co: Cobalt

CTE: Coefficient of thermal expansion

CVD: Chemical vapor deposition

EBSD: Electron backscattered diffraction

EDDI: Energy dispersive diffraction

EDS: Energy dispersive X-ray spectrometer

Fcc: Face centered cubic

FEG: Field emission gun

FEM: Finite element modeling

FIB: Focused ion beam

Ga: Gallium

Hf: Hafnium

HT-CVD: High temperature CVD

IBAD: Ion beam activated deposition

ISE: Ion induced secondary electrons

LMIS: Liquid metal ion source

LP-CVD: Low pressure CVD

LT-CVD: Low temperature CVD

MO-CVD: Metalorganic CVD

MT-CVD: Moderate temperature CVD

N_2: Dinitrogen

NaCl: Sodium chloride

Nb: Niobium

NH_3: Ammonia

O_2: Oxygen.

OIM: Orientation image microscopy

PA-CVD: Plasma assisted CVD

PE-CVD: Plasma enhanced CVD

PVD: Physical vapor deposition

SE: Secondary electrons

SEM: Scanning electron microscope

SPM: Scanning probe microscopy

STEM: Scanning transmission electron microscope

Ta: Tantalum

TaC: Tantalum carbide

TEM: Transmission electron microscope

Ti(C,N): Titanium carbonitride

TiAlN: Titanium Aluminium Nitride

TiC: Titanium carbide

$TiCl_x$: Titanium subchloride

TiN: Titanium nitride

TKD: Transmission Kikuchi diffraction

TMC: Transition metal carbides

TMCN: Transition metal carbonitrides

TMN: Transition metal nitrides

UHTC: Ultra high temperature ceramics

VEC: Valence electron concentration

WC: Tungsten carbide

XEC: X-ray elastic constant

Zr(C,N): Zirconium carbonitride

Zr: Zirconium

ZrC: Zirconium carbide

ZrN: Zirconium nitride

Acknowledgement

By the culmination of what could be called a “journey”, which is at the same time long when referring back to the first day, but also extremely quick considering personal impressions and feelings, I feel the responsibility to express my gratitude to all the people that were of help and great support during this “journey”.

In this regard I would like to express my gratitude to my first supervisor at UDS Prof. Frank Mücklich, who accepted, welcomed and believed in me since the first day. I appreciated his charisma and tact sense which are exemplary for an outstanding leader. I also want to thank my second supervisor at UPC Prof. Luis Llanes for accepting me being one of his doctorate students in his research group. I sincerely wondered his humility, vision and his continuous and unrestricted help, especially during the finalization stages of the thesis.

My candid and huge acknowledgment goes as well to the duo Dr. Flavio Soldera and Dr. José García with whom everything started since the “video-call” interview. Your efforts, contribution and consistent assistance in many aspects were very decisive for the completion of the present project. I want to thank enormously also my nice colleagues in the chair of functional materials (FuWe) for the scientific unfading backup and aid: Dr. Christoph Pauly, Dr. Jeni Barrirero, Dr. Sebastian Suaréz and Sebastian Slawik. I want to thank my scientific supervisor Prof. Christian Motz and his co-workers, especially Dr. Mohammad Zamanzade, for the support and discussions in micromechanics field. I also feel indebted to Dr. Jaafar Ghanbaja (Université de Lorraine) for the considerable TEM workload that unfortunately could not be included in the present dissertation.

Besides, I would like to thank also my office mates and friends for the nice company: Chia-Jui Hsu (aka Ray), Sebastian Slawik (aka SeB), Kai Rochlus and my “office neighbor” Jiaqi Luo. Many thanks to the wonderful workmates - including the “Kicker” team - at FuWe and Eusmat (Saarland University), and at Ciefma group (Universitat Politècnica de Catalunya) that made this “journey” such an enjoyable time.

The European union is acknowledged for funding the exceptional Erasmus Mundus Doctoral Program: DocMASE, and the exchange project CREATe-Network. Remarkable thanks go to the manager of these programs: Dr. Flavio Soldera.

My exchanges and visits to Sandvik Coromant were a real pleasure, then I would like to express my appreciation to the organization for the financial and material assistance. I would not forget dedication, kindness and friendship of the staff, especially from my industrial supervisor (or “El Jefe”): Dr. José García.

Finally, endorsement and encouragement of my family was the driving force, couple of words cannot express my deep-down consideration and indebtedness to their colossal care and sacrifices to bring us to the stage where we stand now.

Above all, I would like to address my deepest gratitude to God for the blessing, protection and guidance through this long journey.

Table of contents

1. Introduction

Continuous enhancement of productivity, reduction of manufacturing costs and upgrading capabilities of the products are three vital pillars for sustainable corporations in nowadays fierce competitive environment. For the metal cutting industry, this mainly relies on the increase of the cutting speed (and/or the feed rate), which leads to accelerated tool wear as a result of increasing temperatures, mechanical loads and oxidation rate [1]. Then, development of reliable new tools that have extended service life and can withstand these severe service conditions is a key factor for achieving this target. In this regard, although they were introduced a century ago, cemented carbides (also referred to as hardmetals) have been established as leading materials in very demanding applications like cutting and forming of metallic alloys. The reason behind is the excellent combination of hardness, toughness and wear-resistance that they exhibit. Besides their mechanical properties, cemented carbides are widely tunable by selecting the appropriate microstructural parameters, i.e. WC grain size, metallic binder volume fraction, alloying, gradients, etc. [2]. Since the late 60s, the successful deposition of few micrometers thick hard coatings onto cemented carbides as external protective layers, has driven the performance and service life of the tools to a superior level (more than 100 times service life improvement [3,4]). As a consequence, the majority of tools used for metal cutting are coated [5–7]. Therefore, the optimization of such tribological coatings is nowadays a key strategy for increasing manufacturing process efficiency [8].

The introduction of coatings to metal cutting applications started with the deposition of TiC monolayer by chemical vapor deposition (CVD) [9]. Since then, more

complex multilayer assemblies have been designed, new deposition routes have been developed (particularly physical vapor deposition (PVD)) and innovative compounds have been proposed and validated (TiN, Ti(C,N), TiAlN, Al_2O_3, etc.) [6,7,10]. Majority of these coatings are generally based on carbon and/or nitrogen in a solid solution (ordered phase) with transition metal element(s) which provides these compounds a unique hybrid combination of ceramic- and metal-like properties. Moreover, continuously rising performance has been achieved by the introduction of new transition metal compounds together with microstructural design adopting different strategies (i.e. texture control, grain boundary engineering, residual stress development, etc.).

Within the above described framework, by changing exclusively the chemical nature of the carbonitride layer, a recently developed Zr(C,N)/Al_2O_3 multilayer CVD coated milling insert has shown extended tool life in comparison to the established Ti(C,N)/Al_2O_3 coated inserts [11]. This finding may be considered somehow surprising, as the respective mechanical and physical properties of Ti(C,N) and Zr(C,N) are quite comparable [12,13]. It is then the scope of the present thesis to conduct an in-depth investigation and comparison of these carbonitride coatings by means of mechanical testing and microstructural characterization at different length scales: bulk, microstructural and atomic. Besides, not only the intrinsic and isolated properties of the coatings are studied but also their respective interaction and deformation with the substrate. The major goals are to reveal different failure mechanisms of the intermediate carbonitride coating, the corresponding critical properties and their resulting impact on the assemblage (i.e. association with the substrate) that makes cutting tools with Zr(C,N) hard coating a superior system (for interrupted cutting) in comparison to the conventional Ti(C,N) system counterpart.

This thesis is organized into four main chapters. In the first one, state of the art of transition-metal compounds, hard coatings and deposition processes related to the study will be introduced. The second chapter presents characterization and testing techniques deployed in the investigations. Afterwards, results and discussions are given as a summary of articles, where connection and interrelation between these studies is addressed. Finally, the last chapter is devoted to the conclusions and future works. A graphical outline of the thesis is presented in Figure 1-1. More details of the papers' scope and interrelation is given in section 4.1.

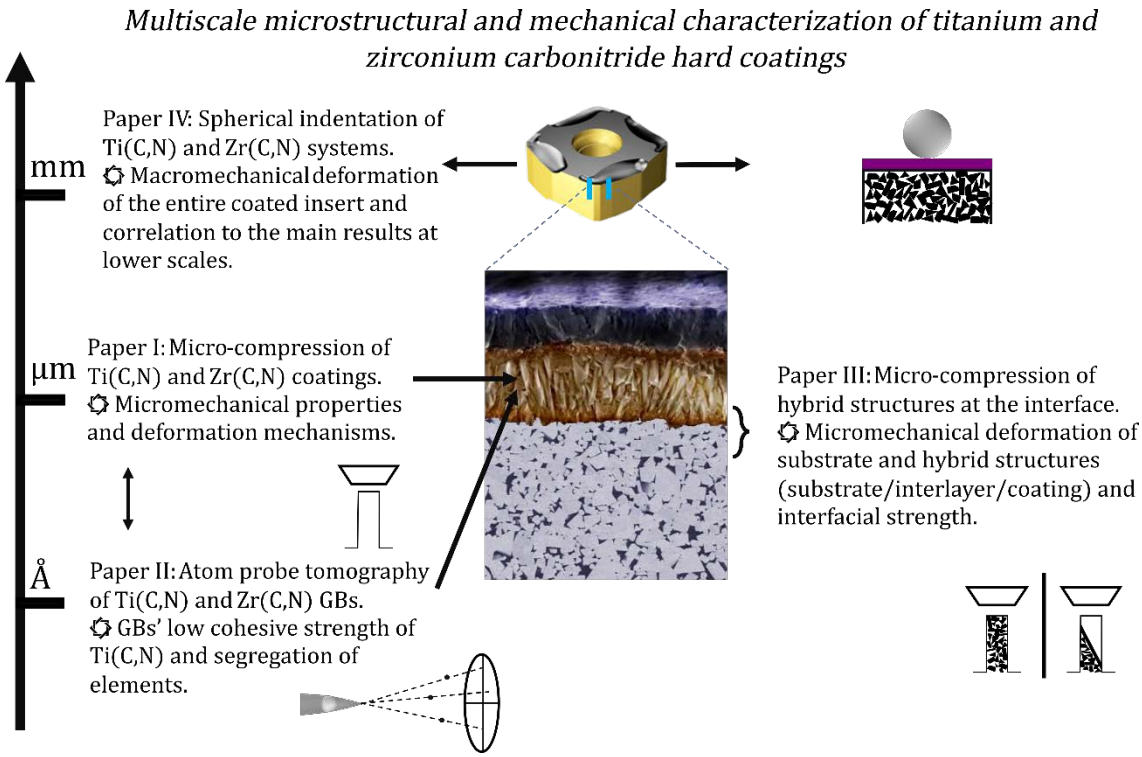

Figure 1-1: Graphical outline of the thesis arranged as cumulative dissertation of papers: paper I [14], paper II [15], paper III [16] and paper IV [17]. (Images of insert and cross section are adapted from Sandvik Coromant).

2. State of the art

2.1 Preamble

Hard coatings used in the metal cutting industry are based on the metal transition compounds. This section will present first an outline of the special properties of transition metal carbonitrides compounds with a focus on the materials concerned (titanium and zirconium carbonitride). Afterwards, development of hard coatings and deposition techniques related to metal cutting industry is given.

2.2 Transition metal carbonitrides

2.2.1 Overview

Transition metal carbides (TMC), nitrides (TMN) and carbonitrides (TMCN) are compounds that combine physical properties of both ceramics (high hardness and stiffness, thermal and chemical stability) and metals (electrical and thermal conductivity, metallic glare). These hybrid properties are attributed to a complex mixture of covalent, ionic and metallic atomic bonding [5]. As a result, these compounds have been deployed in various technological applications: metal cutting operations as wear-resistant protective coatings [5–7], microelectronics industry (diffusion barriers, interconnectors, etc.) [18,19], nuclear reactors [20–22] and aerospace applications [23,24].

The initial report on the synthesis of these materials dates back to the end of the 19th century where synthesis of ZrC was reported for the first time by Moissan and Lengfeld [25]. Then, after more than half a century, studies on single crystalline

and sintered transition-metal carbides have skyrocketed from the 60s until the 80s, due to the race to space and the quest for materials performing at extreme conditions [24]. The focus was on studying the mechanical properties and plasticity at high temperature of these compounds [26–35], since they possess outstanding potential in extreme environment such as aerospace and metal cutting. Later on, since the late 90s, it was understood that different hybrid properties (ceramic- and metal-like) for this class of materials are generally more related to their electronic structures and atomic bonding than to their crystal structure. Consequently, with the boost of computing capabilities, extensive fundamental research based on first principles calculations has been conducted to explain their mechanical and physical properties [36–46].

TMCs and TMNs are closely related in crystal structure type, phase relationship, bonding characteristics, and electrical and magnetic properties [47]. Often these carbides and nitrides form solid solutions resulting in transition metal carbonitrides [5]. Lattice structure of these compounds may be described as close packed or nearly close-packed arrangements of metal atoms with smaller non-metal atoms located in the interstitial cites. For most of the structures, non-metal atoms are isolated and there is no apparent bonding between them [47]. Depending on the application, the two main synthesis routes of these materials are through either powder metallurgy or vapor deposition (for thin layers).

2.2.2 Mechanical properties

Although TMCs, TMNs and TMCNs exhibit outstanding mechanical properties regarding hardness, strength and stiffness, the limiting factor for these compounds to be deployed for broader applications is their intrinsic brittleness and failure through

cracking. The brittleness at room temperature is attributed to limited or absence of dislocation activity. However, at high temperatures, it is generally found that TMCs undergo a brittle to ductile transition, and deforms in a similar manner to the fcc (face centered cubic) metals [47,48], as a result of the thermal activation of additional slip systems. Recently, Kiani et al. have proven by means of in-situ compression in a transmission electron microscope (TEM) that TaC and ZrC single crystals can deform plastically at room temperature through dislocation motion along two active slip systems [44,49]. However, it must be noted that in order to experience extensive plastic deformation in bulk polycrystalline materials, a minimum of five independent slip systems are necessary for compatibility of the strain transfer between different oriented crystals (Von Mises criterium). For technical ceramics, different strategies have been implemented to tackle the brittleness issue: microstructural design, fiber or ductile phase reinforcement, grain boundary engineering, extrinsic toughening mechanism, multilayered assemblage, etc. In the last two decades, new strategies based on first principles calculations have been established for transition metal compounds to tune their mechanical properties. For TMCNs it was reported that by balancing C and N ratios in order to obtain a valence electron concentration (VEC) of about 8.4 per cell, maximum hardness is obtained as a result of creation of strong atomic bonding that resists to shearing [36]. Oppositely, to enhance the ductility of the TMNs while maintaining hardness, specific alloying elements are introduced in order to maximize the VEC (≥ 10) which results in lowering of the shear resistance and promotion of dislocation glide [50–52].

2.2.3 Thermal properties

One of the key advantages of TMCs, TMNs and TMCNs compounds is that their excellent properties, such as high hardness and chemical resistance, do not deteriorate considerably at high temperatures. Moreover, several TMCs and TMNs (based on Zr, Hf, Nb, and Ta) compounds belong to the group referred to as ultrahigh temperature ceramics (UHTC), i.e. materials exhibiting the highest melting points of any known compounds [24,53] (Figure 2-1). This class of materials are binary compounds in which an early transition metal, such as Zr, Hf, Ti, Nb, and Ta, is combined with carbon, nitrogen or boron [24].

Thermal expansion of these compounds is a critical parameter as they are practically not used in a standalone manner but in association with other materials [5]. As an example, upon the thermal load, dissimilar coefficient of thermal expansion between transition metal compound coating and a given substrate can cause structural damage of the assemblage. Generally, the coefficient of thermal expansion of these alloys is higher than the parent transition metal [5]. Concerning thermal conductivity, it is substantially higher than those usually reported for ceramic oxides. Unexpectedly, it is even reported that the thermal conductivity of TMC increases with rising temperature which is a peculiar phenomenon [5]. It is important to emphasize that titanium-, zirconium- and hafnium- carbides, nitrides and carbonitrides can be melted without decomposition [5]. Besides, the corresponding carbides and more generally transition metal monocarbides of the IVB and VB groups can be indeed melted congruently [5].

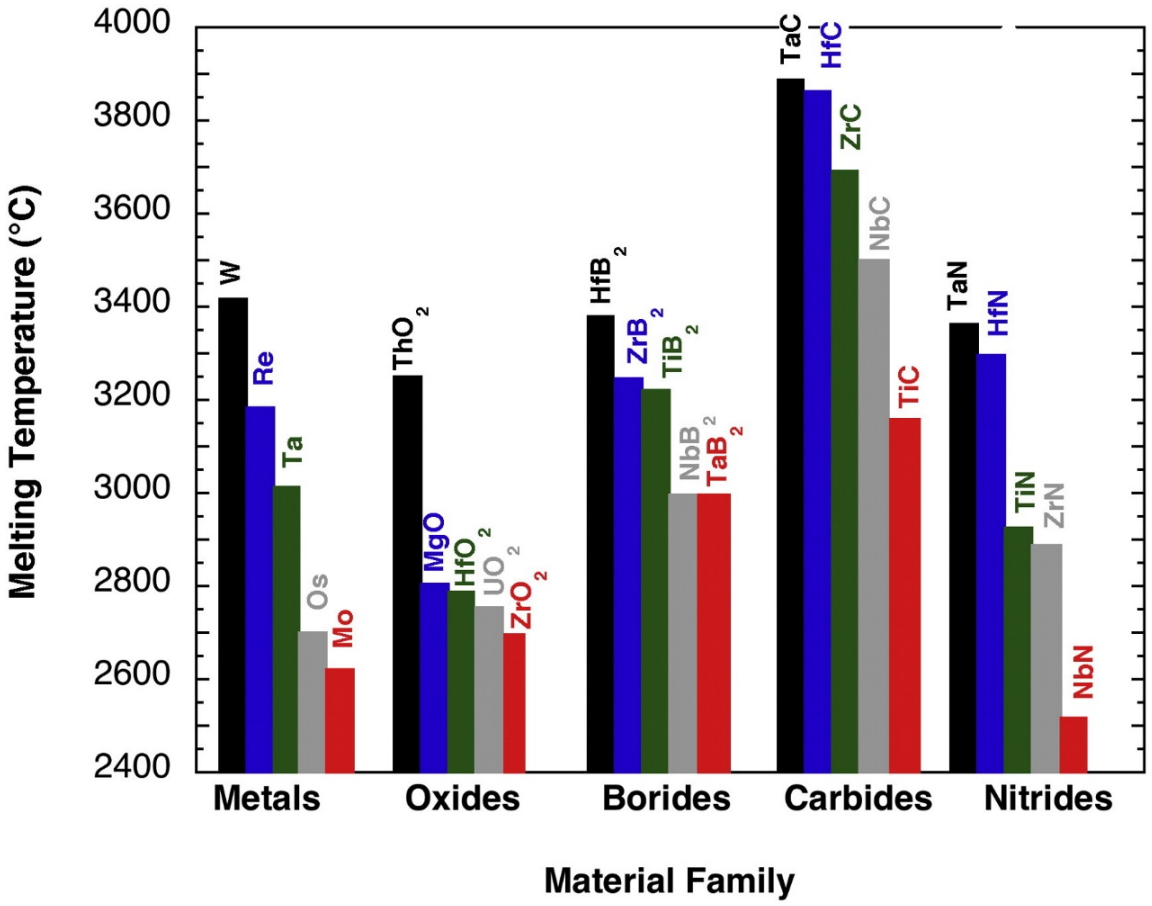

Figure 2-1: A comparison of the melting temperatures of the most refractory members of several classes of materials. Several borides, carbides, and nitrides have melting temperatures above 3000 °C and are considered ultra-high temperature ceramics. For comparison, the melting temperature of Zr is ~ 1850 °C and the melting temperature of Hf is ~2227 °C. (Taken from [54]).

2.2.4 Titanium carbonitride Ti(C,N)

Solid solution of titanium carbide (TiC) and titanium nitride (TiN) forms titanium carbonitride (Ti(C,N)). Similarly to its corresponding nitrides and carbides, $Ti(C_x,N_{1-x})$ compound is crystallized in a NaCl B1 crystal lattice, with $Fm\bar{3}m$ as the corresponding space group. From another perspective, this can be viewed as a titanium face centered cubic (fcc) with carbon and nitrogen occupying the octahedral sites randomly (Figure 2-2). The solid-state properties are tunable with variation of

[C]/[C]+[N] ratio, offering a large field for tailoring these compounds [5]. Moreover, over the entire range of concentration ($0 \leq x \leq 1$), the formation energy (Gibbs free energy) is favorable for a complete miscibility of TiC and TiN, with a minimum value of this energy located between $0.5 < x < 0.75$ [38]. Titanium based carbonitrides are conventionally used as the hard phase for cermets composites also known as Ti(C,N) hardmetals [2]. Their microstructure is characterized by core-rim structure embedded in a tough metal binder. Besides, Ti(C,N) is used widely as wear-resistant hard coating for cutting tools, and it is one of the most used coating materials [55]. The main reason is the remarkable thermo-mechanical resistance of Ti(C,N) compared to traditional TiN and TiC hard coatings, which then supported its implementation in metal cutting industry [56]. Adjustment of the C/N ratio enables tuning the properties of Ti(C,N) from high hardness and low friction of TiC to relative high toughness and chemical stability of TiN [41,57].

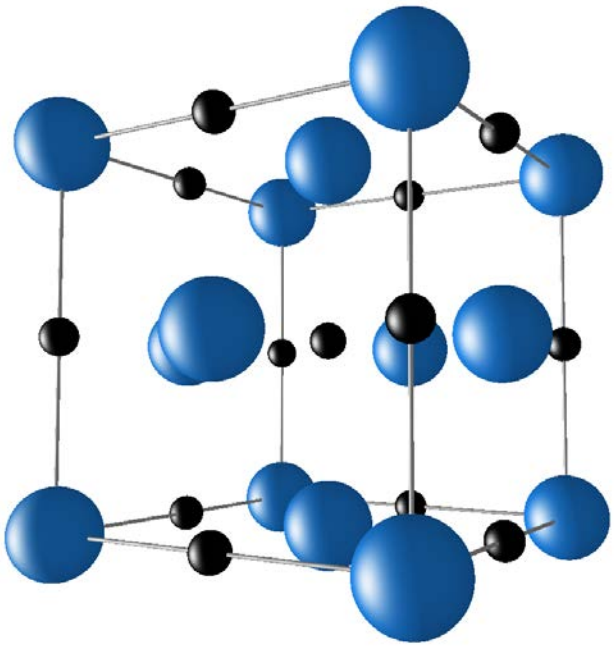

Figure 2-2: Rock salt crystal structure of Ti/Zr(C,N): metal atoms (large blue spheres) and carbon/nitrogen atoms (small dark spheres).

2.2.5 Zirconium carbonitride Zr(C,N)

Similarly to Ti(C,N), Zr(C,N) is a solid solution of zirconium carbide (ZrC) and zirconium nitride (ZrN). The crystal lattice and space group are similar to Ti(C,N) [58]. Likewise, formation energy for $Zr(C_x,N_{1-x})$ indicates complete miscibility between ZrC and ZrN in the entire concentration range and a minimum value of this energy between $0.5 \leq x \leq 0.6$ [39].

Considering that titanium and zirconium are successive elements in the fourth group, their respective compounds have generally similar physical properties. Zirconium based compounds are used as an alternative to the respective titanium

based ones due to the enhanced high temperature durability and chemical stability [46], corrosion resistance [59,60], and better tribological properties [61–64].

Opposite to Ti(C,N), applications and studies of Zr(C,N) are limited. It has been used for tribological applications [65,66] and as wear-resistant coating in metal cutting applications [5,63,67]. Nevertheless, there is a recognition that Zr(C,N) is a promising material in highly demanding applications [5,46,67], and may provide coatings that outperform the current Ti(C,N) coating used [53]. Table 1 reports some physical values of titanium and zirconium compounds.

*Table 1: Physical properties of Ti/Zr carbonitrides. Values without a corresponding reference are taken from [5]. Underlined values are extracted from curves. (*It was reported by Agte et al. that melting temperature of $Ti(C_{0.5},N_{0.5})$ is 45° higher than TiC [68]).*

Ti/Zr compound	*Pearson symbol*	*Lattice parameter (Å)*	*density (g cm⁻³)*	*Melting point (°C)*	*Nano-hardness (GPa)*	*Young modulus (GPa)*	*Heat cond. (W m⁻¹ K⁻¹)*	*Thermal expansion (10^{-6} K⁻¹)*	*Electrical resistivity (μΩ cm)*
TiC	cF8	4.328	4.93	3067	31.7 [13]	450	28.9	8.5	100
TiN	cF8	4.242	5.39	3050	19.4 [13]	420	29	9.9	27
$Ti(C_{0.5},N_{0.5})$	cF8	4.286 [69]	5.15 [70]	3112* [68]	26.5 [13]	463 [13]	-	9.2 [71]	52.5 [12]
ZrC	cF8	4.7	6.46	3420	27.6 [13]	350	24.6	7.5	75
ZrN	cF8	4.57	7.32	3000	18.9 [13]	460	11	7.8	24
$Zr(C_{0.5},N_{0.5})$	cF8	4.625 [69]	6.95 [72]	-	24.4 [13]	405 [13]	22.2 [12]	7.7 [71]	50 [12]

2.3 Hard coatings for metal cutting

2.3.1 Metal cutting

Metal cutting operations can be divided into three main groups: drilling, turning and milling. The latter operation has the largest cutting tools market share [7]. However, it is the most demanding application, as metal cutting is performed with a revolving multi-edged cutting tool in which each cutting insert is subjected to considerable thermo-mechanical cycling, accelerating the wear and reducing the overall tool life.

Generally, conditions under which the cutting tool is subjected are extreme: tools are under a combination of huge thermal loading (up to 1200 °C [73]), very large mechanical stresses (in the order of a couple of GPas [6]) and harsh chemical environment due to oxidation and corrosion (when lubrication is used). For this purpose, several micrometers thick hard layers are deposited on the cutting tools for protection against this aggressive environment. Consequently, load-bearing capacity is enhanced and huge thermal flux which causes plastic deformation of the cutting edge is reduced. An example of this improvement is presented in Figure 2-3.

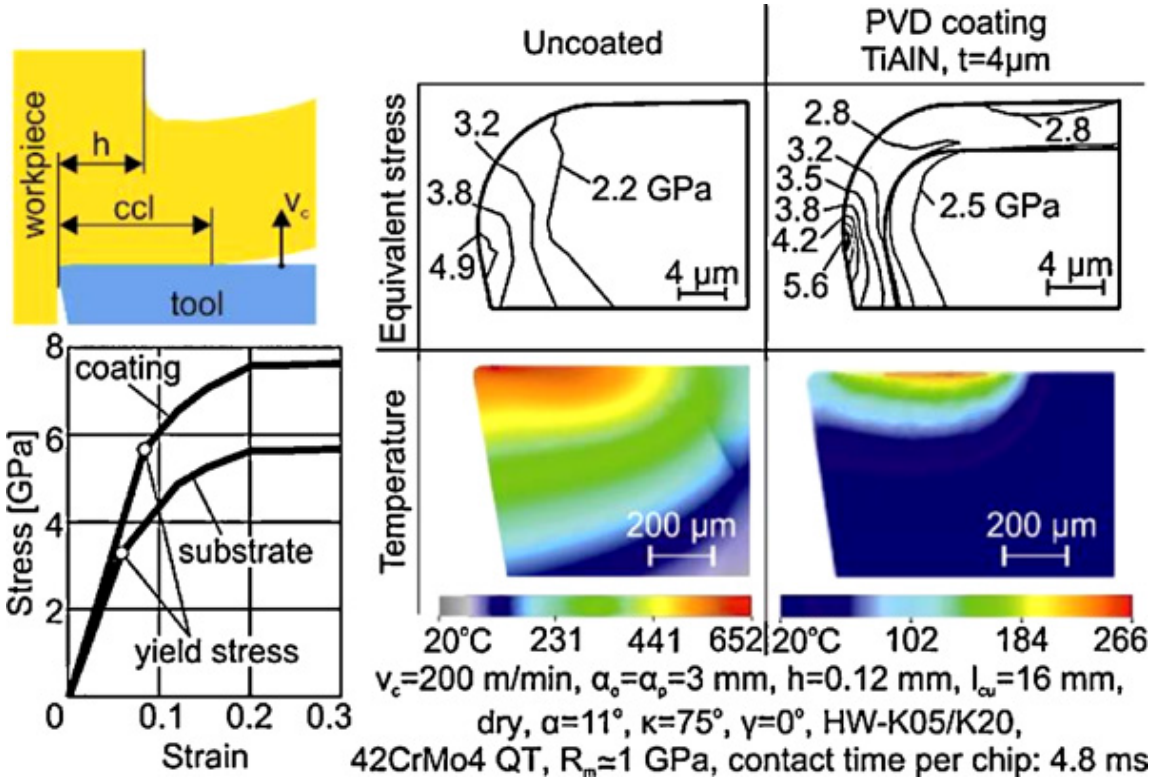

Figure 2-3: Decrease of mechanical and thermal loads of cemented carbide tools in milling by the application of PVD-coatings. (Taken from [6]).

2.3.2 Coatings development

Introduction of coatings to cemented carbide tools dates from the late 1960s, when TiC was deposited on a hardmetal through the CVD process for turning applications [9,10,73]. Back then, 2-3 µm thick coating enhanced not only tool life twice, but also reduced cutting forces, friction and vibrations, in comparison to the corresponding uncoated tool [73]. In 1973, a remarkable breakthrough in service life was achieved by multilayer design which permitted an improvement of up to 1000% [73]. Nearly ten years later, PVD coatings were introduced to the market which initially started with - and until today mainly based on - TiN compounds [6]. Later on,

additional multilayer coating strategies have been adopted to functionalize and tune properties of the coatings. As an example, for CVD coatings (Figure 2-4), Al_2O_3 outer layer is deposited as a thermal barrier which mitigates both high heat flux generated during cutting and adhesive wear. Ti(C,N,O) ensures a very good adhesion and anchoring between Zr(C,N) and alumina layer. Thin TiN starting interlayer (between the substrate and the coating) is deposited to promote nucleation of the carbonitride film, to act as a diffusion barrier layer and to improve adhesion to the substrate. Nowadays, although the literature is abundant on other various investigated compounds, TiN, Ti(C,N), Al_2O_3 and TiAlN coatings - which were introduced back in 1970s and 1980s - remain the most used coatings in cutting tools [7]. Majority of hard coating deployed in metal cutting industry are deposited either by CVD or PVD (Figure 2-5).

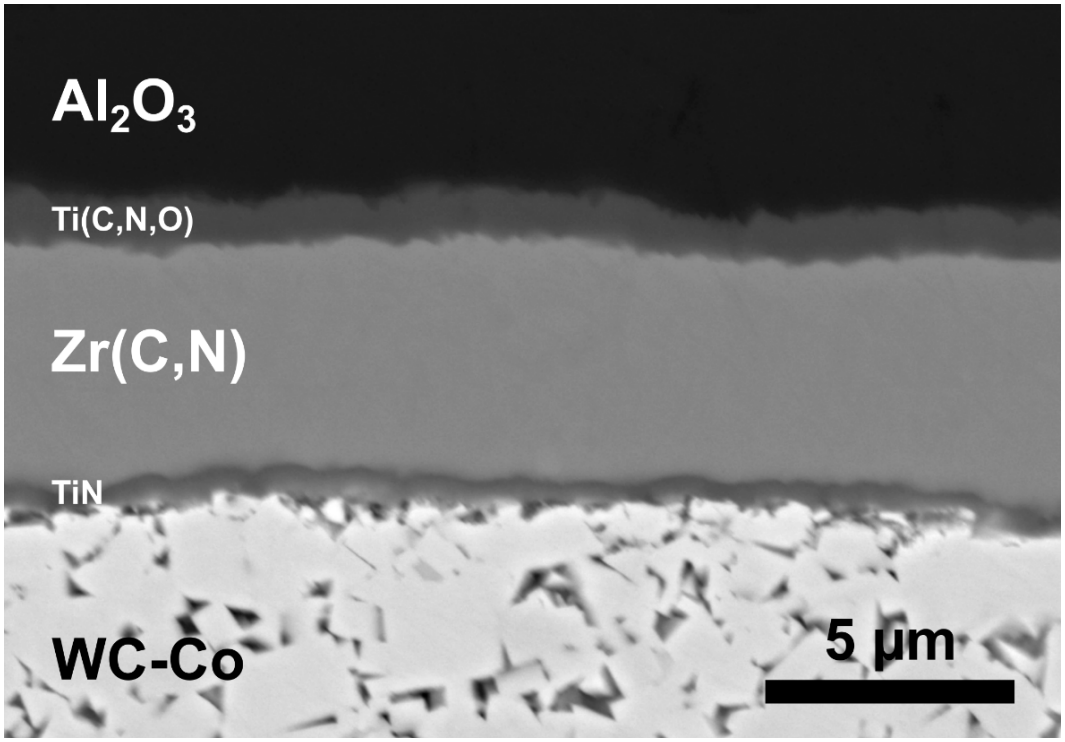

Figure 2-4: Cross section of a CVD coated milling cutting insert showing the different layers deposited on the WC-Co substrate [16].

In addition to the substrate, improvement of tool life and performance depends on tailoring the intrinsic and extrinsic properties of the coatings to comply with requirements of the metal-cutting process. Through the years, constant optimization of the microstructure, compounds and phases, interfaces and multilayer design has permitted outstanding extension of tool life service to more than 100 times in comparison to uncoated counterparts [3,4].

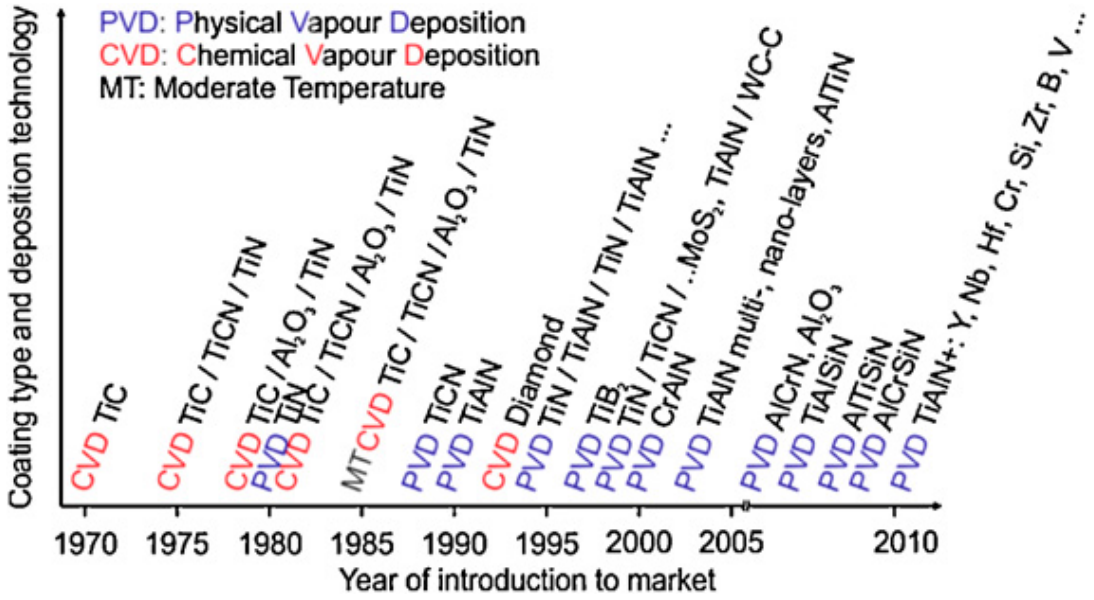

Figure 2-5: Evolution of coating materials for cutting tools. Nowadays, CVD AlTiN has become a trend since its introduction in the market in 2011 [74]. (Taken from [6]).

2.3.3 Deposition processes

2.3.3.1 Physical vapor deposition (PVD)

Physical vapor deposition features a large group of vacuum based coating deposition processes in which the base material is physically extracted from a source (called the target) [6]. For hard coatings, reactive processes are used where a reactive gas is introduced (N_2, O_2, C_2H_2) to react with the produced material base vapor to form

the desired compound. The consolidated coatings are away from the thermodynamic equilibrium and are characterized by a high density of defects which yields high hardness, compressive stresses, and metastable phases [75].

2.3.3.2 Chemical vapor deposition (CVD)

Chemical vapor deposition could be defined as the deposition of a solid through vapor chemical reactions which are activated on a heated substrate [76]. The process was developed during the 19th century for incandescent lamps by coating filament wires with carbon or metals to increase their life time [77]. As mentioned before, the process was scaled to metal cutting inserts in 1969 with the deposition of TiC on cemented carbides.

For transition metal compounds, the deposition is a thermally activated reaction between gas precursors containing the metal base (e.g. halides) and carbon, nitrogen or oxygen source gas. Different compounds can be formed depending on the mixtures of gases. Two types of reactors can be distinguished: hot-wall reactor where the whole system is heated, and cold-wall reactor where only the substrate is heated. The former technique is well suited for mass production by batch processing, as a large number of substrates can be coated simultaneously [4].

Reactions which form solid products (or powder) between precursors in the gas phase are qualified as homogeneous nucleation. However, this reaction is usually detrimental to the process (formation of unwanted complexes, consumption of precursors) as the objective is to initiate a heterogenous reaction on the substrate (Figure 2-6).

The CVD process is atomistic in nature, i.e. deposition species are molecules or atoms or a combination of them [76]. Consequently, exact mechanisms occurring at

the molecular or atomic scale for crystal formation affecting grain size and texture are complex and still not completely understood. Generally, two regimes are proposed depending on the rate-limiting step: surface kinetics controlled and mass transport controlled. In the latter, diffusion of precursors from the laminar gas to the surface is slower than the reaction of species adsorption at the surface. Oppositely, with higher temperature and lower pressure, diffusion is increased and layer thickness is decreased which shifts the regime to a surface kinetics one [75]. Surface kinetics controlled regime provides a more uniform deposition within the coating [75]. Control of the coating microstructure (which is affecting its properties directly) has been done through trial and error adjustment of precursors' partial pressures and temperature.

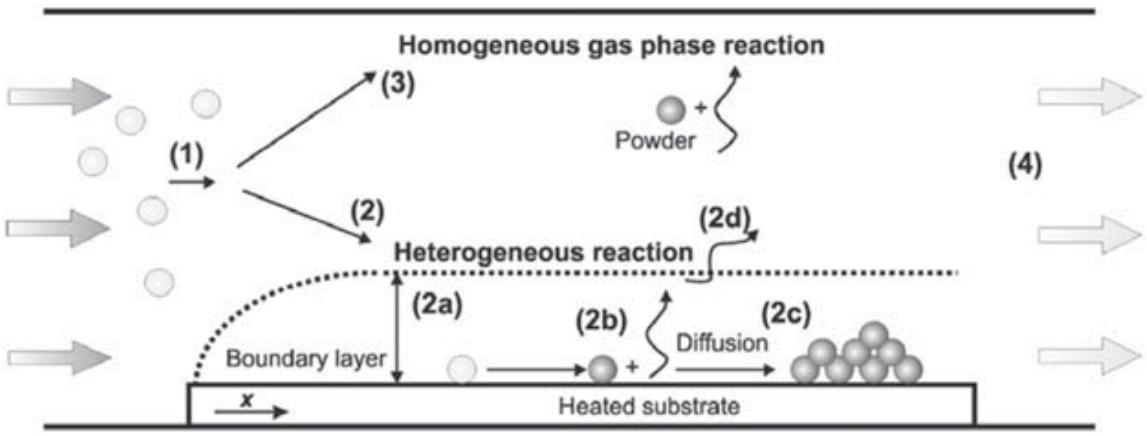

Figure 2-6: Schematic illustration of the basic process steps involved in CVD: gas feed (1), heterogeneous reaction (2), homogeneous reaction (3), and gas exhaust (4). The heterogeneous reaction comprises transport of the reactants through the boundary layer and adsorption (2a), chemical reactions at the substrate surface (2b), nucleation and growth (2c), and desorption of by-products (2d) (Redrawn after Spear (1982) [78] and Choy (2003) [79]). (Taken from [75]).

Transition-metal based CVD processes can be divided into three main groups:

- High temperature CVD (HT-CVD). It can be described as the first-generation process. The relatively high deposition temperature (950-1150 °C [75]) prohibited its use for a large number of substrates (e.g. high-speed steel). Even for cemented carbides, this range of temperature causes diffusion of substrate elements during crystal growth which affects the deposition processes [10]. Moreover, high temperatures can cause decarburization of the substrate which can result in the formation of a brittle carbon deficient tungsten carbide, called Eta-phase ($M_{6,12}C$ with M=W,Co) at the substrate-coating interface. Thus, toughness and performance of the cutting tool are negatively affected.

- Moderate temperature CVD (MT-CVD). The use of acetonitrile (CH_3CN) as a carbon and nitrogen source reduced the deposition temperature (700-900 °C [80]) due to its higher reactivity in comparison to other sources, like N_2 and CH_4. Besides, C/N ratio is maintained constant for the deposited compound [81]. As a result, HT-CVD was replaced by MT-CVD for the deposition of Ti(C,N). Consequently, formation of the brittle Eta-phase could be strongly reduced [80–82].

- Low temperature CVD (LT-CVD). Lower deposition temperatures (below 750 °C) could be achieved mainly by three methods. The first one is by reaction activation through plasma assisted (or enhanced) process (PA/PE-CVD). The second one is by introducing ammonia (NH_3) as a nitrogen source [83–91] with - usually - low pressure in the CVD chamber [84–90]. This process is known as low pressure CVD (LP-CVD) and it is extensively used in microelectronics industry. The third method is by using decomposable precursors at lower temperature like metalorganic and organometallic precursors (MO-CVD) [92,93]. These processes have some shortcomings like

impurity incorporation and low deposition rates for MO-CVD [64], and chlorine contamination (when using chloride containing precursors) at lower deposition temperatures for PA-CVD and LP-CVD.

2.3.3.3 Physical vapor deposition vs chemical vapor deposition

Advantages of PVD over CVD can be summarized as:

- Lower deposition temperatures (450 – 550 °C [6]) which allows its use for a broad range of substrates sensible to higher temperatures.

- Compressive stresses instead of tensile stresses, which is crucial for interrupted cutting operations like milling.

- Environmental issues related to the use of the vapor halide precursors and the resulting by-products, which are often hazardous and toxic.

In contrast, CVD permits deposition of thicker coatings with higher deposition rates, large-scale production and better interfacial adhesion. More importantly, homogenous thickness can be obtained even for complex geometries, as the precursors react on the preheated substrate regardless of the geometry, opposite to PVD where the deposition is directional to the target (line-of-sight deposition).

3. Experimental procedure

3.1 Materials

The investigated coated hardmetal specimens were provided by AB Sandvik Coromant. The coatings were deposited on cemented carbide substrates in an industrial hot-wall CVD reactor. These samples can be divided into two main groups: Ti(C,N) and Zr(C,N). The only difference between these two groups is the chemical nature of the carbonitride wear-resistant layer. Following paragraphs in this section will provide generalities and basics about the mechanical testing methods and characterization techniques used in this study. More details about the specimens and equipment parameters can be found in the related papers I [14], II [15], III [16] and IV [17].

3.2 Testing

3.2.1 Micro-compression testing

Since the introduction of micro-compression technique by Uchic et al. in 2004 [94], the use of experimental micro-/nanomechanical testing has been boosted. This method has been used mainly to study single crystals in terms of slip systems involved in plastic deformation, plasticity size-effects [94–96] and dislocation interactions at bi-crystalline grain boundaries as well [97,98]. In a few studies, this technique has been extended to investigate the deformation of brittle materials and thin hard coatings [99–106]. Although nanoindentation is the most widespread method to characterize mechanical properties of thin hard layers, investigation of deformation

mechanics from the residual imprint is a challenging task. The main reason behind is that multi-axial stresses and strains generated during contact loading are complex [107,108]. In this regard, micro-compression emerges as a more adapted method for such micromechanical characterization, considering the relative uniform stress distribution [108] and the ease of processing micropillars. Micropillar compression could eventually be used for evaluating mechanical properties such as elastic modulus and yield stress. However, special care has to be given to the experimental shortcomings which can corrupt the resulting data [109].

In the present study, micro-compression tests are carried out ex-situ with the aid of a Hysitron Tribo-Indenter Ti 900 equipped with a Performech controller and a 5 µm diamond flat punch. In-situ scanning probe microscopy (SPM) of the pillar using the flat punch as a probe is possible with the Piezo-scanner which is coupled to the transducer. Maximum load that can be actuated by the transducer is around 35 mN. A displacement-controlled loading function was chosen for all the experiments.

Micropillar specimens were produced using a FEI Helios Nanolab DualBeam 600 SEM/FIB (Scanning electron microscope/Focused ion beam). Successive annular milling steps were conducted to achieve the final shape of the pillar with an aspect ratio (diameter/height) of 1/3. More details about the SEM/FIB equipment are given in section 3.3.2. Micropillar compression method was implemented in paper I [14] and paper III [16].

3.2.2 Spherical indentation testing

Spherical indentation was deployed to study “macromechanical” deformation behavior of the entire coated system. Damage scenarios resulting from contact loading on wear-resistant CVD hard coatings deposited on the hardmetal substrate

were analyzed and documented in paper IV [17]. Damage is introduced in a controlled manner by means of a blunt indenter (spherical) which permits applying concentrated stresses over a small area of the specimen surface, such that damage evolution with increasing applied load can be assessed. This experimental approach has proven to be successful in the evaluation of contact damage mechanisms in hard and brittle bulk materials [110–112], as well as in coating-substrate systems, mainly PVD-coated hardmetals and tool steels [113–117].

In paper IV [17], the tests were conducted using a servo-hydraulic testing machine (Instron 8500) and a hardmetal indenter with a curvature radius (r_{sph}) of 1.25 mm. Monotonic loads were applied using a trapezoidal waveform.

3.3 Characterization

3.3.1 Confocal microscope

Confocal laser scanning microscopy (CLSM) is a microscopic optical imaging technique that delivers 3D images of surfaces with high spatial and - particularly - depth resolution, in comparison to classical imaging techniques. In contrast to conventional optical microscope systems, CLSM uses a focused sharp beam which scans the surface of the sample point by point in a raster way. Multiple lateral (X,Y) images are obtained at different focus length which permits to construct 3D images. The name “confocal” originates from the use of a confocal optical system. It is based on the employment of a pinhole in front of the image detector that filters flare or out-of-focus light (emerging from above and below the focal plane [118]). This pinhole is confocally positioned to the illuminated spot of the sample surface (Figure 3-1). This confocal arrangement noticeably enhances image contrast [118].

In the present investigation an Olympus OLS4100 was used with a semiconductor laser of 405 nm wavelength. Height and lateral resolutions down to 10 nm and 120 nm, respectively, can be reached. CLSM was used to image damage and cracking induced by spherical indentation in paper IV [17].

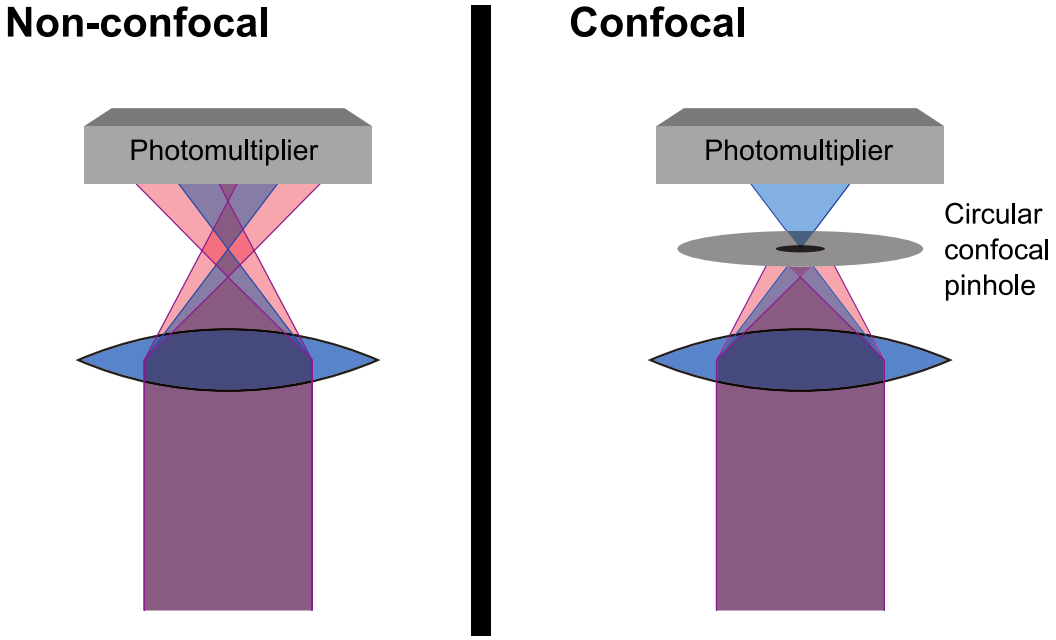

Figure 3-1: Difference between non-confocal and confocal optical systems. The use of pinhole is blocking the blur. (Image taken from the Olympus OLS4100 brochure).

3.3.2 Scanning electron microscope (SEM) and focused ion beam (FIB)

The FEI Helios Nanolab DualBeam 600 is a workstation that combines both scanning electron microscope (SEM) and focused ion beam (FIB). The present equipment can be qualified as the backbone of the present study, as it is used for both characterization (or analysis) and sample preparation.

3.3.2.1 Scanning electron microscope

Scanning electron microscopy is based on the electron-matter interaction, which results in various signals that can be exploited beyond topographical imaging, e.g. chemical composition analysis, phase analysis and crystal orientation. Electrons are emitted from an electron source (Thermionic, Field emission gun (FEG)) and are accelerated through a specific system of apertures and electromagnetic lenses. The generated electron beam penetrates a couple of micrometers into the surface of the sample, and interacts with the atoms producing secondary electrons (SE), backscattered electrons (BSE), X-rays, etc. (Figure 3-2).

Generally, secondary and backscattered electrons are used for imaging, where the former delivers topographic contrast and the latter gives both topographical and higher chemical contrast. Chemical composition is obtained using energy dispersive X-ray spectrometer (EDS) which is coupled to the SEM.

Due to the small wavelength of the electron beam, quite a high resolution (around 1 nm) can be obtained [119]. This has permitted achieving high image resolution by scanning the sample surface with the electron beam. The resolution can be greatly enhanced by subjecting the sample to a strong magnetic field (immersion mode) which improves focusing of the beam and increases the resolution. The ultimate lateral resolution of the SEM depends on the diameter of the electron beam [119]. Scanning transmission electron microscope can be conducted in a SEM, and is usually referred to as STEM-in-SEM. This can be realized by mounting of a special STEM detector under an ultra-thin lamella sample which is transparent to high voltage electron beam (~ 30 kV). STEM detector is an important tool that expands the capabilities of SEM systems [120].

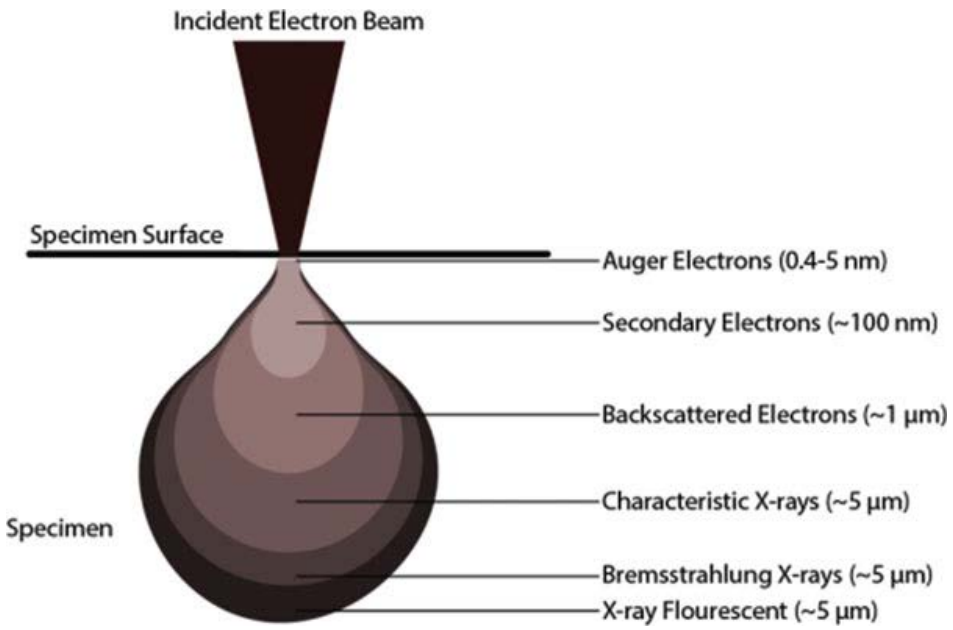

Figure 3-2: Schematic illustrating the formation of teardrop interaction volume upon scattering of the electron beam within the specimen. The probe diameter of a few nanometers results in several cubic micrometers of volume from where signals are generated. This limits the spatial and analytical resolution of the SEM. (Taken from [121]).

3.3.2.2 Focused ion beam

FIB uses similar principle as the SEM. However, ions are operated instead of the electrons. Ions are produced from a liquid metal ion source (LMIS), which guaranties high brightness and focusing capabilities. The most common LMIS is gallium (Ga) as a consequence of its low melting temperature (30 °C), low volatility and electrical properties.

As a result of their mass, ions are used for milling the material to produce cross sections, thin foils for TEM or machining of structures with micrometric dimensions. Gas-injection modules that react with gallium ions enables enhanced etching (for specific materials) and ion beam activated deposition (IBAD) (e.g. platinum deposition).

FIB can also be used for imaging, as secondary electrons are produced during interaction of the ions with sample atoms. These electrons are known as ion induced secondary electrons (ISE). However, since ions have a strong interaction with the crystal atoms, contrast mechanisms of generation of these electrons are different from SE. ISEs provide additional channeling contrast, giving information about crystal orientation and phase [122]. Nevertheless, longer exposure time and higher current are destructive, as sputtering of the material surface becomes important. Besides, Ga incorporation (or contamination) either for imaging or milling is a non-negligible shortcoming of this technique [123].

Most of contemporary FIB systems are coupled with SEM (dual-beam equipment) where FIB column is tilted with a certain angle to the vertical SEM column (Figure 3-3).

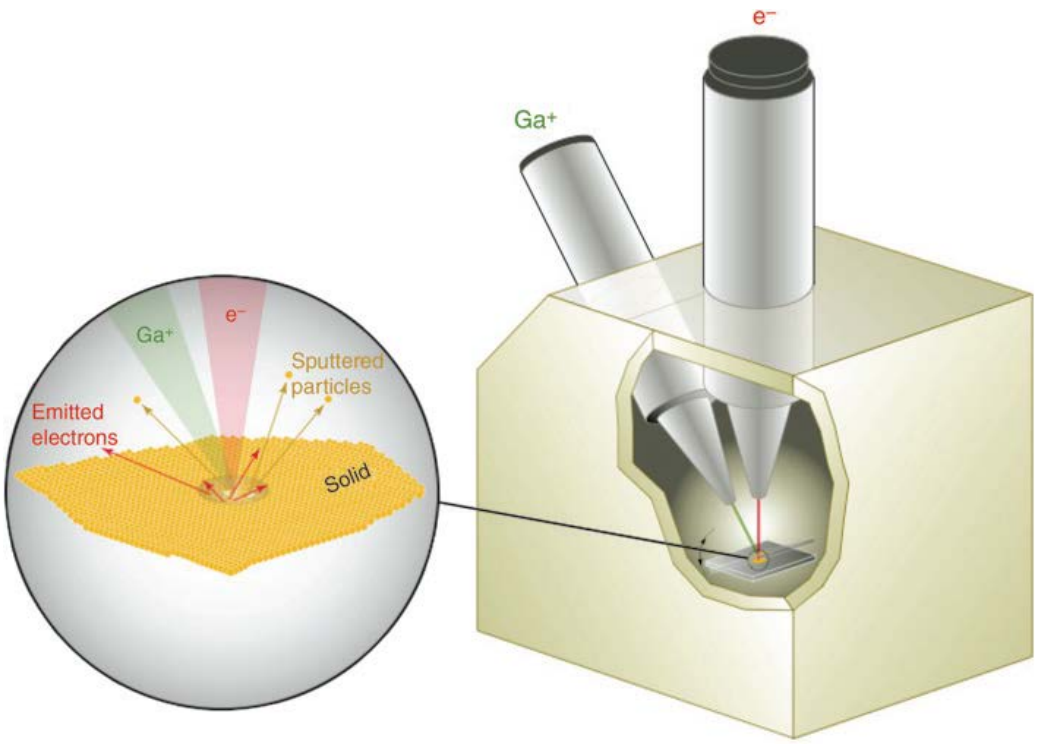

Figure 3-3: Schematic illustration of a dual-beam FIB–SEM instrument. Expanded view shows the electron and ion beam sample interaction. (Taken from [122]).

3.3.3 Electron back scattered diffraction

Electron backscattered diffraction (EBSD) is a powerful image orientation technique which is performed through a dedicated detector (or camera) coupled to a SEM. This technique permits crystallographic characterization of crystalline materials through scanning of an electron beam of the sample surface which gives in each scan point a corresponding EBSD pattern [124]. In addition to the orientation of crystals, other features of grains such as texture, phase nature identification and strain in individual grains can be obtained.

This method is based on backscatter diffraction of an electron beam with a crystal lattice plane. It produces two diffracting electron cones for each plane which are projected on a phosphor screen. The corresponding intersection generates a pattern which is known as Kikuchi band. As multiple diffractions are occurring from different crystal planes, the resulting bands give rise to Kikuchi patterns (e.g. Figure 3-4). The angles between Kikuchi bands correspond to interplanar angles, and the width of the bands is related to the interplanar spacing. EBSD is also known as backscatter Kikuchi diffraction (BKD) or backscatter electron Kikuchi diffraction (BEKD) [125]. The first observation of a diffraction pattern in backscattering mode dates back to 1928 by Nishikawa and Kikuchi [126].

EBSD systems are automated and consist of three main units: the SEM, the pattern acquisition device (or camera) and a dedicated software. The main role of the software is first the detection of the patterns (with Hough transformation), and then their subsequent indexation by comparison of the measured angles and interplanar distances with crystals' theoretical values. Unlike SEM, spatial resolution of EBSD is not related to the diameter of the electron beam but rather to the resulting interaction

volume which generates the patterns. This interaction volume is a function principally of the accelerating voltage, the specimen density and the tilt toward the electron beam [125]. Nevertheless, even if it reduces the resolution, the specimen is tilted to increase yield of the backscattered electrons leaving the sample [124]. EBSD patterns could also be obtained in transmission, which offers a higher spatial resolution [124]. However, in that case, thin foil specimen is necessary. This technique is called transmission Kikuchi diffraction (TKD).

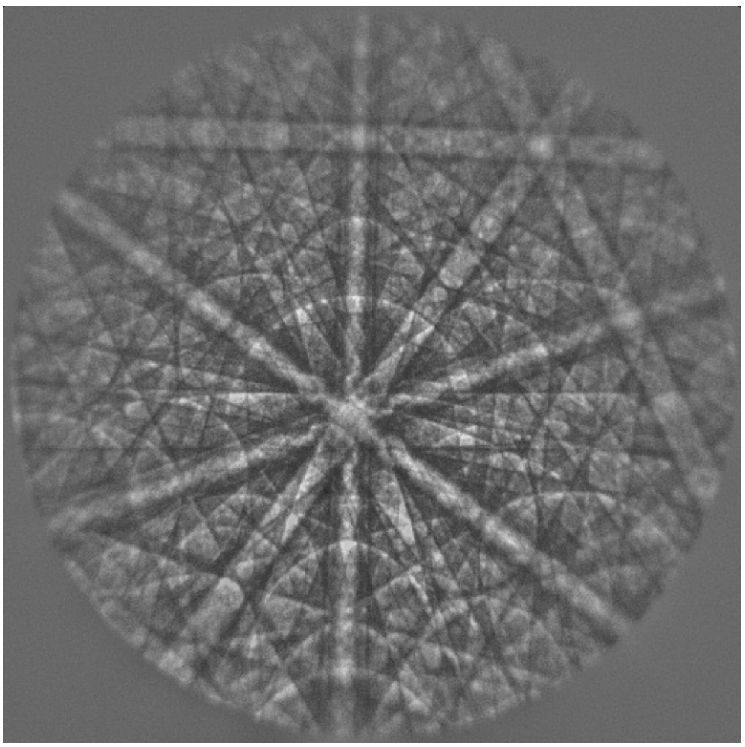

Figure 3-4: Kikuchi patterns at 20 kV of Zr(C,N) grain from the studied polycrystalline thin coating.

An EBSD scan can be used to analyze plastic strain by the calculation of a local misorientation within pixel grains. As dislocations are generated in the material, residual strain is translated in variations in lattice orientations. Then local misorientations give an indication of the strain distribution in the material [127]. Nevertheless, it should be highlighted that EBSD is a surface sensitive technique.

Hence, for a successful measurement, careful surface preparation is necessary as the damage induced on the surface due to the preparation degrades strongly the quality of the EBSD patterns [127].

EDAX Hikari system - associated with the same FEI Helios Nanolab DualBeam 600 - was used. Raw data were processed with OIM Analysis™ v7 software. EBSD was used in paper I [14] to check the polycrystalline microstructure and map the strain in the crystals. Furthermore, it was utilized in paper III [16] to investigate the microstructural phase assemblage and check slip systems in WC phase.

3.3.4 Atom probe tomography

Atom probe tomography (APT) is a powerful technique which enables three-dimensional chemical analyses at the atomic scale. APT combines one of the principles of field ion microscopy (which is a projection type microscope with atomic resolution) with a time of flight spectrometer (which is related to the chemical nature of the elements) [128]. However, in contrast to field ion microscopy, ions of the samples are evaporated in a high vacuum chamber. Samples have to be prepared in order to have a needle-shaped geometry with an apex radius of 50-100 nm. The volume that can be analyzed is in the order of $100 \times 100 \times 300$ nm^3. FIB has become a standard technique for samples preparation through wedge lift-out method [129].

The APT chamber is held at ultra-high vacuum (pressure lower than 1.33×10^{-8} Pa) and the stage is cooled down to cryogenic temperatures. To produce the required electrostatic field, a high electrical voltage is applied between the specimen and a counter-electrode placed in front of the latter. To induce the evaporation of atoms from the surface, two possible modes can be applied: either high-voltage pulses or laser pulses. In voltage mode, the counter-electrode is connected to a negative high-

voltage pulser, while in the laser mode, a pulsed laser is focused on the specimen apex (Figure 3-5). Then, upon the electrostatic high-voltage and the pulsed excitation (which is either voltage or laser pulses), atoms of the surface are progressively evaporated and collected by a (x,y) position-sensitive and time-resolved detector [130,131]. Recorded time-of-flights of the different ions are converted to mass-to-charge ratios which are represented in the form of a histogram called mass spectrum. This mass spectrum is directly related to the chemical nature of the element [130,131]. Finally, the 3D reconstruction is performed with a dedicated software using as an input the (x,y) recorded positions, arrival sequence order of the ions for z position and the analyzed chemical nature. For more details on the reconstruction method, an exhaustive description can be found in reference [132].

A local electrode atom probe LEAP™ 3000X HR was used in the present study in laser mode. The datasets were reconstructed and analyzed with the IVAS™3.6.14 software (CAMECA). APT was carried out to highlight potential element (or phase) segregations at grain boundaries of carbonitrides coatings (Ti(C,N) and Zr(C,N)). Details about the experimental parameters are given in paper II [15].

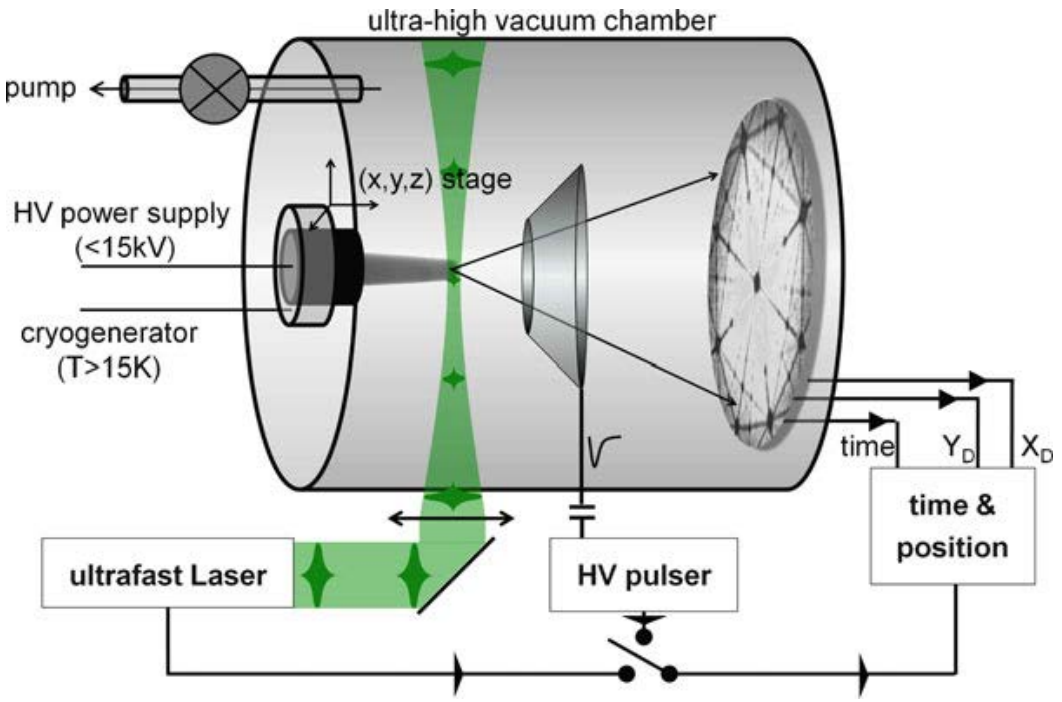

Figure 3-5: Experimental setup for atom probe tomography. Counter-electrode (CE) is linked to the HV pulser which applies nanosecond rise time voltage pulses causing field evaporation of surface atoms towards the position sensitive detector (PSD). Pulsed laser which focused on the sample apex can be used as well for atom evaporation. (Taken from [130]).

3.3.5 X-ray synchrotron

A synchrotron can be described generally as a cyclic particle accelerator which produces radiation. This synchrotron radiation is produced through deflection (or deceleration) of accelerated particles via a magnetic field. Hence, this radiation is also known as “Magnetobremsstrahlung". When electrons are accelerated fast enough, X-ray radiation can be generated as a result of the deflection. Then X-ray synchrotron is defined as a powerful source of bright and intense X-rays which are produced by acceleration and constant deflection (through different types of magnets) of high energy electrons circulating in a closed loop, known as “storage ring”. The latter is composed of a set of focusing and deflection magnets that circulate the electrons

inside the ring track. The produced radiation is redirected and collected by what is called “beamlines” that surround the storage ring. Each beamline is designed for a specific research area; hence, a particular diffractometer assembly.

The main advantage of using energy dispersive (ED) diffraction offered by the synchrotron, instead of the angle dispersive (AD) available with conventional X-ray diffractometers, is the mode of data recording [133]. In the ED approach, a complete diffraction spectrum with a multitude of reflections can be obtained in a fixed position (for both sample and detector) and within a couple of seconds. This property offers additional testing possibilities. Moreover, smaller beam divergence provides higher resolution strain profiling [133].

In the present study, residual stresses were measured by means of ED X-ray diffraction with synchrotron radiation. It was performed at the Material Science Beamline EDDI (Energy dispersive diffraction) of the Helmholtz-Zentrum at the storage ring BESSY in Berlin, Germany [133]. The $\sin^2\psi$ method was used to determine residual stress values. Principles of this method are discussed here briefly.

When a crystal is subjected to an elastic strain, the lattice spacing “d” depends on this applied strain. Based on this dependency, the named method “$\sin^2\Psi$” is used to calculate strain in polycrystalline materials; and thus, residual stress. In case of a biaxial rotationally symmetric stress state, the lattice spacing d_Ψ is a function of the angle Ψ between the surface normal and the diffraction vector according to the following relation:

$$\varepsilon(\Psi) = \frac{d_{\Psi} - d_0}{d_0} = \left(2S_1^{hkl} + \frac{1}{2}S_2^{hkl}\sin^2\Psi\right)\sigma \qquad (1)$$

where d_0 is the strain free lattice spacing and S_1^{hkl} and $\frac{1}{2}S_2^{hkl}$ are X-ray elastic constants (XECs) of the coating material [134]. By plotting the strain $\varepsilon(\Psi)$ (which is calculated from the measured lattice parameter d_Ψ) versus $\sin^2\psi$ (see Figure 3-6), residual stress can be determined from the corresponding slope of the straight line [134].

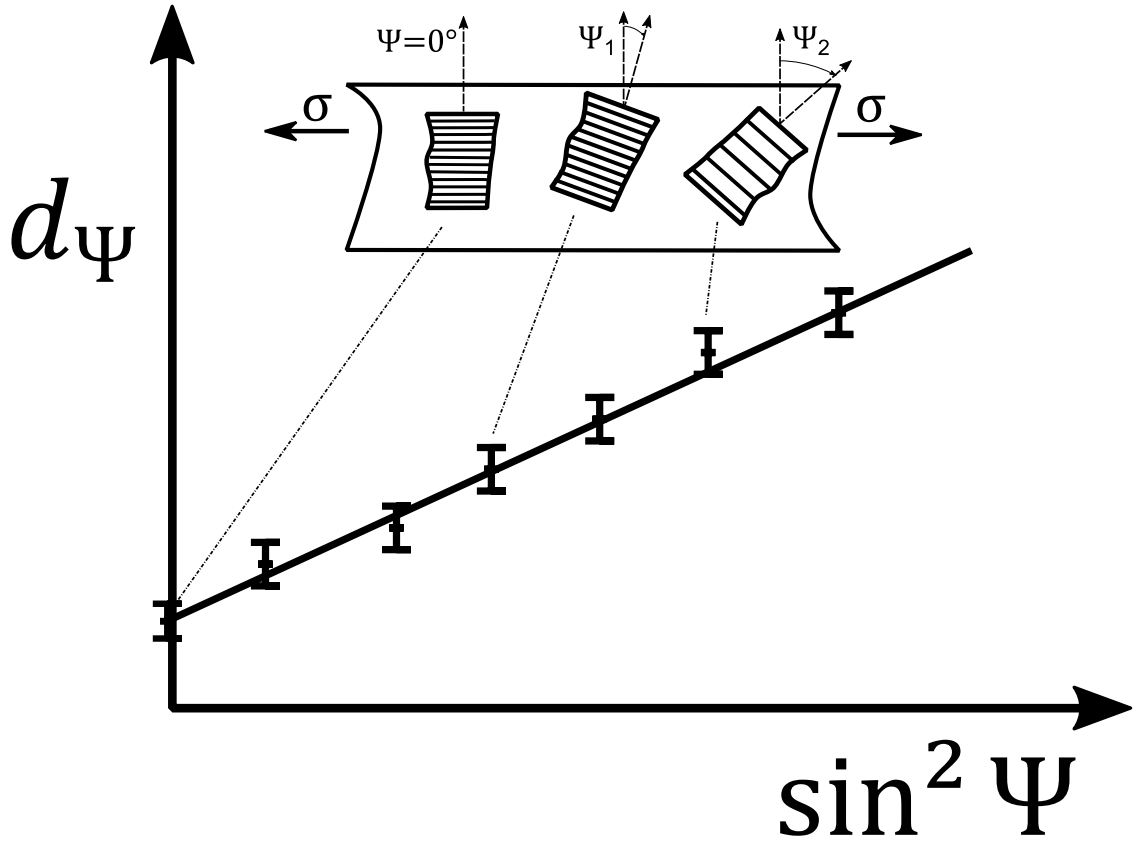

Figure 3-6: Schematic plot of the $\sin^2\psi$ principle. ψ is the angle between the sample normal and diffraction vector. The dependency of lattice spacing d with the angle Ψ is shown for rotationally symmetric tensile stress. The slope of the line gives the residual stress in the coating. (Adapted from [134,135]).

Thermal residual stresses of single-layered samples (Ti(C,N) and Zr(C,N)) were measured in paper IV [17]. Corresponding experimental parameters used at the beamline are summarized in Table 2.

Table 2: Experimental parameters of X-ray synchrotron measurements [135].

Primary Beam	0.5*0.5 mm^2
Secondary optics	Double slit system 0.03*8 mm^2 (equatorial*axial)
Diffraction angle	$2\theta = 9°$
Detector	Low energy solid state germanium detector (Canberra GL0110)
Counting time	100 s
Calibration	Gold powder (standard specimen in glass plate)

4. Summary of the results

4.1 Scope of the papers

As stated in the introduction of this thesis, the major target is to unveil properties and deformation mechanisms responsible for the extended tool life of Zr(C,N) based milling inserts, as compared to that exhibited by Ti(C,N) counterpart. Opposite to the latter, available literature on properties of zirconium-based nitrides, carbides and carbonitrides are very limited. Existing studies on these materials are focused on synthesis methods. Available data on the physical properties of this class of materials has to be handled with care as the synthesis processes are distinct among different research groups. It then yields large disparities in chemical composition, microstructure and density [136]. Pioneering work of Lengauer's research group addressed these shortcomings and provided reliable data of group IV carbonitride compounds [12,13]. Regarding the compounds under consideration here, physical and mechanical properties are quite comparable, considering that Zr and Ti are successive in the 4th group of the periodic table. Comparison shows that actually Ti($C_{0.5}$,$N_{0.5}$) is gradually harder and stiffer than Zr($C_{0.5}$,$N_{0.5}$) (Table 1). Overall better performance of the former in interrupted cutting would then be expected. However, it is not actually the case [11]. Hence, to understand the different wear behavior, the first approach was to investigate deformation mechanisms of these coatings at the microstructural scale. Micropillar compression was chosen and the results are presented in paper I [14]. Paper II [15] is directly related to the former, but here investigations are deepened to understand the distinctive low cohesive strength at the grain boundaries (GBs) of Ti(C,N), and correlate it to presumable segregation

highlighted by APT. As the Zr(C,N) presented better ductility over Ti(C,N) while keeping similar strength, the next step was to evaluate deformation mechanisms of this newly developed coating within the coated system, i.e. taking into consideration the substrate and corresponding interlayer at the interface. This was the objective of paper III [16]. Finally, in paper IV [17], the entire assemblage is tested at the macro-scale by means of spherical indentation. This approach was implemented to simulate and analyze failure at a coarser scale (comparable to application-related use) in order to depict the impact of the carbonitride layer on the entire assemblage, and compare these findings to the results obtained at the microstructural scale. Main strategy followed for this work is to study, analyze and compare Ti(C,N) and Zr(C,N) systems.

4.2 Paper I: Deformation mechanisms of the carbonitride layer

Title: *Investigations on micro-mechanical properties of polycrystalline Ti(C,N) and Zr(C,N) coatings.*

Deformation behavior and micro-mechanical properties at room temperature of Ti(C,N) and Zr(C,N) CVD coatings were evaluated. As mentioned in section 3.2.1, micropillar compression was selected - instead of nanoindentation - as a method of investigation, due to relatively more uniform stress-strain field. With respect to other micro-mechanical tests like micro-cantilever bending or micro-beam tension, tests under compression might imitate some deformation scenarios that are likely to occur in cutting applications. Analogous studies for hard coatings are scarce, and to the best knowledge of the authors, very few studies handle micro-compression testing of polycrystalline hard coatings [99–105], and none of them address transition-metal carbonitrides.

As these tests were performed on thin coating deposited on a non-conventional substrate for these experiments (WC-Co), the experimental setup was initially studied with the aid of finite element modeling (FEM). From stress-displacement curves, both Ti(C,N) and Zr(C,N) exhibited a relatively high yield strength (around 14 GPa), and Ti(C,N) was found to be stiffer than Zr(C,N). Meanwhile, the latter exhibited higher toughness. Post-mortem SEM showed that, different from Zr(C,N) where the crack path is undefined, Ti(C,N) undergoes a pure intergranular crack propagation and grain decohesion after yielding (Figure 4-1). EBSD mapping of post-compressed pillars revealed that Zr(C,N) exhibits misorientation gradients which are absent in Ti(C,N). This result suggests that in addition to its high strength and better cohesive strength, Zr(C,N) attested additionally plastic deformation at room temperature. The brittle behavior of Ti(C,N) is dominated by low cohesive strength along the GBs and reduced dislocation activation at room temperature. The results presented in this work may explain the enhanced performance of Zr(C,N) under cycled thermo-mechanical loads by the combination of high hardness, better cohesive strength and its supposed intrinsic plasticity in contrast to Ti(C,N).

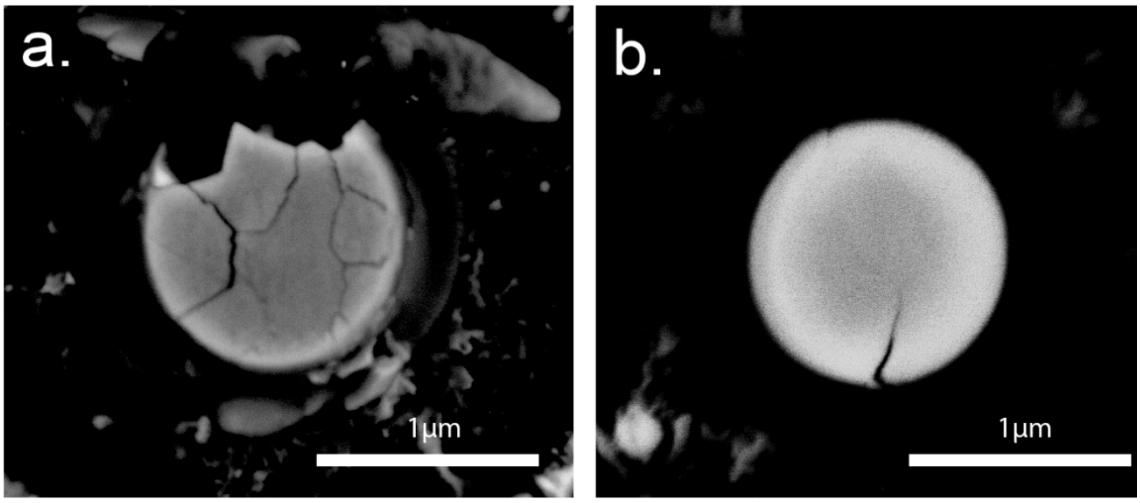

Figure 4-1: Top view post-compression images of (a) Ti(C,N) and (b) Zr(C,N) micropillars. While Zr(C,N) shows indefinite crack propagation, Ti(C,N) fails at the GBs revealing low cohesive strength leading to intercolumnar failure [14,15].

4.3 Paper II: Cohesive strength of GBs and crack propagation path

Title: *Atom Probe Tomography investigations on grain boundary segregation in polycrystalline Ti(C,N) and Zr(C,N) CVD coatings.*

The second paper is a direct sequel of the first one. Following the peculiar intergranular crack propagation discerned for Ti(C,N), it was speculated that a particular element (or phase) segregation at GBs could be responsible for its relatively lower cohesive strength. Thus, investigations went deeper with analysis of this hypothesis. Samples containing GBs of both Zr(C,N) and Ti(C,N) were explored with atom probe tomography (APT). Looking at the impurity candidates in the literature, it has been reported that chlorine contamination affects the mechanical properties of deposited CVD coating. Chlorine impurities stems from the use of prevalent metal chlorides as a precursor in CVD reactions. However, this issue

concerns almost exclusively low-temperature CVD processes, which are different from the present case in which the deposition temperature is in the range of 885-930 °C. Moreover, most authors have reported that chlorine is incorporated into the lattice [88,137–144], rather than to interfaces. Nevertheless, no direct evidence has been provided. Indeed, on the one hand, our results have shown that chlorine segregated at the GBs of Ti(C,N) along with Co in a interlocked way (see Figure 4-2). On the other hand, segregation of homogeneously distributed Co without Cl was evidenced for Zr(C,N). Co is diffusing from the WC-Co substrate to segregate at the interfaces of carbonitrides coating, while exclusive Cl segregation for Ti(C,N) was attributed to the combined effect of lower temperature deposition and higher partial pressure of the metal tetrachloride precursor, in comparison to Zr(C,N). From the calculated elements concentrations, it was suggested that Cl is segregated as a titanium subchloride complex ($TiCl_x$, $x<4$).

The next question concerns the impact of segregation on mechanical properties. It might be expected that segregation of cobalt will have a negative effect on the mechanical properties. This is particularly true at higher temperatures, when low melting phases form at the interface, leading to the drop of high-temperature strength [34]. Nevertheless, it was reported that diffusion and segregation of elements (at the GBs) from the WC-Co substrate during the deposition enhances the adhesion to the substrate and wear resistance [145,146]. Surprisingly, it was even reported that a Co-C(N) metal modified covalent bond at the interface is stronger than the bulk bonding between Ti-C(N) [147]. Regarding chlorine segregation, with its intrinsic high electronegativity, it would definitely have a dramatic negative effect on the interfacial cohesion and electronic structure between adjacent atoms at the GBs. For titanium based CVD coatings, it is agreed that mechanical properties degrade with

the increase of chlorine content, i.e. decrease in hardness [89,138–142,144,148,149] as well as reduction of adhesion to the substrate [89,141,142,148,149]. Hence, chlorine segregation might be one of the relevant factors contributing to the low cohesive strength at the GBs of Ti(C,N), which results in the specific intergranular fracture behavior evidenced under uniaxial compression of micropillars.

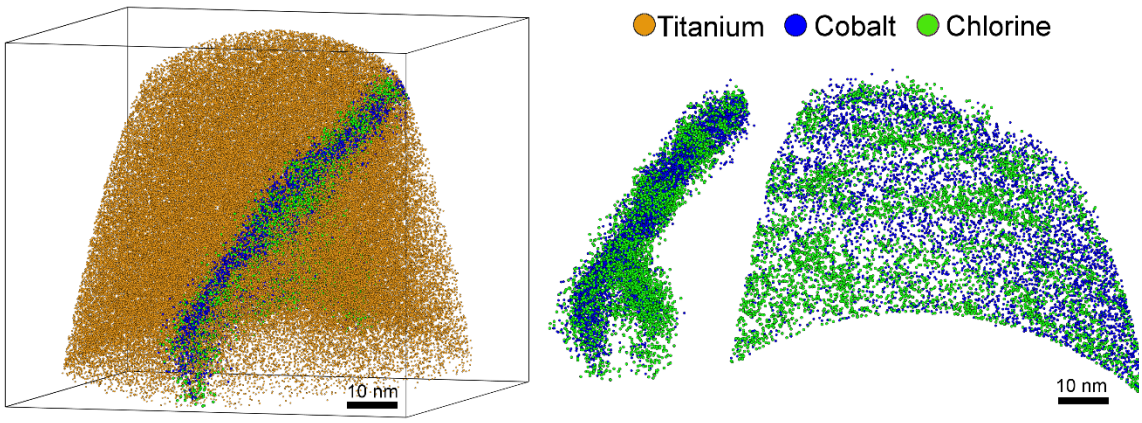

Figure 4-2: APT of a Ti(C,N) grain boundary highlighting chlorine and cobalt segregation in an interlocked way without mixing [15].

4.4 Paper III: Interfacial deformation of Zr(C,N) with the substrate

Title: *Micromechanical investigations of CVD coated WC-Co cemented carbide by micropillar compression.*

Once the microstructural factors behind better performance of Zr(C,N) have been unveiled, and knowing that in real application the coating is not performing independently but interact with different components of the cutting insert, the next stage was to investigate deformation behavior and interaction of different components of the cutting insert, i.e. WC-Co substrate, TiN bonding layer and Zr(C,N).

Hence, complex interactions between different components under compression in real applications were attempted to be replicated at the micro-scale by using the same technique as before, i.e. micropillar compression. Differently from the previous study, the pillars were milled from a cross-section such that comparable pillars from substrate, coating and their combination, including also the TiN interlayer, were available.

The present study is divided into two main sections. The first one focuses on deformation behavior of WC-Co substrate having a fine-grained WC phase and relatively low binder content (not addressed in previous literature reports). Besides, post-mortem deformation and microstructure were investigated using EBSD and high-resolution microscopy. In the second section, new composite pillars containing substrate, coating and the interlayer are evaluated and compared to the response of individual components.

Deformation of substrate pillars is influenced strongly by phase assemblage and distribution as distinct loading slopes were obtained for each substrate pillar. Nevertheless, similar to the previous study by Tarragó et al. [150], all the pillars presented an increasing unloading slope (in comparison to the loading) which is related to the change of effective phase assemblage after compression. Considerable slip takes place in the WC phase, as it has been showcased by the extensive and multiple slip in one sample (according to the established $\{10\bar{1}0\}\langle 11\bar{2}3\rangle$ slip system [151–154]) and initiation of several slip traces in different WC grains. Hence, in addition to the Co metallic phase, toughness of the cemented carbide may also be attributed to coarse WC phase which can absorb considerable strain energy by deforming plastically.

The second part deals with the hybrid structure. This new composite hybrid pillar presented the highest strength among the tested micropillars (see Figure 4-3). The coating contributed with its strength while the substrate provided the necessary toughness, which enhanced its properties and outscored their individual components in terms of ultimate strength. Moreover, both components (substrate and coating) had deformed together: WC grains in the substrate deformed plastically whereas the Zr(C,N) hard coating bent with the substrate component without developing a visible crack. This outstanding result could be attributed to better cohesive strength (at grain boundaries) and ductility of Zr(C,N), in comparison with the widely used Ti(C,N) coating (as highlighted in papers I [14] and II [15]). Finally, despite the higher shear stresses expected at the interfaces of TiN interlayer during compression tests, the latter provided an excellent interfacial strength between the substrate and the coating, which strengthens and bounds both components together.

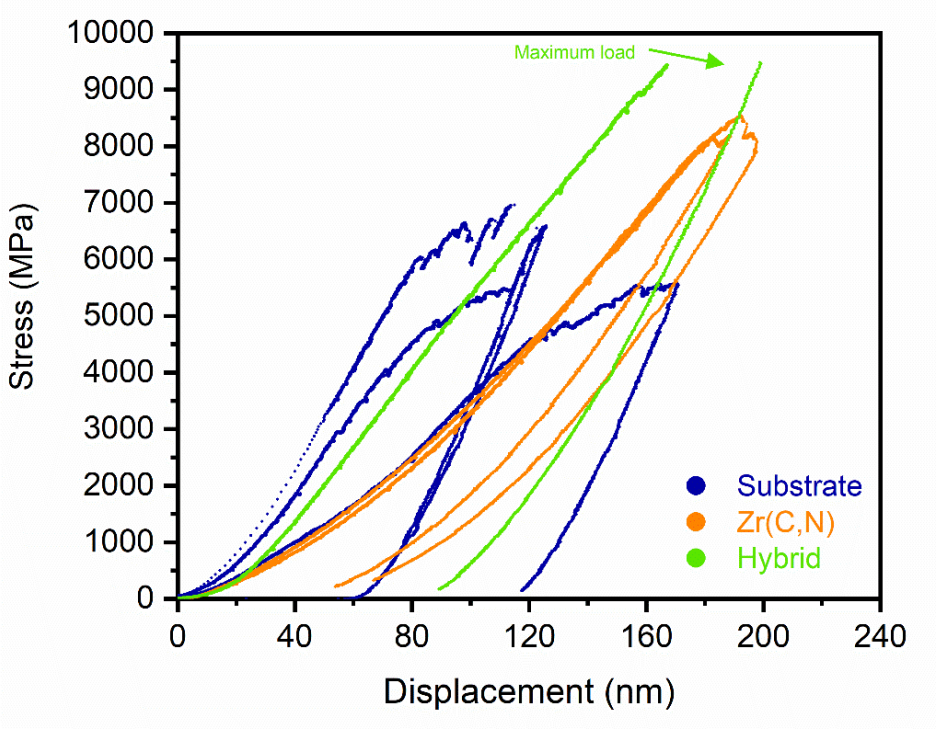

Figure 4-3: Stress and displacement curves of substrate pillars (S1, S2, S3) (Yield strength ~ 4-7 GPa), Zr(C,N) coating pillars (Yield strength ~ 8 GPa), and hybrid pillar (Ultimate strength ~ 9 GPa). Hybrid pillar exhibits the highest strength among all the tested specimens [16].

4.5 Paper IV: Mechanical resistance of the coated substrate system

Title: *Contact damage investigation of CVD carbonitride hard coatings deposited on cemented carbides.*

The aim of the fourth paper was the investigation of "macro"-mechanical properties of the entire industrial cutting insert systems - including the outer alumina layer - by means of spherical indentation tests. As indicated in section 3.2.2, this method consists of inducing controlled damage by spherical indentation with increasing monotonic load. For hard and brittle materials, the use of spherical

indentation is attractive in comparison to the conventional methods using sharp-like indenters. Main reason behind is that "blunt" indenters allow to monitor damage evolution with an uncracked microstructure, as a function of increasing applied load or number of cycles (for fatigue experiments) [113]. Use of this technique has proven to be helpful and adapted for investigating PVD coated systems [113–117].

The methodology of papers I [14] and II [15] is conserved, and effects of the wear-resistant carbonitride layer on the contact damage resistance of the cutting inserts are evaluated, based on comparison of coated systems whose exclusive difference was the use of either Ti(C,N) or Zr(C,N). The first approach was the evaluation of differences in damage mechanisms of the same samples investigated in papers I [14] and II [15] consisting of a single carbonitride Ti(C,N) or Zr(C,N) deposited on the substrate (single-layered samples). Then, the same testing protocol was extended to multilayered systems (with an outer alumina layer), corresponding to the real industrial cutting inserts (i.e. samples similar to the one in paper III). Confocal laser scanning microscopy (CLSM), SEM and FIB were used to characterize the residual imprints. Synchrotron X-ray was employed to measure the residual stresses of the carbonitride layer.

In this paper, circumferential cracks showed a continuous crack path for Zr(C,N). This was opposite to the behavior exhibited by Ti(C,N), where the crack path displayed a disrupted aspect. Polishing as-deposited samples (to remove inherited roughness of the columnar crystals) revealed that a spread peculiar crack network existed exclusively for Ti(C,N). This cracking network was rationalized by the dissimilar coefficient of thermal expansion (CTE) between the coating and the substrate, which is higher for Ti(C,N) than for Zr(C,N). Consequently, during cooling

down from deposition temperature (~900 °C), higher thermal stresses are generated resulting in an extensive cracking network only for Ti(C,N). Measured residual stresses allowed to speculate that a considerable stress relaxation takes place after cracking. This cracking network fragments the layer into small islands, impacting then the structural integrity. Within this context, it may be postulated that the disrupted circumferential crack path for Ti(C,N) specimen is a consequence of the interaction with the existing cooling cracks network. Moreover, at the microstructural scale, it is important to point out that the induced cracking path for the single-layered carbonitride coatings correlates well with previous micromechanical results in papers I [14] and II [15], linked to intergranular crack propagation for Ti(C,N) and mainly transgranular for Zr(C,N) (Figure 4-4), despite the different length scale of spherical indentation test from micro-compression one. For the multilayered specimens, associated finding were highlighted which were also related to the role of Zr(C,N) intermediate layer in conserving more the structural integrity of these specimens. In other words, CVD cooling cracks are less developed in samples where the intermediate layer is the Zr(C,N). Main reason is the lower CTE that reduces tensile stresses which are responsible for inducing CVD cooling cracks.

Then synergy of all these properties explains the higher resistance of Zr(C,N) samples, in terms of a larger dissipation of strain energy in irreversible deformation of the thin film. This is different for the Ti(C,N) samples, given the lessened structural integrity resulting from CVD cooling cracks and the low cohesive strength at grain boundaries.

Finally, mechanical performance of the CVD coated cemented carbides relies on the interplay between the multilayer coating sequence and the substrate, rather

than on the intrinsic properties of each single component in the coating/substrate system. This has to be taken into account in the design of innovative grades for machining applications.

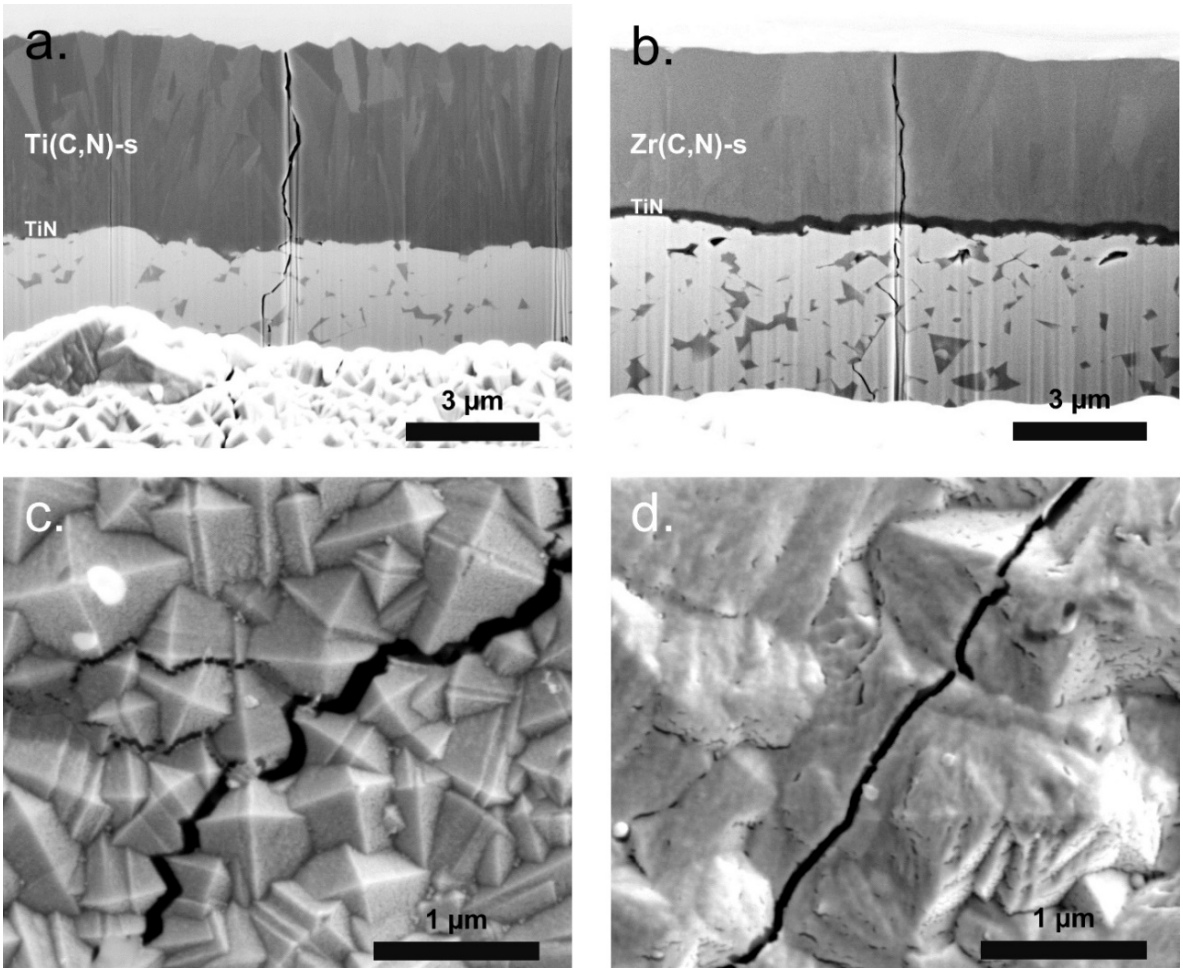

Figure 4-4: a./b. FIB cross sections at circumferential cracks induced by spherical indentation under an applied load of 2200 N for Ti(C,N)-s and Zr(C,N)-s samples, respectively. c./d. In plane SEM images of referred circumferential cracks for Ti(C,N)-s and Zr(C,N)-s specimens, respectively [17]. Similarly to previous results in papers I [14] and II [15], cracks propagate intergranularly for Ti(C,N) and mainly transgranularly for Zr(C,N).

5. Conclusion and perspectives

In this dissertation, the coating/substrate systems have been investigated through mechanical testing and microstructural characterization at different length scales using a wide set of advanced techniques. It was aimed to reveal the properties that sustain Zr(C,N) as a better coating for milling applications. Within this context, the following conclusions may be drawn:

- For single-layered samples, the more compatible coefficient of thermal expansion of Zr(C,N) with the substrate is responsible for the absence of the CVD cooling cracks network which preserved the structural integrity of the coating. In contrast, the higher CTE for Ti(C,N) generated considerable thermal stresses which exceeded the coating strength and caused extensive cracking. This makes the Ti(C,N) system similar to disconnected coating clusters deposited on the substrate for single and multilayered assemblage.

- Crystals of Zr(C,N) have attested a better cohesive strength at the grain boundaries, oppositely to Ti(C,N) in which cracks propagates almost exclusively along the grain boundaries. This behavior was revealed first with micro-compression tests and later supported through contact damage tests performed at a larger scale. This result points out a coating related intrinsic feature which is responsible for this cracking path tendency. The latter was attributed to exclusive chlorine segregation at grain boundaries of Ti(C,N), as demonstrated at the atomic scale by APT.

- Based on misorientation calculation, it was supposed that oppositely to Ti(C,N), Zr(C,N) is able to deform plastically to a certain extent before initiation and propagation of cracks.

In short, absence of extensive cracking network for Zr(C,N) - in the as deposited state - is one of the main advantages over Ti(C,N). This is mainly credited to adjusted coefficient of thermal expansion and to plastic deformation with better cohesive strength at the grain boundaries which will render more toughness to the coating. It must be noted that these properties are not only in favor of retaining structural integrity (in the as-deposited state), but also very decisive during milling applications as important thermo-mechanical cycling is taking place in the coating. These factors can explain better performance of Zr(C,N) in interrupted cutting under severe service conditions.

These investigations can be extended to explore more properties of these TMCN. Concerning micromechanical properties, it would be interesting to shed the light on the plastic deformation mechanisms of Zr(C,N). For this purpose, high resolution TEM has to be performed, and coarser single crystals with specific orientations have to be tested. Moreover, as these materials performs at superior temperatures, conducting micro-compression at high temperatures would be of great interest. Regarding phase segregation at the grain boundaries of these compounds, attempting to produce Ti(C,N) without chlorine segregation at a first stage and then inspecting the corresponding impact on the cohesive strength and micromechanical properties, is a subject of high concern. Similarly, effect of cobalt segregation at the grain boundaries seems to be a promising topic. With respect to the substrate-coating interface, examination of additional hybrid pillars with different substrate

assemblage will provide a deeper insight on the deformation and failure mechanisms at this critical spot. Furthermore, as the TiN interlayer has shown excellent interfacial strength, deeper investigation of deformation mechanisms of this nanocrystalline thin coating can be very relevant as well.

Finally, besides uncovering material related properties and features that gave advantage to Zr(C,N), these investigations provided better understanding and shed the light over microstructural features that can be tuned to enhance the properties and performance of CVD hard coating. Promising three routes or strategies for tailoring mechanical performance of CVD hard coating are proposed, as following:

- Reducing tensile thermal residual stresses leading to extensive cracking during deposition and interrupted machining with large temperature differences.

- Development of transition-metal compounds that can deform plastically and maintain indeed an adequate hardness.

- Engineering of grain boundary segregating phases (or complexities) that strengthen interfaces between the crystals.

6. References

[1] A. Osada, E. Nakamura, H. Homma, T. Hayahi, T. Oshika, Wear mechanism of thermally transformed CVD Al_2O_3 layer, International Journal of Refractory Metals and Hard Materials. 24 (2006) 387–391. https://doi.org/10.1016/j.ijrmhm.2005.11.007.

[2] J. García, V. Collado Ciprés, A. Blomqvist, B. Kaplan, Cemented carbide microstructures: a review, International Journal of Refractory Metals and Hard Materials. 80 (2019) 40–68. https://doi.org/10.1016/j.ijrmhm.2018.12.004.

[3] J. García, J. Persson, E. Göthelid, Development of Wear resistant coatings for cutting tools, in: World PM2016 Congress and Exhibition, Hamburg, Germany, 2016.

[4] L. von Fieandt, Cutting edge titanium-based CVD hard coatings, Acta Universitatis Upsaliensis, 2018.

[5] W. Lengauer, Transition metal carbides, nitrides, and carbonitrides, in: R. Riedel (Ed.), Handbook of Ceramic Hard Materials, Wiley-VCH Verlag GmbH, Weinheim, Germany, 2000: pp. 202–252. https://doi.org/10.1002/9783527618217.ch7.

[6] K.-D. Bouzakis, N. Michailidis, G. Skordaris, E. Bouzakis, D. Biermann, R. M'Saoubi, Cutting with coated tools: Coating technologies, characterization methods and performance optimization, CIRP Annals. 61 (2012) 703–723. https://doi.org/10.1016/j.cirp.2012.05.006.

[7] K. Bobzin, High-performance coatings for cutting tools, CIRP Journal of Manufacturing Science and Technology. 18 (2017) 1–9. https://doi.org/10.1016/j.cirpj.2016.11.004.

[8] K. Bewilogua, G. Bräuer, A. Dietz, J. Gäbler, G. Goch, B. Karpuschewski, B. Szyszka, Surface technology for automotive engineering, CIRP Annals. 58 (2009) 608–627. https://doi.org/10.1016/j.cirp.2009.09.001.

[9] P. Ettmayer, H. Kolaska, H.M. Ortner, History of Hardmetals, in: V.K. Sarin, D. Mari, L. Llanes (Eds.), Comprehensive Hard Materials - Volume 1: Hardmetals, Elsevier, 2014: pp. 3–27. https://doi.org/10.1016/B978-0-08-096527-7.00001-5.

[10] S. Söderberg, M. Sjöstrand, B. Ljungberg, Advances in coating technology for metal cutting tools, Metal Powder Report. 56 (2001) 24–30. https://doi.org/10.1016/S0026-0657(01)80174-0.

[11] J. García, M.F. Moreno, J. Östby, J. Persson, H.C. Pinto, Design of coated cemented carbides with improved comb crack resistance, in: Proceedings 19th Plansee Seminar, Reutte, Austria, 2017.

[12] W. Lengauer, S. Binder, K. Aigner, P. Ettmayer, A. Guillou, J. Debuigne, G. Groboth, Solid state properties of group IVb carbonitrides, Journal of Alloys and Compounds. 217 (1995) 137–147.

[13] Q. Yang, W. Lengauer, T. Koch, M. Scheerer, I. Smid, Hardness and elastic properties of Ti(C_xN_{1-x}), Zr(C_xN_{1-x}) and Hf(C_xN_{1-x}), Journal of Alloys and Compounds. 309 (2000) L5–L9. https://doi.org/10.1016/S0925-8388(00)01057-4.

[14] I. El Azhari, J. Garcia, M. Zamanzade, F. Soldera, C. Pauly, L. Llanes, F. Mücklich, Investigations on micro-mechanical properties of polycrystalline Ti(C,N) and Zr(C,N) coatings, Acta Materialia. 149 (2018) 364–376. https://doi.org/10.1016/j.actamat.2018.02.053.

[15] I. El Azhari, J. Barrirero, J. García, F. Soldera, L. Llanes, F. Mücklich, Atom Probe Tomography investigations on grain boundary segregation in polycrystalline Ti(C,N) and Zr(C,N) CVD coatings, Scripta Materialia. 162 (2019) 335–340. https://doi.org/10.1016/j.scriptamat.2018.11.041.

[16] I. El Azhari, J. García, M. Zamanzade, F. Soldera, C. Pauly, C. Motz, L. Llanes, F. Mücklich, Micromechanical investigations of CVD coated WC-Co cemented carbide by micropillar compression, Materials & Design. 186 (2020) 108283. https://doi.org/10.1016/j.matdes.2019.108283.

[17] I. El Azhari, J. García, F. Soldera, S. Suarez, E. Jiménez-Piqué, F. Mücklich, L. Llanes, Contact damage investigation of CVD carbonitride hard coatings deposited on cemented carbides, International Journal of Refractory Metals and Hard Materials. 86 (2020) 105050. https://doi.org/10.1016/j.ijrmhm.2019.105050.

[18] E.O. Travis, R.W. Fiordalice, Manufacturing aspects of low pressure chemical-vapor-deposited TiN barrier layers, Thin Solid Films. 236 (1993) 325–329. https://doi.org/10.1016/0040-6090(93)90690-Q.

[19] Y.T. Hou, F.Y. Yen, P.F. Hsu, V.S. Chang, P.S. Lim, C.L. Hung, L.G. Yao, J.C. Jiang, H.J. Lin, Y. Jin, S.M. Jang, H.J. Tao, S.C. Chen, M.S. Liang, High performance tantalum carbide metal gate stacks for nMOSFET application, in: IEEE InternationalElectron Devices Meeting, 2005. IEDM Technical Digest., IEEE, Tempe, Arizon, USA, 2005: pp. 31–34. https://doi.org/10.1109/IEDM.2005.1609258.

[20] G.W. Egeland, K. Wheeler, P. Peralta, K.J. McClellan, S.A. Maloy, G.M. Bond, Plastic deformation in zirconium nitride observed by nanoindentation and TEM, Journal of Nuclear Materials. 416 (2011) 253–261. https://doi.org/10.1016/j.jnucmat.2010.12.002.

[21] Y. Katoh, G. Vasudevamurthy, T. Nozawa, L.L. Snead, Properties of zirconium carbide for nuclear fuel applications, Journal of Nuclear Materials. 441 (2013) 718–742. https://doi.org/10.1016/j.jnucmat.2013.05.037.

[22] W.E. Lee, E. Giorgi, R. Harrison, A. Maître, O. Rapaud, Nuclear applications for ultra-high temperature ceramics and MAX phases, in: W.G. Fahrenholtz, E.J. Wuchina, W.E. Lee, Y. Zhou (Eds.), Ultra-High Temperature Ceramics, John Wiley & Sons, Inc, Hoboken, NJ, 2014: pp. 391–415. https://doi.org/10.1002/9781118700853.ch15.

[23] L. Courtright, H.C. Graham, A.P. Katz, R.J. Kerans, Ultrahigh temperature assessment study: ceramic matrix composites, Wright Laboratory Materials

Directorate, Wright Patterson Air Force Base, Ohio, 1992. https://apps.dtic.mil/docs/citations/ADA262740.

[24] W.G. Fahrenholtz, G.E. Hilmas, Ultra-high temperature ceramics: Materials for extreme environments, Scripta Materialia. 129 (2017) 94–99. https://doi.org/10.1016/j.scriptamat.2016.10.018.

[25] H. Moissan, F. Lengfeld, Sur un nouveau carbure de zirconium, Comptes rendus hebdomadaires des séances de l'Académie des sciences. 122 (1896) 651–654.

[26] W.S. Williams, Influence of temperature, strain rate, surface condition, and composition on the plasticity of transition-metal carbide crystals, Journal of Applied Physics. 35 (1964) 1329–1338. https://doi.org/10.1063/1.1713614.

[27] G.E. Hollox, R.E. Smallman, Plastic behavior of titanium carbide, Journal of Applied Physics. 37 (1966) 818–823. https://doi.org/10.1063/1.1708264.

[28] D.W. Lee, J.S. Haggerty, Plasticity and creep in single crystals of zirconium carbide, Journal of the American Ceramic Society. 52 (1969) 641–647.

[29] I.V. Gridneva, Y.V. Mil'man, G.A. Rymashevskii, V.I. Trefilov, S.I. Chugunova, Effect of temperature on the strength characteristics of zirconium carbide, Soviet Powder Metallurgy and Metal Ceramics. 15 (1976) 638–645. https://doi.org/10.1007/BF01159455.

[30] R. Darolia, T.F. Archbold, Plastic deformation of polycrystalline zirconium carbide, Journal of Materials Science. 11 (1976) 283–290.

[31] D.K. Chatterjee, M.G. Mendiratta, H.A. Lipsitt, Deformation behaviour of single crystals of titanium carbide, Journal of Materials Science. 14 (1979) 2151–2156.

[32] E. Breval, Microplasticity at room temperature of single-crystal titanium carbide with different stoichiometry, Journal of Materials Science. 16 (1981) 2781–2788.

[33] G. Das, K.S. Mazdiyasni, H.A. Lipsitt, Mechanical properties of polycrystalline TiC, Journal of the American Ceramic Society. 65 (1982) 104–110.

[34] A.P. Katz, H.A. Lipsitt, T. Mah, M.G. Mendiratta, Mechanical behaviour of polycrystalline TiC, Journal of Materials Science. 18 (1983) 1983–1992.

[35] V.M. Sura, D.L. Kohlstedt, State-variable analysis of inelastic deformation of TiC single crystals, Journal of the American Ceramic Society. 70 (1987) 315–320.

[36] S.-H. Jhi, J. Ihm, S.G. Louie, M.L. Cohen, Electronic mechanism of hardness enhancement in transition-metal carbonitrides, Nature. 399 (1999) 132–134. https://doi.org/10.1038/20148.

[37] A. Zaoui, B. Bouhafs, P. Ruterana, First-principles calculations on the electronic structure of TiC_xN_{1-x}, $Zr_xNb_{1-x}C$ and HfC_xN_{1-x} alloys, Materials Chemistry and Physics. 91 (2005) 108–115. https://doi.org/10.1016/j.matchemphys.2004.10.056.

[38] V.I. Ivashchenko, P.E.A. Turchi, L.A. Ivashchenko, P.L. Skrynskii, Electronic origin of elastic properties of titanium carbonitride alloys, Metallurgical and Materials Transactions A. 37 (2006) 3391–3396. https://doi.org/10.1007/s11661-006-1031-9.

[39] V.I. Ivashchenko, P.E.A. Turchi, V.I. Shevchenko, First-principles study of elastic and stability properties of ZrC–ZrN and ZrC–TiC alloys, Journal of Physics: Condensed Matter. 21 (2009) 395503. https://doi.org/10.1088/0953-8984/21/39/395503.

[40] W. Feng, S. Cui, H. Hu, G. Zhang, Z. Lv, Electronic structure and elastic constants of TiC_xN_{1-x}, $Zr_xNb_{1-x}C$ and HfC_xN_{1-x} alloys: A first-principles study, Physica B: Condensed Matter. 406 (2011) 3631–3635. https://doi.org/10.1016/j.physb.2011.06.058.

[41] R.F. Zhang, S.H. Sheng, S. Veprek, Origin of different plastic resistance of transition metal nitrides and carbides: Stiffer yet softer, Scripta Materialia. 68 (2013) 913–916. https://doi.org/10.1016/j.scriptamat.2013.01.040.

[42] S.K. Yadav, R. Ramprasad, A. Misra, X.-Y. Liu, Core structure and Peierls stress of edge and screw dislocations in TiN: A density functional theory study, Acta Materialia. 74 (2014) 268–277. https://doi.org/10.1016/j.actamat.2014.04.047.

[43] V. Krasnenko, M.G. Brik, First-principles calculations of the structural, elastic and electronic properties of MN_xC_{1-x} ($M = Ti, Zr, Hf$; $0 \leq x \leq 1$) carbonitrides at ambient and elevated hydrostatic pressure, Solid State Sciences. 28 (2014) 1–8. https://doi.org/10.1016/j.solidstatesciences.2013.11.012.

[44] S. Kiani, C. Ratsch, A.M. Minor, S. Kodambaka, J.-M. Yang, Orientation- and size-dependent room-temperature plasticity in ZrC crystals, Philosophical Magazine. 95 (2015) 985–997. https://doi.org/10.1080/14786435.2015.1012568.

[45] T. Li, T. Liu, L. Zhang, T. Fu, H. Wei, First-principles investigation on slip systems and twinnability of TiC, Computational Materials Science. 126 (2017) 103–107. https://doi.org/10.1016/j.commatsci.2016.09.028.

[46] J. Kim, Y.J. Suh, Temperature- and pressure-dependent elastic properties, thermal expansion ratios, and minimum thermal conductivities of ZrC, ZrN, and $Zr(C_{0.5}N_{0.5})$, Ceramics International. 43 (2017) 12968–12974. https://doi.org/10.1016/j.ceramint.2017.06.195.

[47] L. Toth, Mechanical properties, in: Transition Metal Carbides and Nitrides, 1st ed., Academic Press, 1971: pp. 141–184.

[48] G.E. Hollox, Microstructure and mechanical behavior of carbides, Materials Science and Engineering. 3 (1968) 121–137. https://doi.org/10.1016/0025-5416(68)90001-3.

[49] S. Kiani, C. Ratsch, A.M. Minor, J.-M. Yang, S. Kodambaka, In situ transmission electron microscopy observations of room-temperature plasticity in sub-micron-size TaC(100) and TaC(011) single crystals, Scripta Materialia. 100 (2015) 13–16. https://doi.org/10.1016/j.scriptamat.2014.11.036.

[50] D.G. Sangiovanni, L. Hultman, V. Chirita, Supertoughening in B1 transition metal nitride alloys by increased valence electron concentration, Acta Materialia. 59 (2011) 2121–2134. https://doi.org/10.1016/j.actamat.2010.12.013.

[51] H. Kindlund, D.G. Sangiovanni, L. Martínez-de-Olcoz, J. Lu, J. Jensen, J. Birch, I. Petrov, J.E. Greene, V. Chirita, L. Hultman, Toughness enhancement in hard

ceramic thin films by alloy design, APL Materials. 1 (2013) 042104. https://doi.org/10.1063/1.4822440.

[52] D.G. Sangiovanni, L. Hultman, V. Chirita, I. Petrov, J.E. Greene, Effects of phase stability, lattice ordering, and electron density on plastic deformation in cubic TiWN pseudobinary transition-metal nitride alloys, Acta Materialia. 103 (2016) 823–835. https://doi.org/10.1016/j.actamat.2015.10.039.

[53] S.V. Ushakov, A. Navrotsky, Q.-J. Hong, A. van de Walle, Carbides and Nitrides of Zirconium and Hafnium, Materials. 12 (2019) 2728. https://doi.org/10.3390/ma12172728.

[54] W.G. Fahrenholtz, G.E. Hilmas, I.G. Talmy, J.A. Zaykoski, Refractory diborides of zirconium and hafnium, Journal of the American Ceramic Society. 90 (2007) 1347–1364. https://doi.org/10.1111/j.1551-2916.2007.01583.x.

[55] J. Garcia, R. Pitonak, R. Weissenbacher, A. Köpf, Production and characterization of wear resistant Ti(C,N) coatings manufactured by modified chemical vapor deposition process, Surface and Coatings Technology. 205 (2010) 2322–2327. https://doi.org/10.1016/j.surfcoat.2010.09.013.

[56] S.J. Bull, D.G. Bhat, M.H. Staia, Properties and performance of commercial TiCN coatings. Part 2: tribological performance, Surface and Coatings Technology. 163–164 (2003) 507–514. https://doi.org/10.1016/S0257-8972(02)00651-5.

[57] E. Bergmann, H. Kaufmann, R. Schmid, J. Vogel, Ion-plated titanium carbonitride films, Surface and Coatings Technology. 42 (1990) 237–251. https://doi.org/10.1016/0257-8972(90)90156-7.

[58] R.W. Harrison, W.E. Lee, Processing and properties of ZrC, ZrN and ZrCN ceramics: a review, Advances in Applied Ceramics. 115 (2016) 294–307. https://doi.org/10.1179/1743676115Y.0000000061.

[59] L. van Leaven, M.N. Alias, R. Brown, Corrosion behavior of ion plated and implated films, Surface and Coatings Technology. 53 (1992) 25–34. https://doi.org/10.1016/0257-8972(92)90100-O.

[60] F. Hollstein, D. Kitta, P. Louda, F. Pacal, J. Meinhardt, Investigation of low-reflective ZrCN–PVD-arc coatings for application on medical tools for minimally invasive surgery, Surface and Coatings Technology. 142–144 (2001) 1063–1068. https://doi.org/10.1016/S0257-8972(01)01222-1.

[61] A.S. Korhonen, J.M. Molarius, I. Penttinen, E. Harju, Hard transition metal nitride films deposited by triode ion plating, Materials Science and Engineering: A. 105–106 (1988) 497–501. https://doi.org/10.1016/0025-5416(88)90734-3.

[62] W.C. Russell, Experimental Design Approach to Development of a CVD ZrN Coating, Le Journal de Physique IV. 05 (1995) 127–134. https://doi.org/10.1051/jphyscol:1995513.

[63] S. Kudapa, K. Narasimhan, P. Boppana, W.C. Russell, Characterization and properties of MTCVD TiCN and MTCVD ZrCN coatings, Surface and Coatings Technology. 120 (1999) 259–264. https://doi.org/10.1016/S0257-8972(99)00484-3.

[64] C.P. Allenbach, MOCVD and tribological properties of thin zirconium carbonitride films, ETH Zurich, 2000. https://doi.org/10.3929/ethz-a-004064305.

[65] C.-A. Manier, H. Ziegele, J. Barriga, J. Goikoetxea, M. Woydt, Zirconium-based coatings in highly stressed rolling contacts as alternative solution to DLC and ta-C coatings, Wear. 269 (2010) 770–781. https://doi.org/10.1016/j.wear.2010.08.004.

[66] M. Braic, V. Braic, M. Balaceanu, C.N. Zoita, A. Kiss, A. Vladescu, A. Popescu, R. Ripeanu, Structure and properties of Zr/ZrCN coatings deposited by cathodic arc method, Materials Chemistry and Physics. 126 (2011) 818–825. https://doi.org/10.1016/j.matchemphys.2010.12.036.

[67] E. Silva, M. Rebelo de Figueiredo, R. Franz, R. Escobar Galindo, C. Palacio, A. Espinosa, S. Calderon V., C. Mitterer, S. Carvalho, Structure–property relations in ZrCN coatings for tribological applications, Surface and Coatings Technology. 205 (2010) 2134–2141. https://doi.org/10.1016/j.surfcoat.2010.08.126.

[68] C. Agte, K. Moers, Methoden zur Reindarstellung hochschmelzender Carbide, Nitride und Boride und Beschreibung einiger ihrer Eigenschaften, Zeitschrift für anorganische und allgemeine Chemie. 198 (1931) 233–275. https://doi.org/10.1002/zaac.19311980122.

[69] P. Villars, P. Villars, Pearson's handbook: crystallographic data for intermetallic phases, Desk ed, ASM International, Materials Park, OH, 1997.

[70] P. Villars, K. Cenzual, $TiC_{1-x}N_x$, x= 0.5 ($TiC_{0.5}N_{0.5}$) Crystal Structure: Datasheet from "PAULING FILE Multinaries Edition – 2012" in SpringerMaterials (https://materials.springer.com/isp/crystallographic/docs/sd_1831497), Springer-Verlag Berlin Heidelberg & Material Phases Data System (MPDS), Switzerland & National Institute for Materials Science (NIMS), Japan, n.d. https://materials.springer.com/isp/crystallographic/docs/sd_1831497.

[71] K. Aigner, W. Lengauer, D. Rafaja, P. Ettmayer, Lattice parameters and thermal expansion of $Ti(C_xN_{1-x})$, $Zr(C_xN_{1-x})$, $Hf(C_xN_{1-x})$ and TiN_{1-x} from 298 to 1473 K as investigated by high-temperature X-ray diffraction, Journal of Alloys and Compounds. 215 (1994) 121–126. https://doi.org/10.1016/0925-8388(94)90828-1.

[72] P. Villars, K. Cenzual, $ZrN_{0.5}C_{0.5}$ ($ZrC_{0.5}N_{0.5}$) Crystal Structure: Datasheet from "PAULING FILE Multinaries Edition – 2012" in SpringerMaterials (https://materials.springer.com/isp/crystallographic/docs/sd_0303358), Springer-Verlag Berlin Heidelberg & Material Phases Data System (MPDS), Switzerland & National Institute for Materials Science (NIMS), Japan, n.d. https://materials.springer.com/isp/crystallographic/docs/sd_0303358.

[73] W. Schintlmeister, W. Wallgram, J. Kanz, K. Gigl, Cutting tool materials coated by chemical vapour deposition, Wear. 100 (1984) 153–169.

[74] R. Haubner, M. Lessiak, R. Pitonak, A. Köpf, R. Weissenbacher, Evolution of conventional hard coatings for its use on cutting tools, International Journal of Refractory Metals and Hard Materials. 62 (2017) 210–218. https://doi.org/10.1016/j.ijrmhm.2016.05.009.

[75] C. Mitterer, PVD and CVD hard coatings, in: V.K. Sarin, L. Llanes, D. Mari (Eds.), Comprehensive Hard Materials - Volume 2: Ceramics, Elsevier, Amsterdam, 2014: pp. 449–468. https://doi.org/10.1016/B978-0-08-096527-7.00035-0.

[76] H.O. Pierson, The CVD of ceramic materials: carbides, in: Handbook of Chemical Vapor Deposition (CVD), 2nd ed., Park Ridge: Noyes Publications, USA, 1999: pp. 231–259.

[77] R. Haubner, The history of hard CVD coatings for tool applications at the University of Technology Vienna, International Journal of Refractory Metals and Hard Materials. 41 (2013) 22–34. https://doi.org/10.1016/j.ijrmhm.2013.01.012.

[78] K.E. Spear, Principles and applications of chemical vapor deposition (CVD), Pure and Applied Chemistry. 54 (1982) 1297–1311. https://doi.org/10.1351/pac198254071297.

[79] K. Choy, Chemical vapour deposition of coatings, Progress in Materials Science. 48 (2003) 57–170. https://doi.org/10.1016/S0079-6425(01)00009-3.

[80] A. Larsson, S. Ruppi, Microstructure and properties of Ti(C,N) coatings produced by moderate temperature chemical vapour deposition, Thin Solid Films. 402 (2002) 203–210. https://doi.org/10.1016/S0040-6090(01)01712-6.

[81] H.G. Prengel, W.R. Pfouts, A.T. Santhanam, State of the art in hard coatings for carbide cutting tools, Surface and Coatings Technology. 102 (1998) 183–190. https://doi.org/10.1016/S0257-8972(96)03061-7.

[82] S. Ruppi, Advances in chemically vapour deposited wear resistant coatings, Le Journal de Physique IV. 11 (2001) 847–859. https://doi.org/10.1051/jp4:20013106.

[83] S.R. Kurtz, R.G. Gordon, Chemical vapor deposition of titanium nitride at low temperatures, Thin Solid Films. 140 (1986) 277–290. https://doi.org/10.1016/0040-6090(86)90271-3.

[84] M.J. Buiting, A.H. Reader, Influence of impurities and microstructure on the resistivity of LPCVD titanium nitride films, MRS Online Proceedings Library Archive. 168 (1989). https://doi.org/10.1557/PROC-168-199.

[85] M.J. Buiting, A.F. Otterloo, A.H. Montree, Kinetical Aspects of the LPCVD of Titanium Nitride from Titanium Tetrachloride and Ammonia, Journal of the Electrochemical Society. 138 (1991) 500–505. https://doi.org/10.1149/1.2085618.

[86] N. Yokoyama, LPCVD Titanium Nitride for ULSIs, Journal of The Electrochemical Society. 138 (1991) 190–195. https://doi.org/10.1149/1.2085535.

[87] R.I. Hegde, R.W. Fiordalice, P.J. Tobin, TiNCl formation during low-temperature, low-pressure chemical vapor deposition of TiN, Applied Physics Letters. 62 (1993) 2326–2328. https://doi.org/10.1063/1.109406.

[88] R. Leutenecker, B. Fröschle, U. Cao-Minh, P. Ramm, Titanium nitride films for barrier applications produced by rapid thermal CVD and subsequent in-situ annealing, Thin Solid Films. 270 (1995) 621–626. https://doi.org/10.1016/0040-6090(95)06898-8.

[89] S. Anderbouhr, V. Ghetta, E. Blanquet, C. Chabrol, F. Schuster, C. Bernard, R. Madar, LPCVD and PACVD (Ti,Al)N films: morphology and mechanical properties, Surface and Coatings Technology. 115 (1999) 103–110. https://doi.org/10.1016/S0257-8972(99)00062-6.

[90] N. Ramanuja, R.A. Levy, S.N. Dharmadhikari, E. Ramos, C.W. Pearce, S.C. Menasian, P.C. Schamberger, C.C. Collins, Synthesis and characterization of low pressure chemically vapor deposited titanium nitride films using $TiCl_4$ and NH_3, Materials Letters. 57 (2002) 261–269. https://doi.org/10.1016/S0167-577X(02)00776-0.

[91] J. Wagner, V. Edlmayr, M. Penoy, C. Michotte, C. Mitterer, M. Kathrein, Deposition of Ti–Al–N coatings by thermal CVD, International Journal of Refractory Metals and Hard Materials. 26 (2008) 563–568. https://doi.org/10.1016/j.ijrmhm.2008.01.003.

[92] L.A. Dobrzański, D. Pakula, M. Staszuk, Chemical vapor deposition in manufacturing, in: A.Y.C. Nee (Ed.), Handbook of Manufacturing Engineering and Technology, Springer London, London, 2015: pp. 2755–2803. https://doi.org/10.1007/978-1-4471-4670-4_30.

[93] S.J. Cho, S.-H. Nam, C.-K. Jung, H.-G. Jee, J.-H. Boo, S. Kim, J.G. Han, Study on plasma assisted metal-organic chemical vapor deposition of Zr(C,N) and Ti(C,N) thin films and *in situ* plasma diagnostics with optical emission spectroscopy, Journal of Vacuum Science & Technology A: Vacuum, Surfaces, and Films. 26 (2008) 847–853. https://doi.org/10.1116/1.2944262.

[94] M.D. Uchic, Sample Dimensions Influence Strength and Crystal Plasticity, Science. 305 (2004) 986–989. https://doi.org/10.1126/science.1098993.

[95] J.R. Greer, J.Th.M. De Hosson, Plasticity in small-sized metallic systems: Intrinsic versus extrinsic size effect, Progress in Materials Science. 56 (2011) 654–724. https://doi.org/10.1016/j.pmatsci.2011.01.005.

[96] O. Torrents Abad, J.M. Wheeler, J. Michler, A.S. Schneider, E. Arzt, Temperature-dependent size effects on the strength of Ta and W micropillars, Acta Materialia. 103 (2016) 483–494. https://doi.org/10.1016/j.actamat.2015.10.016.

[97] N. Kheradmand, H. Vehoff, A. Barnoush, An insight into the role of the grain boundary in plastic deformation by means of a bicrystalline pillar compression test and atomistic simulation, Acta Materialia. 61 (2013) 7454–7465. https://doi.org/10.1016/j.actamat.2013.08.056.

[98] P.J. Imrich, C. Kirchlechner, C. Motz, G. Dehm, Differences in deformation behavior of bicrystalline Cu micropillars containing a twin boundary or a large-angle grain boundary, Acta Materialia. 73 (2014) 240–250. https://doi.org/10.1016/j.actamat.2014.04.022.

[99] G. Dehm, H.P. Wörgötter, S. Cazottes, J.M. Purswani, D. Gall, C. Mitterer, D. Kiener, Can micro-compression testing provide stress–strain data for thin films?, Thin Solid Films. 518 (2009) 1517–1521. https://doi.org/10.1016/j.tsf.2009.09.070.

[100] M. Schlögl, C. Kirchlechner, J. Paulitsch, J. Keckes, P.H. Mayrhofer, Effects of structure and interfaces on fracture toughness of CrN/AlN multilayer coatings,

Scripta Materialia. 68 (2013) 917–920. https://doi.org/10.1016/j.scriptamat.2013.01.039.

[101] J.M. Wheeler, R. Raghavan, V. Chawla, M. Morstein, J. Michler, Deformation of hard coatings at elevated temperatures, Surface and Coatings Technology. 254 (2014) 382–387. https://doi.org/10.1016/j.surfcoat.2014.06.048.

[102] S. Liu, R. Raghavan, X.T. Zeng, J. Michler, W.J. Clegg, Compressive deformation and failure of CrAlN/Si_3N_4 nanocomposite coatings, Applied Physics Letters. 104 (2014) 081919.

[103] Y. Zou, H. Ma, R. Spolenak, Ultrastrong ductile and stable high-entropy alloys at small scales, Nature Communications. 6 (2015) 7748. https://doi.org/10.1038/ncomms8748.

[104] S. Liu, J.M. Wheeler, J. Michler, X.T. Zeng, W.J. Clegg, Plastic flow at the theoretical yield stress in ceramic films, Scripta Materialia. 117 (2016) 24–27. https://doi.org/10.1016/j.scriptamat.2016.02.008.

[105] Y. Mu, X. Zhang, J.W. Hutchinson, W.J. Meng, Measuring critical stress for shear failure of interfacial regions in coating/interlayer/substrate systems through a micro-pillar testing protocol, Journal of Materials Research. 32 (2017) 1421–1431. https://doi.org/10.1557/jmr.2016.516.

[106] S. Korte-Kerzel, Microcompression of brittle and anisotropic crystals: recent advances and current challenges in studying plasticity in hard materials, MRS Communications. 7 (2017) 109–120. https://doi.org/10.1557/mrc.2017.15.

[107] D. Kiener, C. Motz, G. Dehm, Micro-compression testing: A critical discussion of experimental constraints, Materials Science and Engineering: A. 505 (2009) 79–87. https://doi.org/10.1016/j.msea.2009.01.005.

[108] H. Fei, A. Abraham, N. Chawla, H. Jiang, Evaluation of micro-pillar compression tests for accurate determination of elastic-plastic constitutive relations, Journal of Applied Mechanics. 79 (2012) 061011.

[109] G. Dehm, B.N. Jaya, R. Raghavan, C. Kirchlechner, Overview on micro- and nanomechanical testing: New insights in interface plasticity and fracture at small length scales, Acta Materialia. 142 (2018) 248–282. https://doi.org/10.1016/j.actamat.2017.06.019.

[110] B.R. Lawn, Indentation of Ceramics with Spheres: A Century after Hertz, Journal of the American Ceramic Society. 81 (1998) 1977–1994. https://doi.org/10.1111/j.1151-2916.1998.tb02580.x.

[111] A. Góez, D. Coureaux, A. Ingebrand, B. Reig, E. Tarrés, A. Mestra, A. Mateo, E. Jiménez-Piqué, L. Llanes, Contact damage and residual strength in hardmetals, International Journal of Refractory Metals and Hard Materials. 30 (2012) 121–127. https://doi.org/10.1016/j.ijrmhm.2011.07.013.

[112] F. García-Marro, A. Mestra, V. Kanyanta, K. Maweja, S. Ozbayraktar, L. Llanes, Contact damage and residual strength in polycrystalline diamond (PCD), Diamond and Related Materials. 65 (2016) 131–136. https://doi.org/10.1016/j.diamond.2016.03.004.

[113] E. Tarrés, G. Ramírez, Y. Gaillard, E. Jiménez-Piqué, L. Llanes, Contact fatigue behavior of PVD-coated hardmetals, International Journal of Refractory Metals

and Hard Materials. 27 (2009) 323–331. https://doi.org/10.1016/j.ijrmhm.2008.05.003.

[114] G. Ramírez, A. Mestra, B. Casas, I. Valls, R. Martínez, R. Bueno, A. Góez, A. Mateo, L. Llanes, Influence of substrate microstructure on the contact fatigue strength of coated cold-work tool steels, Surface and Coatings Technology. 206 (2012) 3069–3081. https://doi.org/10.1016/j.surfcoat.2011.12.012.

[115] J.J. Roa, E. Jiménez-Piqué, R. Martínez, G. Ramírez, J.M. Tarragó, R. Rodríguez, L. Llanes, Contact damage and fracture micromechanisms of multilayered TiN/CrN coatings at micro- and nano-length scales, Thin Solid Films. 571 (2014) 308–315. https://doi.org/10.1016/j.tsf.2014.04.018.

[116] J. Yang, F. García Marro, T. Trifonov, M. Odén, M.P. Johansson-Jõesaar, L. Llanes, Contact damage resistance of TiN-coated hardmetals: Beneficial effects associated with substrate grinding, Surface and Coatings Technology. 275 (2015) 133–141. https://doi.org/10.1016/j.surfcoat.2015.05.028.

[117] G. Ramírez, E. Jiménez-Piqué, A. Mestra, M. Vilaseca, D. Casellas, L. Llanes, A comparative study of the contact fatigue behavior and associated damage micromechanisms of TiN- and WC:H-coated cold-work tool steel, Tribology International. 88 (2015) 263–270. https://doi.org/10.1016/j.triboint.2015.03.036.

[118] R.L. Price, W.G. Jerome, Introduction and Historical Perspective, in: W.G. Jerome, R.L. Price (Eds.), Basic Confocal Microscopy, Springer International Publishing, Switzerland, 2018: pp. 1–20. https://doi.org/10.1007/978-3-319-97454-5_1.

[119] A. Ul-Hamid, Introduction, in: A Beginners' Guide to Scanning Electron Microscopy, Springer International Publishing, Switzerland, 2018: pp. 1–14. https://doi.org/10.1007/978-3-319-98482-7_1.

[120] A. Ul-Hamid, Specialized SEM Techniques, in: A Beginners' Guide to Scanning Electron Microscopy, Springer International Publishing, Switzerland, 2018: pp. 181–232. https://doi.org/10.1007/978-3-319-98482-7_5.

[121] A. Ul-Hamid, Contrast Formation in the SEM, in: A Beginners' Guide to Scanning Electron Microscopy, Springer International Publishing, Switzerland, 2018: pp. 77–128. https://doi.org/10.1007/978-3-319-98482-7_3.

[122] C.A. Volkert, A.M. Minor, Focused Ion Beam Microscopy and Micromachining, MRS Bulletin. 32 (2007) 389–399. https://doi.org/10.1557/mrs2007.62.

[123] D. Kiener, C. Motz, M. Rester, M. Jenko, G. Dehm, FIB damage of Cu and possible consequences for miniaturized mechanical tests, Materials Science and Engineering: A. 459 (2007) 262–272. https://doi.org/10.1016/j.msea.2007.01.046.

[124] S. Zaefferer, G. Habler, Scanning electron microscopy and electron backscatter diffraction, in: W. Heinrich, R. Abart (Eds.), Mineral Reaction Kinetics: Microstructures, Textures, Chemical and Isotopic Signatures, 1st ed., Mineralogical Society of Great Britain & Ireland, 2017: pp. 37–95. https://doi.org/10.1180/EMU-notes.16.3.

[125] R.A. Schwarzer, D.P. Field, B.L. Adams, M. Kumar, A.J. Schwartz, Present State of Electron Backscatter Diffraction and Prospective Developments, in: A.J.

Schwartz, M. Kumar, B.L. Adams, D.P. Field (Eds.), Electron Backscatter Diffraction in Materials Science, Springer US, Boston, MA, 2009: pp. 1–20. https://doi.org/10.1007/978-0-387-88136-2_1.

[126] S. Nishikawa, S. Kikuchi, The Diffraction of Cathode Rays by Calcite, Proceedings of the Imperial Academy. 4 (1928) 475–477. https://doi.org/10.2183/pjab1912.4.475.

[127] S.I. Wright, M.M. Nowell, D.P. Field, A Review of Strain Analysis Using Electron Backscatter Diffraction, Microscopy and Microanalysis. 17 (2011) 316–329. https://doi.org/10.1017/S1431927611000055.

[128] A.D. Giddings, S. Koelling, Y. Shimizu, R. Estivill, K. Inoue, W. Vandervorst, W.K. Yeoh, Industrial application of atom probe tomography to semiconductor devices, Scripta Materialia. 148 (2018) 82–90. https://doi.org/10.1016/j.scriptamat.2017.09.004.

[129] K. Thompson, D. Lawrence, D.J. Larson, J.D. Olson, T.F. Kelly, B. Gorman, In situ site-specific specimen preparation for atom probe tomography, Ultramicroscopy. 107 (2007) 131–139. https://doi.org/10.1016/j.ultramic.2006.06.008.

[130] B. Gault, M.P. Moody, J.M. Cairney, S.P. Ringer, From Field Desorption Microscopy to Atom Probe Tomography, in: Atom Probe Microscopy, Springer New York, New York, NY, 2012: pp. 29–68. https://doi.org/10.1007/978-1-4614-3436-8_3.

[131] B. Gault, D.J. Larson, Atom probe tomography: Looking forward, Scripta Materialia. 148 (2018) 73–74. https://doi.org/10.1016/j.scriptamat.2017.11.009.

[132] B. Gault, M.P. Moody, J.M. Cairney, S.P. Ringer, Tomographic Reconstruction, in: Atom Probe Microscopy, Springer New York, New York, NY, 2012: pp. 157–209. https://doi.org/10.1007/978-1-4614-3436-8_7.

[133] Ch. Genzel, I.A. Denks, J. Gibmeier, M. Klaus, G. Wagener, The materials science synchrotron beamline EDDI for energy-dispersive diffraction analysis, Nuclear Instruments and Methods in Physics Research Section A: Accelerators, Spectrometers, Detectors and Associated Equipment. 578 (2007) 23–33. https://doi.org/10.1016/j.nima.2007.05.209.

[134] G.C.A.M. Janssen, Stress and strain in polycrystalline thin films, Thin Solid Films. 515 (2007) 6654–6664. https://doi.org/10.1016/j.tsf.2007.03.007.

[135] C. Genzel, M. Klaus, In-Situ high temperature stress analysis on coated cutting tools by energy-dispersive diffraction performed at the EDDI beamline., Helmholtz-Zentrum Berlin für Materialien und Energie, Berlin, 2017.

[136] C. Kral, W. Lengauer, D. Rafaja, P. Ettmayer, Critical review on the elastic properties of transition metal carbides, nitrides and carbonitrides, Journal of Alloys and Compounds. 265 (1998) 215–233. https://doi.org/10.1016/S0925-8388(97)00297-1.

[137] S. Li, W. Huang, H. Yang, Z. Wang, Plasma chemical vapor deposition of TiN, Plasma Chemistry and Plasma Processing. 4 (1984) 147–161. https://doi.org/10.1007/BF00566838.

[138] T. Arai, H. Fujita, K. Oguri, Plasma-assisted chemical vapour deposition of TiN and TiC on steel: properties of coatings, Thin Solid Films. 165 (1988) 139–148.

[139] K.-T. Rie, A. Gebauer, J. Woehle, Investigation of PA-CVD of TiN: relations between process parameters, spectroscopic measurements and layer properties, Surface and Coatings Technology. 60 (1993) 385–388.

[140] K.-T. Rie, A. Gebauer, J. Wöhle, Plasma assisted CVD for low temperature coatings to improve the wear and corrosion resistance, Surface and Coatings Technology. 86 (1996) 498–506.

[141] B. Arnold, I. Endler, TEM investigation of TiN x-PACVD-coatings, Microchimica Acta. 125 (1997) 83–87.

[142] K. Wetzig, I. Endler, Depth profile analysis of plasma assisted CVD hard materials coatings, Microchimica Acta. 125 (1997) 121–125.

[143] K. Kawata, H. Sugimura, O. Takai, Effects of chlorine on tribological properties of TiN films prepared by pulsed dc plasma-enhanced chemical vapor deposition, Thin Solid Films. 407 (2002) 38–44.

[144] M. Stoiber, E. Badisch, C. Lugmair, C. Mitterer, Low-friction TiN coatings deposited by PACVD, Surface and Coatings Technology. 163–164 (2002) 451–456. https://doi.org/10.1016/S0257-8972(02)00642-4.

[145] S. Takatsu, K. Shibuki, Diffusion of cobalt into a TiC layer during chemical vapour deposition and its effects on the cutting performance of TiC/Al_2O_3-coated cemented carbides, Thin Solid Films. 127 (1985) 283–292.

[146] K. Akiyama, E. Nakamura, I. Suzuki, T. Oshika, A. Nishiyama, Y. Sawada, A study of the adhesion between CVD layers and a cemented carbide substrate by AEM analysis, Surface and Coatings Technology. 94 (1997) 328–332.

[147] S.V. Dudiy, B.I. Lundqvist, First-principles density-functional study of metal-carbonitride interface adhesion: Co/TiC(001) and Co/TiN(001), Physical Review B. 64 (2001). https://doi.org/10.1103/PhysRevB.64.045403.

[148] S.B. Kim, S.K. Choi, S.S. Chun, K.H. Kim, The effects of chlorine content on the properties of titanium carbonitride thin film deposited by plasma assisted chemical vapor deposition, Journal of Vacuum Science & Technology A: Vacuum, Surfaces, and Films. 9 (1991) 2174–2179. https://doi.org/10.1116/1.577246.

[149] K.H. Kim, S.H. Lee, Comparative studies of TiN and $Ti_{1-x}Al_xN$ by plasma-assisted chemical vapor deposition using a $TiCl_4/AlCl_3/N_2/H_2$/Ar gas mixture, Thin Solid Films. 283 (1996) 165–170.

[150] J.M. Tarragó, J.J. Roa, E. Jiménez-Piqué, E. Keown, J. Fair, L. Llanes, Mechanical deformation of WC–Co composite micropillars under uniaxial compression, International Journal of Refractory Metals and Hard Materials. 54 (2016) 70–74. https://doi.org/10.1016/j.ijrmhm.2015.07.015.

[151] S.B. Luyckx, Slip system of tungsten carbide crystals at room temperature, Acta Metallurgica. 18 (1970) 233–236. https://doi.org/10.1016/0001-6160(70)90028-3.

[152] M.K. Hibbs, R. Sinclair, Room-temperature deformation mechanisms and the defect structure of tungsten carbide, Acta Metallurgica. 29 (1981) 1645–1654. https://doi.org/10.1016/0001-6160(81)90047-X.

[153] V. Jayaram, R. Sinclair, D.J. Rowcliffe, Intergranular cracking in WC-6% Co: An application of the von mises criterion, Acta Metallurgica. 31 (1983) 373–378. https://doi.org/10.1016/0001-6160(83)90214-6.

[154] T. Csanádi, M. Bl'anda, N.Q. Chinh, P. Hvizdoš, J. Dusza, Orientation-dependent hardness and nanoindentation-induced deformation mechanisms of WC crystals, Acta Materialia. 83 (2015) 397–407. https://doi.org/10.1016/j.actamat.2014.09.048.

7. Included papers

7.1 Paper I

Investigations on micro-mechanical properties of polycrystalline Ti(C,N) and Zr(C,N) coatings

I. El Azhari, J. Garcia, M. Zamanzade, F. Soldera, C. Pauly, L. Llanes, F. Mücklich

Acta Materialia. 149 (2018) 364–376

https://doi.org/10.1016/j.actamat.2018.02.053

Acta Materialia 149 (2018) 364–376

Contents lists available at ScienceDirect

Acta Materialia

journal homepage: www.elsevier.com/locate/actamat

Full length article

Investigations on micro-mechanical properties of polycrystalline Ti(C,N) and Zr(C,N) coatings

Idriss El Azhari [a, b], José Garcia [c, *], Mohammad Zamanzade [d], Flavio Soldera [a], Christoph Pauly [a], Luis Llanes [b], Frank Mücklich [a]

[a] Functional Materials, Department of Materials Science and Engineering, Saarland University, Campus D 3.3, D-66123 Saarbrücken, Germany
[b] Materials Science and Metallurgical Department (CIEFMA), Barcelona East School of Engineering (EEBE), Universitat Politècnica de Catalunya, 08019 Barcelona, Spain
[c] Sandvik Coromant R&D, SE-126 80 Stockholm, Sweden
[d] Materials Science and Methods, Department of Materials Science and Engineering, Saarland University, Campus D 2.2, D-66123 Saarbrücken, Germany

ARTICLE INFO

Article history:
Received 7 November 2017
Received in revised form
7 February 2018
Accepted 24 February 2018
Available online 2 March 2018

Keywords:
CVD coatings
Micro-compression
Plasticity
Zr(C,N)
Ti(C,N)
EBSD

ABSTRACT

Micro-mechanical properties of Ti(C,N) and Zr(C,N) coatings deposited by chemical vapor deposition on a WC-Co cemented carbide substrate were examined by micro-compression testing using a nanoindenter equipped with a flat punch. Scanning Electron Microscopy, Focused Ion Beam, Electron Backscattered Diffraction and Finite Element Modeling were combined to analyze the deformation mechanisms of the carbonitride layers at room temperature. The results revealed that Ti(C,N) undergoes a pure intergranular crack propagation and grain decohesion under uniaxial compression; whereas the fracture mode of Zr(C,N) was observed to be inter/transgranular failure with unexpected plastic deformation at room temperature.

1. Introduction

The increase of production efficiency in metal cutting industry is vital for the reduction of manufacturing costs. This can be achieved by developing coated cemented carbide systems that can withstand high cutting speeds and severe service conditions. Hence, the strategy is to focus not only on the design of new cemented carbide substrate, but also on the design of thin hard films with optimized properties by tailoring their composition, texture and particle size among others [1]. Moreover, both high hardness and adequate toughness are essential for the thin layers and their combination with the cemented carbide substrate [2], given that high hardness comes at the expense of toughness and vice versa [3].

The present study deals with micro-mechanical investigations of transition metal Zirconium and Titanium carbonitrides (Zr(C,N) and Ti(C,N) respectively) coatings deposited by chemical vapor deposition (CVD) on Tungsten carbide-Cobalt bonded (WC-Co) cemented carbide. They both have good combination of high hardness and adequate toughness [4] and comparable physical properties [5,6]. However, they present different performances during metal cutting applications [7]. Then, in order to understand this different wear behavior, it is of great importance to investigate their deformation mechanisms at the micro-scale, such that micro-mechanical response may be correlated to microstructure features.

Studies on single crystalline and sintered transition-metal carbides (TMC) flourished between the 60s and the 80s due to historical reasons [8]. The focus was on studying the mechanical properties and plasticity at high temperature of these compounds [9–18] because of their outstanding potential in extreme environment such as aerospace applications and metal cutting industry. From the late 90s on, as it was understood that different hybrid properties (ceramic and metal-like) in these materials originate from their electronic structures and atomic bonding, and with the boost of computing capabilities, extensive fundamental research based on first principles calculations has been conducted to explain their mechanical and physical properties [19–29]. In general, it is agreed that the TMC are ductile at high temperatures, yet they are brittle at room temperature and fail through cracking because of

* Corresponding author. Tel.: +46 70 616 7194.
E-mail address: jose.garcia@sandvik.com (J. Garcia).

https://doi.org/10.1016/j.actamat.2018.02.053
1359-6454/

limited or absence of dislocation activity. Recently, Kiani et al. have proven through Transmission Electron Microscopy in-situ compression of ZrC single crystals that they deform, indeed, plastically at room temperature through dislocation motion along two active slip systems [27].

Nanoindentation is the standard and most frequent method used to characterize mechanical properties of thin film materials [30]. Accordingly, studies on deformation mechanisms of thin films variants of transition-metals carbides/nitrides (TMC/N) were mainly performed through micro/nano-indentation experiments combined with modeling [31–36]. Intergranular shear sliding is identified as a common and important failure mechanism in these studies. Nevertheless, investigation of the deformation mechanisms from the residual imprints is not always easy because of the multi-axial stress-strain created during indentation [37–41]. Micro-compression test has shown to be a more adaptable method to investigate the micro-mechanics on a small defined geometry [42], and it has the advantage - over nanoindentation - of a relatively more uniform stress-strain field [41]. This testing technique has gained increased interest in the recent years to acquire knowledge on the micromechanics that govern deformation mechanisms in different classes of materials [40,42,43], including brittle materials as the biggest challenge of premature failure during testing is circumvented by the miniaturization of the tested size [44]. However, this technique is fundamentally used to characterize single crystalline materials. Analogous studies for hard coatings are scarce, and to the best knowledge of the authors, micro-compression investigations of polycrystalline hard coatings are limited to few studies [30,45–50], and for transition metal carbonitrides are rather missing.

In order to fill the missing gap of the current knowledge in terms of deformation mechanics of TMCN, we present and compare results on deformation of hard coatings (Ti(C,N) and Zr(C,N)) during micro-compression. The target is to reveal which are the microstructural features that controls the mechanical properties and deformation behavior in polycrystalline coatings produced in industrial CVD reactor. The study is mainly composed of two sections. The first one presents the general results and basic observations, which are the starting point for the upcoming discussions. In the second section, the influence of the adopted experimental protocol on the results is reviewed based on Finite Element Modeling (FEM) and other investigations. Then, the deformation mechanism of each carbonitride coating is presented based on Scanning Electron Microscope (SEM) and Electron Backscattered Diffraction (EBSD) results.

2. Experimental

2.1. Coating deposition

Each $Ti(C_{0.5},N_{0.5})$ and $Zr(C_{0.5},N_{0.5})$ coating was deposited on a WC-6wt%Co substrate at around 900 °C in a hot wall CVD reactor using $TiCl_4$, $ZrCl_4$, CH_3CN and H_2 as gas precursors. The final thickness of the coating was 5 μm. A thin TiN layer of 0.3 μm was previously deposited on the cemented carbide to enhance the adherence of the carbonitride coating and hinder reactions and diffusion with the substrate. (See Fig. 1). Mechanical properties of the materials taken from literature are shown in Table 1.

2.2. Pillar milling

Because a flat and roughness free surface is required for pillars fabrication, the surface topography inherited from the coating growth process was gently smoothed by a stepwise polishing up to 1 μm. To avoid damaging the coating and limit the residual stress changes - which could be inflicted during polishing - low rotation speed and force were applied with the use of a diamond suspension (ranging from 9 μm to 1 μm) sprayed on polishing cloth. The sample was then mounted in a FEI Helios Nanolab Dualbeam 600 SEM/FIB that operates with gallium (Ga) ion beam. To achieve the final shape of the pillars, three annular milling steps are used with a current decreasing from 21 nA, 0,92 nA to 0,28 nA. Many challenges were faced during the milling as the following scope statement must be respected for reproducible experiments: (a) A standard aspect ratio of 1/3 (diameter/height) should be maintained [51]. (b) The pillar must be based and emerging from the coating (i.e. direct contact with the substrate must be avoided) to reduce as much as possible the substrate compliance and response during compression (Fig. 1 (a), (b)). Because of the latter condition, the pillars have a relatively higher tapering angle varying from 4° to 6° since an additional fine-milling step to reduce the tapering would mill the whole layer and reach the cemented carbide substrate. Subsequently, the final pillar diameter ranges from 1 μm to 1.1 μm and the length from 3 μm to 3.4 μm. Our effort came up short to suppress the irregularities at the pillar base, as it is an intrinsic property of the coating itself related to the orientation of the grains that influences the material removal rate (Fig. 1 (c)).

2.3. Compression test

Compression tests were performed with the aid of a Hysitron Tribo-Indenter TI 900, equipped with a Performech controller and a 5 μm diamond flat punch. The loading function is a displacement controlled with a constant rate of 3 nm/s and a maximum depth of 120 nm. Twelve pillars were tested for each coating following the same experimental strategy.

After the compression test, inspection was conducted with Scanning Electron Microscopy (SEM). The irregularities around the pillar and the non-flat base surface make the determination of the actual pillar height very difficult. Hence, the numerical estimation of engineering strain was not possible to determine with a simple equation and requires rather Finite Element Modeling (FEM) for each case. As mentioned above, further fine milling could suppress easily both the tapering and irregularities; nevertheless, the pillar would be based on the substrate and the assessment of the pillar's referred base (for strain calculation) will remain still not accessible, as the pillar would be in this case partly submerged in the substrate.

Therefore, the engineering stress (quotient of applied force and the top area of the pillar) versus displacement are the chosen parameters for the representation of the curves. We note that the raw data is plotted without fitting or smoothing the curves.

2.4. Finite element analysis (FEM)

A 3D finite element analysis with ANSYS APDL was done to have an overview of the stress distribution, the elastic deformation and the interaction between the pillar, coating, bonding layer and the substrate during the compression test. The polycrystallinity of the coatings and multiple phases in the substrate phases were reduced to an isotropic and homogeneous condition for each material. The different properties of the coatings were taken from Ref. [6] and for the substrate from the Sandvik Coromant R&D database (Table 1). A displacement controlled loading function was simulated.

2.5. Electron backscattered diffraction (EBSD) characterization

Analysis of compressed pillars (in terms of cracking, microstructure and deformation) was conducted on a lamella taken from the pillar and prepared with a procedure similar to the one used for preparation of Transmission Electron Microscopy (TEM) samples.

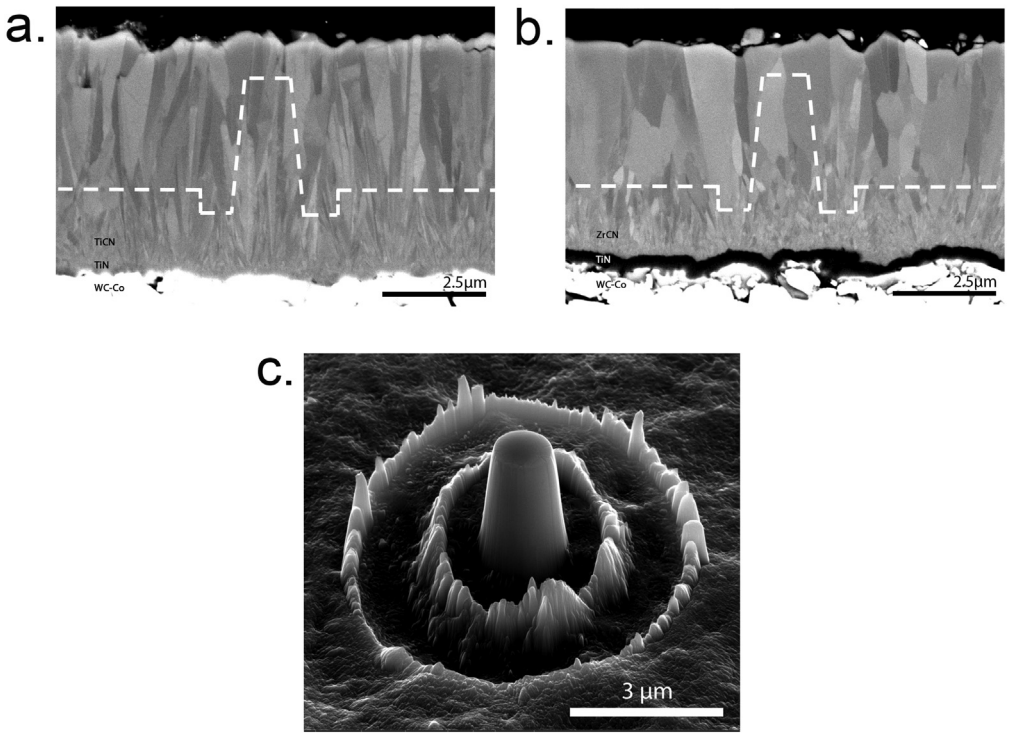

Fig. 1. (a) Cross section image (SEM) of Zr(C,N) and (b) Ti(C,N) coatings investigated. Surface topography can be seen at the edge. White dashed line indicates the position where pillars were milled. (c) Final pillar shape milled from Ti(C,N) coating.

Table 1
Mechanical properties of different materials (* [6];** Sandvik Coromant database).

Material	Young's modulus E (GPa)	Shear modulus G (GPa)
$Zr(C_{0,5},N_{0,5})^*$	405	172
$Ti(C_{0,5},N_{0,5})^*$	463	194
TiN*	465	189
WC-Co**	626	257

First, the pillar was covered by Platinum (Pt) which was deposited with Electron Beam Induced Deposition (EBID) and subsequently with Ion Beam Induced Deposition (IBID). In this way, the surface of the pillars was not damaged when working with ions for cutting and transferring the lamella and sharp edges could be maintained during the final polishing with ions. This lamella was milled at the pillar center with Focused Ion Beam (FIB), lifted out with an OmniProbe 100 manipulator and deposited on a TEM grid holder for final polishing on a single side only, leaving the sample rather thick (about 500 nm) since electron transparency is not required. Finally, EBSD was conducted in reflection mode with an EDAX Hikari system. As the EBSD surface is very sensitive to surface condition [52], low current and acceleration (11 pA and 5-2 kV respectively) voltage was used during the final polishing of the lamella in order to minimize any possible damage with Ga^+ ions.

Diffraction patterns were obtained in reflection mode at 20 kV acceleration voltage, 11 nA current and a 20 nm step size. Subsequently the raw data was processed and analyzed with OIM 7™ Data Analysis software. The processing consists of defining a grain as an island of at least five adjacent points with a maximum misorientation of 5°. Afterwards the confidence index (CI) was standardized across each grain and finally noise and poor data were filtered by a cut-off of CI = 0.09. No morphological operation (e.g. dilation operation) was used to enhance the representability of the EBSD maps.

The choice of EBSD for orientation imaging comes from the fact that it has a series of advantages over conventional TEM (i.e. using the spot diffraction patterns), among others being faster, automated for mapping, easier and with higher angular accuracy [53]. Moreover, it provides additional information about the long range and short range misorientation character like Kernel Average Misorientation (KAM) [54] and is more adapted for studying polycrystalline materials (Since for TEM, the sample has to be tilted according to the zone axis of each grain).

3. Results and discussion

3.1. Stress-displacement curves

3.1.1. Ti(C,N) coating

The deformation of pillars starts with a linear regime followed by pop-ins (or strain bursts), afterwards catastrophic failure occurs immediately (see Fig. 2 (a)). Indeed, if we consider the pop-in load state as the yield strength, then a high yield strength of 14 GPa was reached which is comparable to some of the highest yield values reported on compression tests of hard materials: CrAlN/Si_3N_4 (16 GPa) [47], ZrB_2 (13.4 GPa) [55], GaN (7.8 GPa) [56] and WC (6.6 GPa) [57]. No clear deformation insight could be extracted after complete destruction of the pillar apart from the fact that the debris have the shape of the initial columnar grains (see Fig. 2 (b)). Thus, to preserve the pillar integrity after the compression test and to unveil the origin of pop-ins, the flat punch was quickly unloaded after the appearance of a pop-in in the stress-displacement curve.

Subsequently, using this method has enabled, on the one hand, the observation of the deformation inflicted on pillars and, on the other hand, to correlate the observed event in the curves to the changes of the pillars. Fig. 3 shows intergranular crack formation at the circumference of the pillar after appearance of the pop-in.

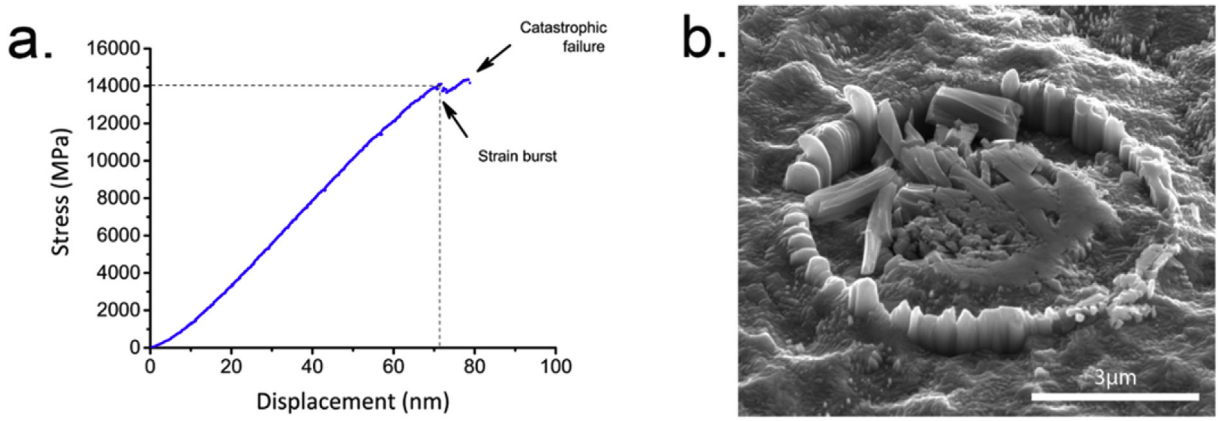

Fig. 2. (a) Stress-displacement of a Ti(C,N) pillar (b) Destroyed Ti(C,N) pillar after completion of the loading function.

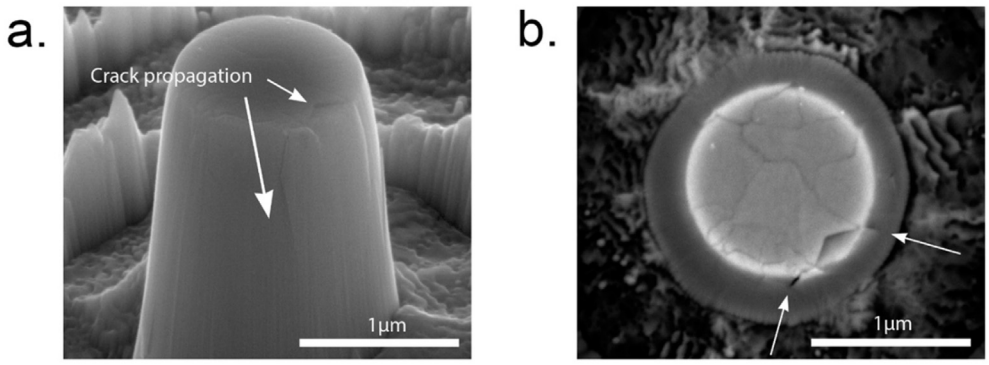

Fig. 3. (a) Cracks (white arrows) at the sides of Ti(C,N) pillar following intergranular path which can be seen in the corresponding top view in (b).

3.2. Zr(C,N) coating

For the Zr(C,N) coatings the curves look in general similar to Ti(C,N); the curves start with linear behavior followed by a pop-in. Thereafter, if the experiment is not terminated, a catastrophic failure will take place. However, two major differences compared to the behavior of Ti(C,N) coatings were noticed: (a) The stiffness of Ti(C,N) coating is higher than the Zr(C,N). (b) The cracking related to the pop-ins is different, in comparison to Ti(C,N), which is generally partial cracking on the top surface following an undefined pattern giving the impression of a mixed inter/intragranular propagation behavior (see Fig. 4 (b) and (c)).

Fig. 5 (a) (which presents a summary of all the curves for both coatings) indicates that stress-displacement curves are reproducible and similar with a leaning for each coating. The ultimate strength is similar among most of the curves, however, the pop-ins occur at higher displacements for Zr(C,N) which is an indication of superior toughness compared with Ti(C,N). The small disparities within each coating family are more related to the variations of tapering angle from one pillar to another, which affects the stiffness directly. Fei et al. [41] have shown that if the tapering angle is lower than 5°, then its effect is negligible on the stress. The same tendency can be recognized in Fig. 5 (b) where the slope of stress-displacement curves are plotted against the tapering angle of each pillar. We observe that when the tapering angle is higher than 5° the disparities between the points increase.

3.3. Influence of the substrate during compression

Depending on the experimental setup, the base substrate below

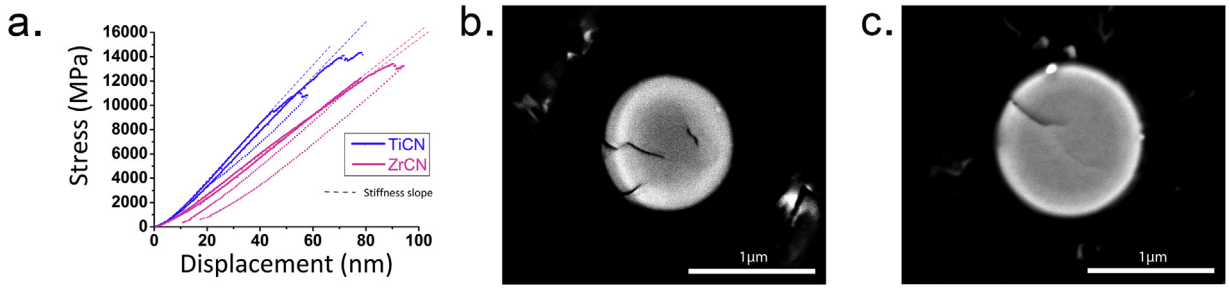

Fig. 4. (a) Stress-displacement for selected Ti(C,N) and Zr(C,N) pillars, the stiffness slope is extended. (b), (c) Top view of two Zr(C,N) pillars after compression. The crack propagation mode seems to be a mixed inter/intragranular mode.

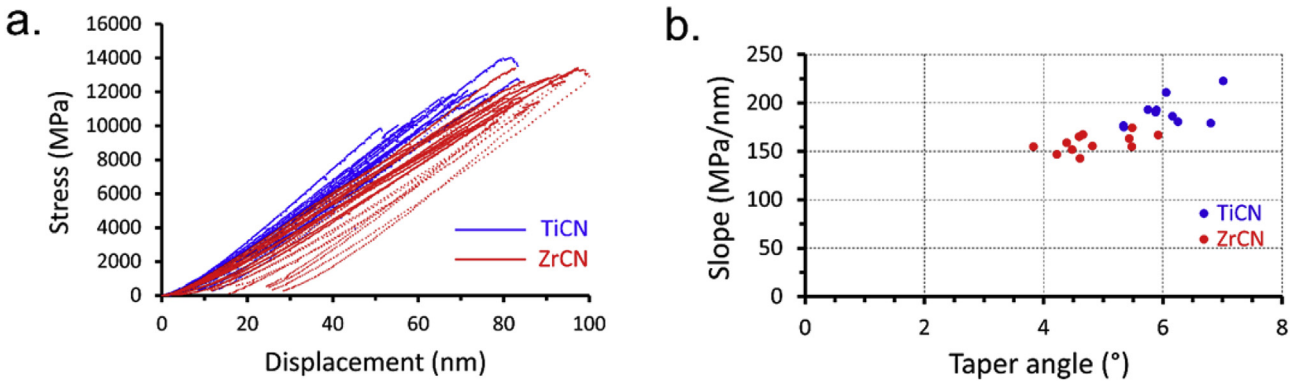

Fig. 5. (a) Recap of all stress-displacement curves. (b) Slope of stress-displacement curve vs tapering angle.

the coating can have a major impact during compression. Thereby, the deformation mechanisms of the pillar coating can be influenced and the stiffness will be affected [46]. In the present study, sink-in of the pillar during compression is reduced by higher taper angle [41]. Indeed, the deformation could be probed also from the substrate instead. On the one hand, the topography of the substrate at the micrometric scale is wavy and we could have a pillar based directly or very close to the substrate even if the pillar's base is not showing any trace of it. On the other hand, the local properties of the cemented carbide may not be uniform owing to a randomly distributed WC grains in a cobalt matrix [58]. To investigate these effects, serial cross sections with the FIB were conducted for a destroyed pillar, which has been stressed up to 14 GPa (Fig. 6 (a)). The cross section in Fig. 6 (b) shows that 1 μm coating (including the TiN bonding layer) separates the pillar from the substrate and no damage was detected in the vicinity of the supporting coating even with the diamond flat punch crushing of the debris against the supporting coating during catastrophic failure. This result is in a good agreement with finite element modeling. We can see in Fig. 7 that the major displacement/deformation is localized and maximum at the pillar top part, and it is compressive following a gradient along the Y axis. More importantly in this discussion, the displacement is confined within the carbo-nitride coating, which is in consistency with our experimental setup. Thereby, considering these results, cracking of the supporting interlayer (between the substrate and the pillar) during pillar's compression is discarded.

In case the pillar is sitting directly on very soft spot on the substrate (formed mainly by cobalt), the pillar acts as an extension of the flat punch and consequently the substrate is indented/probed first because it is softer than the coating, then at a certain stress state the coating starts to deform. This assumption is proven in comparing the curves of a compliant WC-Co substrate pillar, a Ti(C,N) pillar settling on a similar WC-Co substrate and a normal pillar (Fig. 8). We notice clearly that the first half of the red curve (corresponding to the coating pillar based on the substrate) overlaps the substrate curve (green curve), then at a higher stress the slope of the red curve becomes more regular and similar to the normal pillar curve (blue). In short, this means that in case that a pillar is located near a softer substrate spot, we will see a non-linear stress-displacement curve during the early stages, and then this result will be discarded.

3.4. Deformation mechanisms

The discussion of the results must consider that the pillar compression is performed on a polycrystalline material with a variety of grain sizes including small and bigger crystals, which means that every pillar has different distribution of grain size, crystal orientations and defects (CVD cooling cracks). This fact makes each pillar to respond relatively different toward the applied load. Besides, it has been reported that the scattering of the results increases as the size of the pillar approaches the microstructural dimensions [30,45,59].

3.4.1. Deformation mechanisms of Ti(C,N)

For Ti(C,N) an elastic deformation was first observed, followed by the pop-in which corresponds to crack initiation between the grains (Fig. 2). It is then suggested that the failure takes place according to purely columnar grain dissociation or intercolumnar cracking.

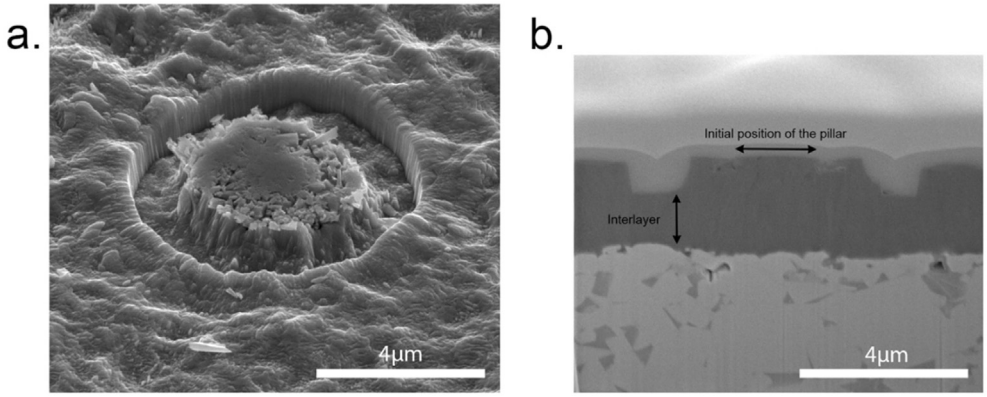

Fig. 6. (a) Destroyed Ti(C,N) pillar after compression. (b) Corresponding FIB cross section showing no damage in the supporting interlayer.

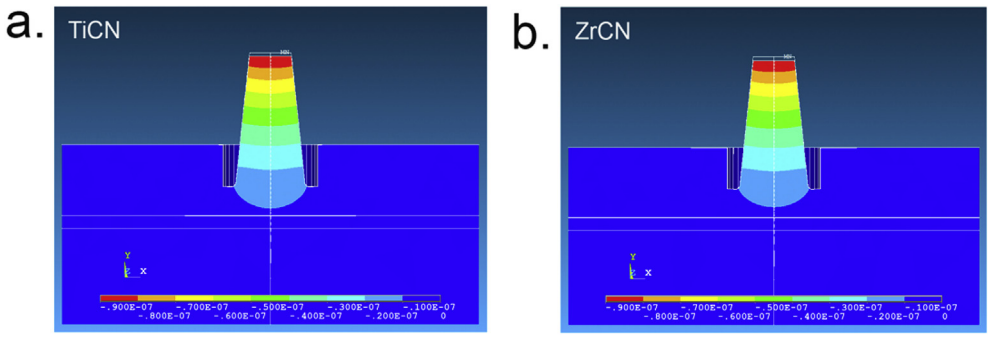

Fig. 7. FEM model of Uy displacement (m^{-1}) at 90 nm penetration depth for Ti(C,N) (a) and for Zr(C,N) (b).

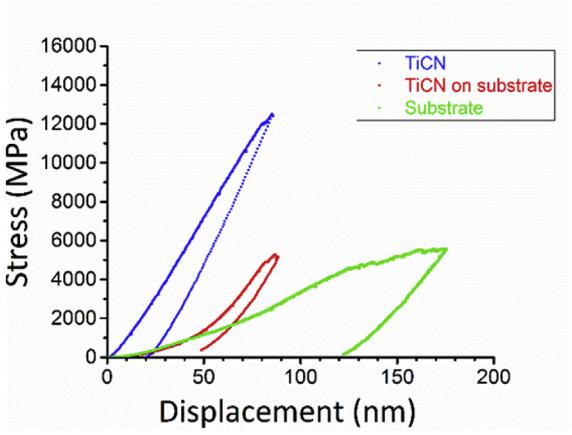

Fig. 8. Comparison of deformation between three assemblies: Normal experimental Ti(C,N) pillar (blue curve), Ti(C,N) pillar settling directly on a substrate (red curve) and a pillar carved from a substrate. (For interpretation of the references to colour in this figure legend, the reader is referred to the Web version of this article.)

Yong et al. [35], performed nano-indentation with a spherical diamond indenter to investigate the failure modes of Ti(C,N) coating. They also stated inter-columnar cracking along the grain boundary as the first failure event, which took place as the indentation load increased. The location of these cracks within the Ti(C,N) layer corresponded to the highest calculated strain energy density with FEM. Calculating the same parameter in our FEM model in Fig. 9, we find out that inter-columnar cracking occurred at the apex part where also maximum strain energy density was calculated.

Similar columnar grain decohesion during pillar compression has been reported by Zou et al. [45] for Nb-Mo-Ta-W high entropy alloys (HEA) having similar characteristics (polycrystalline, columnar structured, generally brittle at room-temperature and high yield strength). They noticed that pillars having a diameter more than 1 μm experienced cracking at the top and cracks propagate along the grain boundaries showing intergranular fracture. They draw an analogy to bundled bamboos to describe the structure of the columnar grains inside the pillar, and suggested that it is like if the compression was performed on a discrete array of single-crystalline pillars, and if the deformation in each grain cannot be accommodated by its neighbors, it may lead to crack initiation along the grain boundaries [45]. The reason behind this mechanism could be attributed to the low cohesive strength at the grain boundaries of this HEA alloy [45,60,61].

In Fig. 10, an example that endorses strongly this assumption is shown. The post-compression SEM images of Ti(C,N) pillars shows an evident decohesion of the grains and cracks follows perfectly the intergranular pattern. This extended decohesion is translated by a non-linear stress-displacement curve after elastic part (Fig. 10 (c)). Furthermore, topography/steps on the pillar top surface is spotted which is probably attributed either to the grain sliding or to the elastic recovery (after unloading) that became specific to each grain orientation after dissociation.

Summarizing the deformation mechanism of the Ti(C,N) pillar can be resumed as following: in the beginning the polycrystalline Ti(C,N) pillar deforms elastically toward the applied load as one structure. As the deformation continues, the stress is accumulating at the grain boundaries as they are the weak spots in the structure and also because each crystal has a specific stiffness (according to its orientation). When higher stresses are reached, the grains begin to slide along the grain boundaries. Then, at a given critical load, cracks will initiate at the top face of the pillar as a result of maximum strain energy in this region, then they will propagate along the columnar grain boundaries which causes grain decohesion and finally catastrophic failure (Fig. 2 (b)).

3.4.2. *Deformation mechanisms of Zr(C,N)*

The fracture images of the Zr(C,N) pillars showed that the crack pattern is different compared to the Ti(C,N) pillars (discontinuous partial cracking and undefined pattern (Fig. 4)). It can be assumed that the crack propagation shows a rather random pattern and mixed mode (inter/intragranular). In addition, no decohesion and no steps (on the top face) between the grains were seen, and the cracks were fine and difficult to observe (in some cases) which may indicate a high cohesive strength between the grains. Nevertheless, two important facts were noticed during the compression of Zr(C,N) compared to Ti(C,N). First, few pillars did-not show pop-ins even at stresses exceeding 12 GPa. SEM examination of the pillars after compression test did not reveal any structural changes in the pillars. This led us to retest these resistant pillars until a pop-in took place. Surprisingly, when comparing the curves of the 1st and 2nd compression (Fig. 11) the outcome was a strain hardening behavior like the one observed in metals. This may be considered as a clear indication of a plastic deformation for Zr(C,N) pillars. The second fact was that in one Zr(C,N) pillar endured material extrusion at the top ring and buckling was also recognized at the same side (Fig. 12 (a)). To investigate the deformation mechanism, a cross section was performed at the middle of the pillar and interestingly buckling was noticed at the right side (Fig. 12 (b)). Afterwards, a lamella was extracted from this pillar to observe closely the inner microstructure with EBSD (Fig. 12 (c)). Similar procedure was done for a deformed Ti(C,N) pillar (Fig. 12 (d–f)) and both results are compared and discussed in the following section.

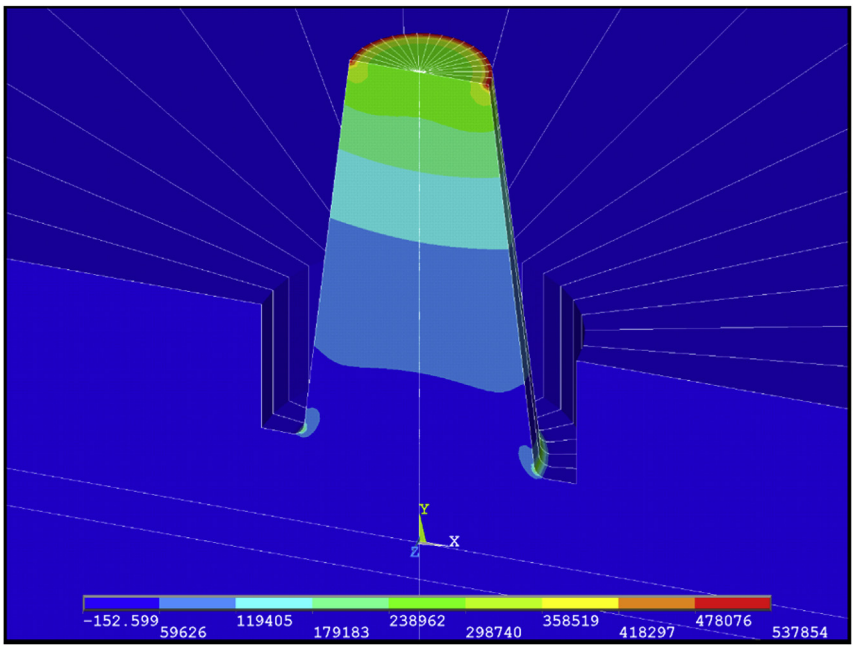

Fig. 9. FEM model of strain energy density (J/m^3) at 90 nm penetration depth. The energy density is maximum at the circumference of the pillar's apex region.

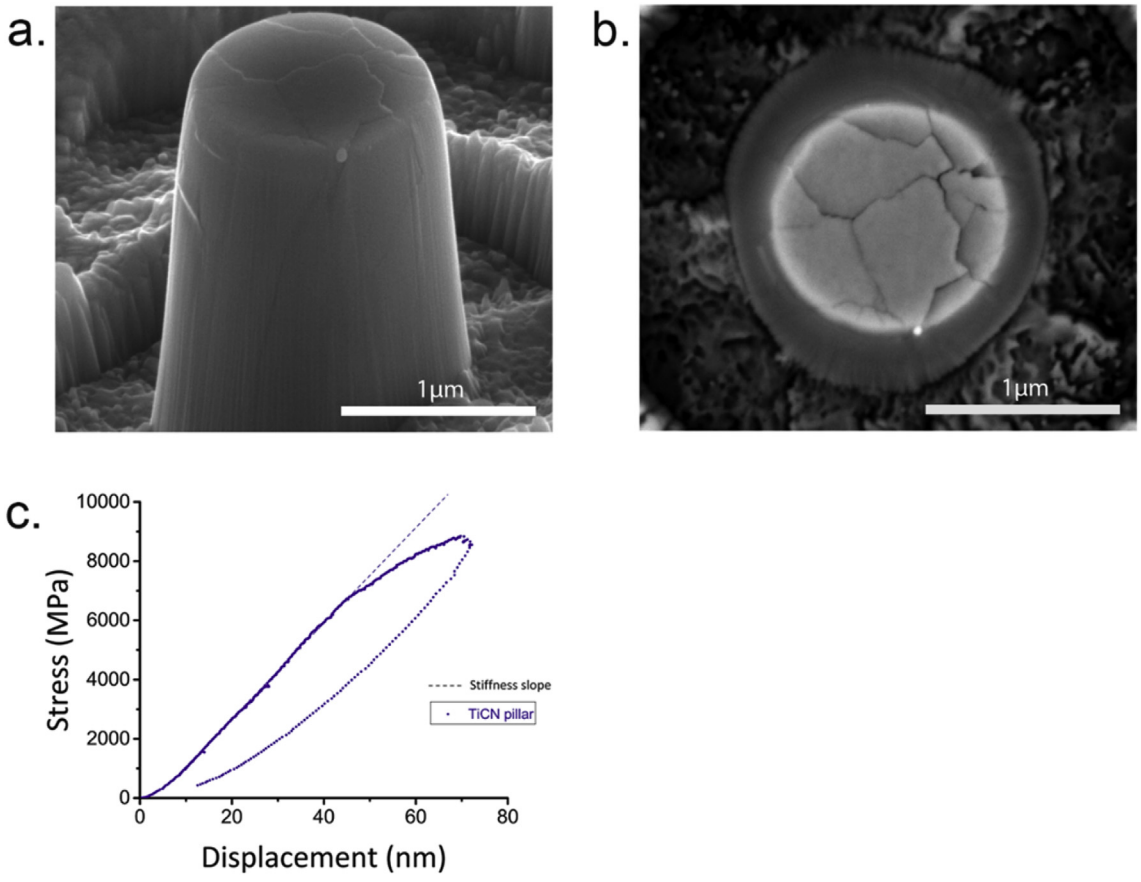

Fig. 10. (a) Topography steps on the top surface of the pillar indicating grain slide or independent elastic recovery for each single grain. (b) Associated top-view showing decohesion of the grains and cracks following intergranular patterns. (c) Corresponding stress-displacement curve showing non-linear behavior due to grain sliding.

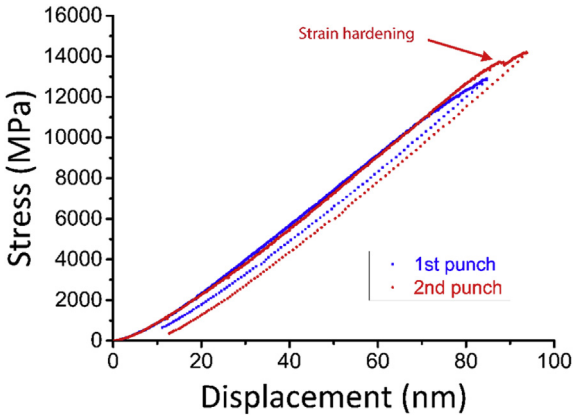

Fig. 11. Comparison between two successive compression tests for a Zr(C,N) pillar. Strain hardening is perceived during the 2nd punch.

3.5. EBSD analysis

3.5.1. Inverse pole figure (IPF)

Fig. 12 (c) and (f) presents the IPF map of Zr(C,N) and Ti(C,N) pillars after the compression tests respectively. Polycrystallinity, randomness of the texture and the columnar microstructure of the pillars are visible. The Zr(C,N) has a buckled shape compared to Ti(C,N) especially at the right side where we can see that the obvious buckling (Fig. 12 (b)) is coming from a single elongated grain.

3.5.2. Schmid factor

The Schmid factor was calculated (Fig. 13) individually for each grain considering a perpendicular compression and presumably one active slip system: $\{001\}\,110$ for Zr(C,N) [11,27] and $\{110\}\,1\bar{1}0$ for Ti(C,N) [14,28]. Due to the scarcity of data in carbonitride systems and the similar properties between carbides and carbonitrides, this data was taken from ZrC and TiC respectively. We would like to emphasize here that for ZrC, Schmid factors were calculated by considering only one slip system as, on the one hand, it is the favorable one due to easy shear in comparison to $\{110\}\,1\bar{1}0$ [27] and, on the other hand, we wanted to test minimal conditions to expect activation of slip systems in ZrC grains.

High Schmid factor means that either the proper orientation (before compression) was favorable for plastic deformation or that it is a result of a crystal rotation. For Zr(C,N), interestingly, maximum Schmid factor is observed at the grain where material extrusion originated from, and the buckled grain (at the right side of the pillar) exhibits a gradient of the Schmid factor (Fig. 13 (a)). Moreover, by comparing the distributions in Fig. 13 (d), we can discern a higher and sharp Schmid factor distribution for Zr(C,N) shifted to high values that are close to the maximum theoretical value of 0.5. In other words, in contrast to Ti(C,N) (Fig. 13 (b)) where random values are spread over the map and the corresponding distribution is spread, Zr(C,N) grains with high Schmid factor corresponds to the areas where deformation was observed. These observations are an indication that higher Schmid factors are not only related to the initial state, but also as a result of grain rotation. Arguably, in our experiments the pillar (as one structure) would in extreme conditions experience a maximum strain of 3.3% and it is far from causing such grain rotation effect. However, again we draw the attention that, on the one hand, the pillar has tapered geometry, which results in a concentration of most displacement at the upper part. On the other hand, the pillar is composed of polycrystalline grains, which are depending on the orientation, grain size, contiguity to other grains and location in the pillar, are more or less prone to deform. Accordingly, to have a better insight, the calculation of a misorientation parameter will be of relevance.

3.6. Misorientation analysis

Misorientation is considered to be an indication of strain distribution in the material [62]. Besides, earlier studies on FCC materials have shown that the increase of misorientation is linearly related to the square root of the strain ($\theta \propto \sqrt{\varepsilon}$) during cold deformation [54,63,64], and it was experimentally proven that when the strain increases, the misorientation distribution is shifted toward higher angles and the angular spread increases as well [54,63,65].

In Fig. 14, misorientation mapping is used to calculate the misorientation of each pixel within a grain with respect to a user defined reference point (selected at the bottom of each grain). This parameter was calculated for both Ti(C,N) and Zr(C,N) and has given a strong confirmation of the postulated presumptions.

A clear misorientation gradient is visible along the loading vertical axis for Zr(C,N) grains, not only on particular regions but rather on the entire pillar structure. Actually, this misorientation tendency is not related to the deposited state but rather to the deformation, since firstly, the observed vertical gradient cannot be produced by thermal residual stresses, which are acting horizontally; and secondly, residual stresses are relaxed gradually during successive annular milling of the pillar [66,67] and during the lamella preparation [68]. Therefore, the observed gradient means that not only some grains underwent a deformation, yet every component had absorbed the strain energy plastically. However, as discussed before, some grains are more prone to deform than others. To highlight the strong gradient in misorientation, a line is sketched to calculate the profile vector on each map and the result is presented in Fig. 14 (c) where we can see quantitatively the strong gradient within Zr(C,N) grains. Similar deformation gradient was observed in the FEM model of strain energy density (Fig. 9).

The occurrence of gradients is a sign that the grains have undergone a partial rotation to accommodate the strain energy. In a study about the development of gradient orientations at different grain scales Gurao et al. [69] confirmed that in microcrystalline FCC grains, plastic deformation is carried by crystallographic slip that contributes to evolution of orientation gradients through the formation of Grain Boundary Affected Zone (GBAZ) that takes over a major fraction of the entire grain [69]. Same observation is valid for Zr(C,N) grains in the pillar investigated, knowing that Zr(C,N) is an FCC rock salt structure where C and N atoms occupy interstitial octahedral sites [70], and generally transition metal carbides deform on slip systems analogous to FCC metals [71]. Particularly, it was reported that the mechanical response of ZrC in compression is similar to FCC metals rather than a B1 structured ionic compound [27].

Another misorientation parameter called Kernel Average Misorientation (KAM) was calculated. It has been shown that the latter is correlated to the deformation of the microstructure and can be used to study the evolution of the substructure during deformation [54,69]. Analyzing the results in Fig. 14 (d), we can see that the KAM distribution is shifted and slightly wider for Zr(C,N) compared to Ti(C,N). It may appear that the difference is more or less small, however, the KAM was calculated across all the grains in the pillar and also similar differences can be observed for Nickel subjected to increasing strain [54]. Besides, it has been stated that a good correlation between Schmid factor and KAM values [69] exists. Then looking back at the higher Schmid factor results, there is a clear indication that the strain has contributed to this higher propensity. We emphasize that the references cited for the gradient formation in the microstructure are for FCC materials deformed

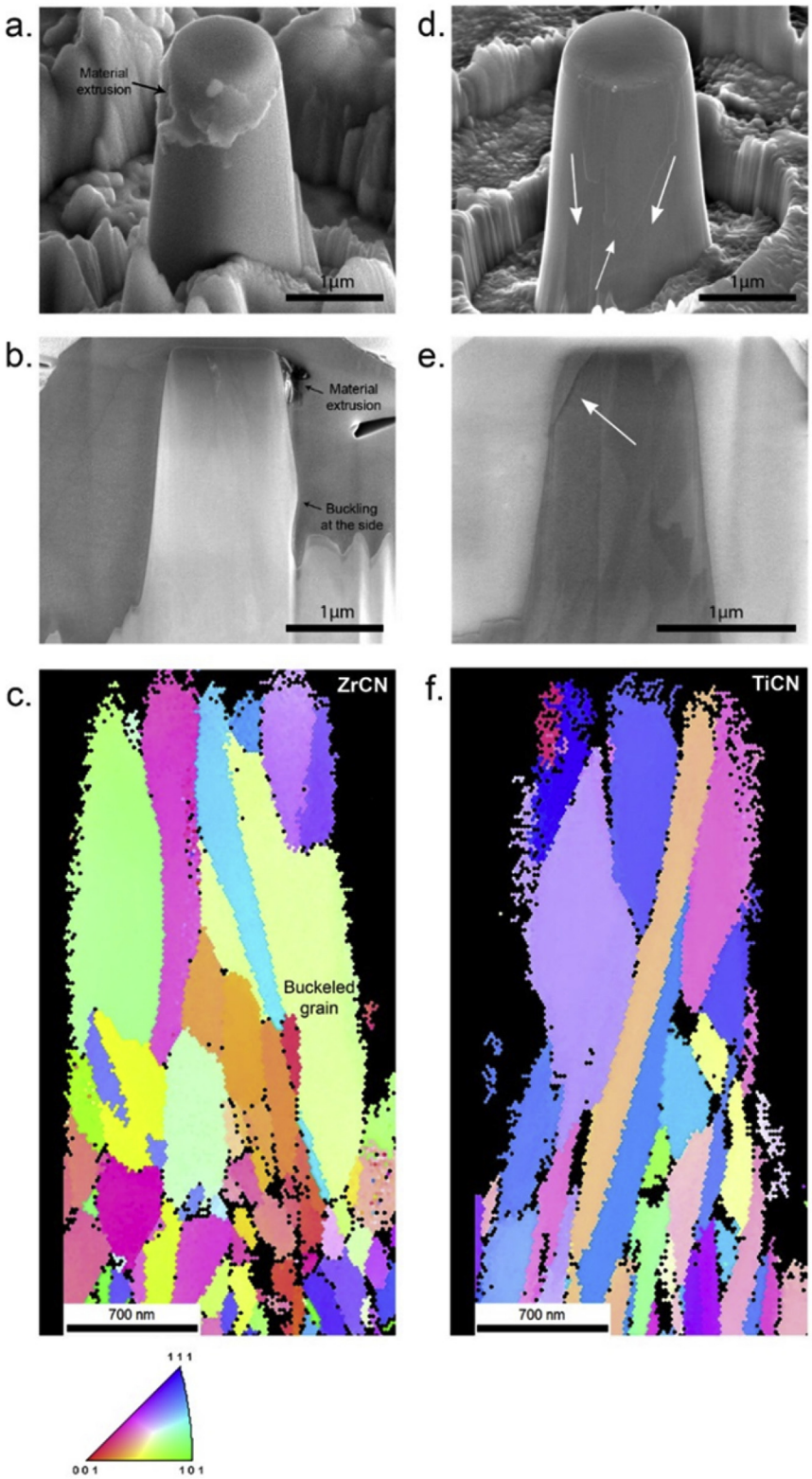

Fig. 12. Comparison of yielding events between Zr(C,N) (a–c) and Ti(C,N) (d–f). (a) Yielding at the top side part of a Zr(C,N) pillar. (b) Corresponding FIB cross section according to the vertical axis at the middle. (c) Corresponding Inverse Pole Figure map along the vertical axis. (d) Grain slide at the side of a Ti(C,N) pillar. (e) Corresponding FIB cross section according to the vertical axis at the middle. (f) Corresponding Inverse Pole Figure map along the vertical axis.

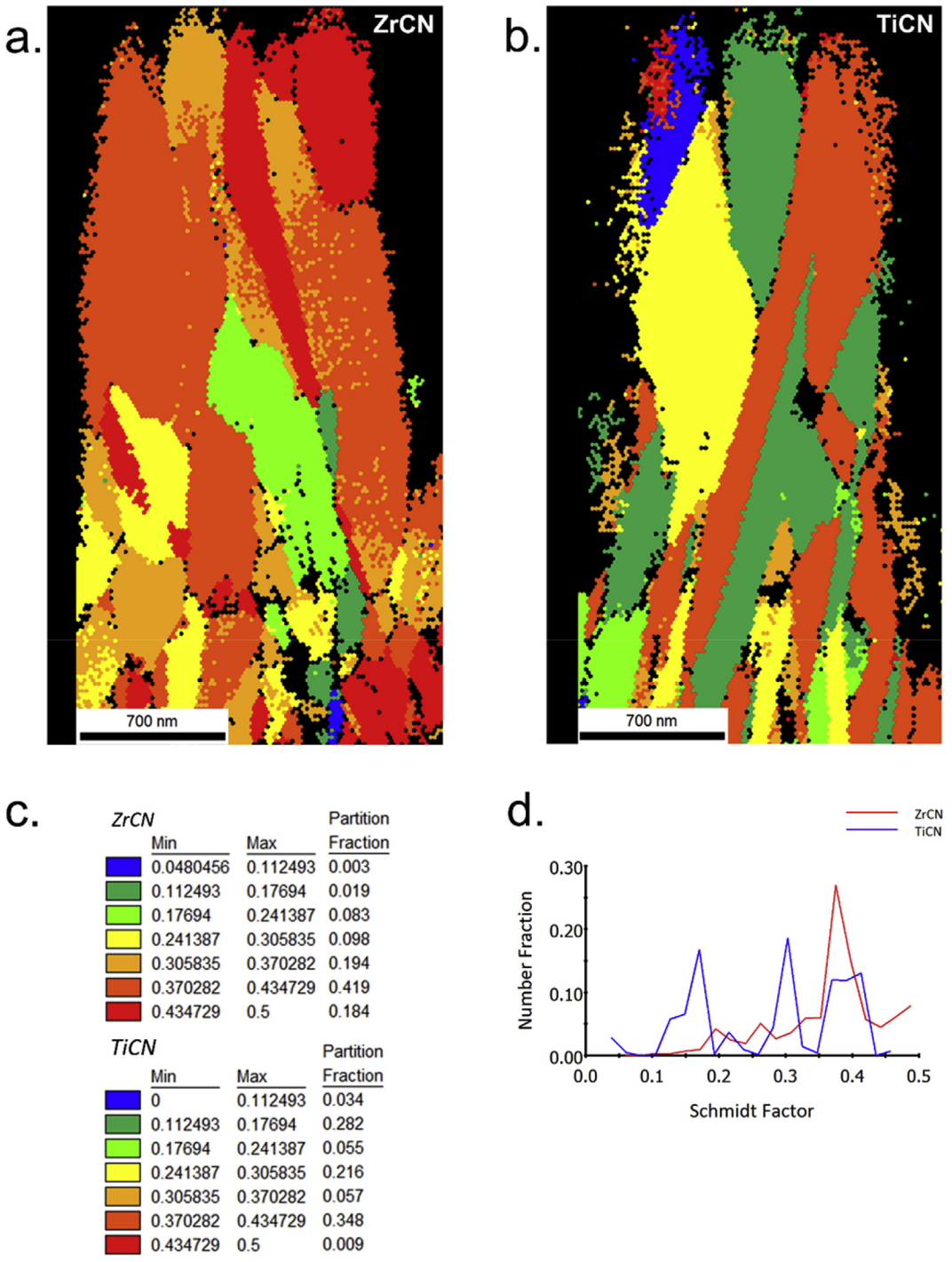

Fig. 13. Schmid factor map for Zr(C,N) (a) and Ti(C,N) (b) (Map legend in (c)). (d) Schmid factor distribution in Zr(C,N) and Ti(C,N).

during rolling. The latter could be considered as compression in the direction of rolling plane normal [72] which have similarities to our micro-compression test and will induce similar effects.

Calculation of Geometrically Necessary Dislocation (GND) from the misorientation measurements for Zr(C,N) is not precise because of the finer grain size and more importantly to the poor indexing at the grain boundaries.

For the case of Ti(C,N) no gradient is noticed and rather higher misorientations are located at the grain boundaries. As a result, unlike the Zr(C,N) which is deforming as a single structure, Ti(C,N) behaves as discrete arrays of grains sliding along each other and deforming independently. This confirms the earlier discussions for the deformation mechanism of Ti(C,N).

Summarizing, plastic deformation in ceramics at high temperature is a known fact, and since the 50s and over the past, many studies focused on high temperature plasticity for B1-type structure materials. However, dislocation motion and plasticity at room temperature is rather a recent topic. Kiani et al. [27] proved (using in-situ TEM compression tests) that ZrC monocrystals (which are very similar to Zr(C,N): same B1 lattice, comparable mechanical

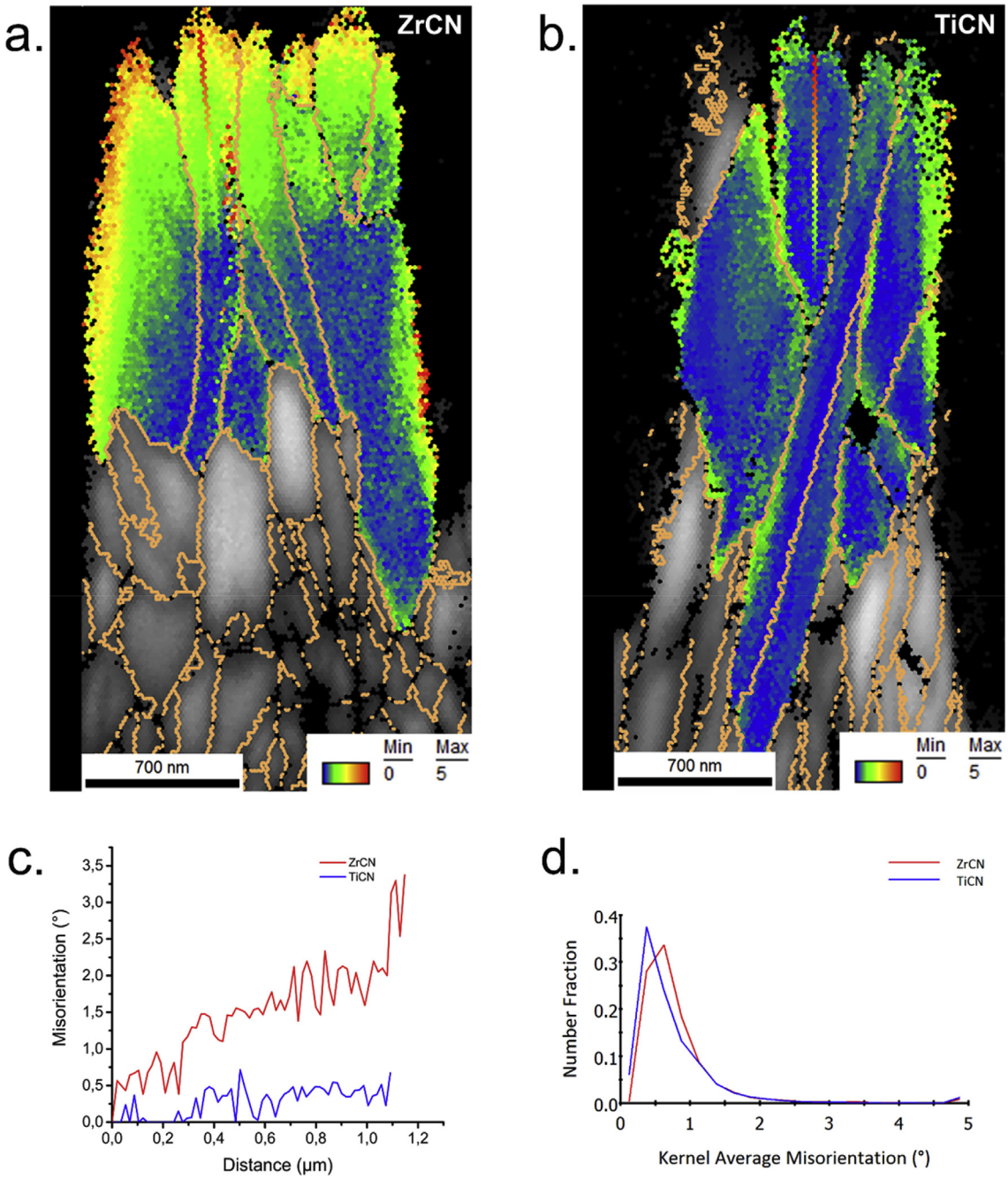

Fig. 14. Misorientation analysis with respect to a reference point for (a) Zr(C,N) (b) Ti(C,N). (c) Misorientation profile according to the drawn line in (a) and (b). (d) Kernel Average Misorientation (KAM) of Zr(C,N) vs Ti(C,N) calculated across the entire pillar.

properties) underwent a plastic deformation at room temperature. They also mentioned that carefully prepared polycrystalline transition metal carbide samples may also undergo plastic deformation at low temperatures upon the fact that multiple slip systems are active at room temperature [27]. The brittleness of the pillar is related mainly to the polycrystallinity of the pillar and multi-interfaces (due to the micron/sub-micron grain size) that exerts and limits dislocation motion [3]. In literature this phenomenon is introduced as the "microstructural constraint" (coating microstructure here) which is in addition to the "dimensional constraint" (pillar size in our case) that monitor together the dislocation mechanics and hence deformation mechanisms [73–75].

For the brittle failure, the bulk fragile properties take over as a general yielding at the end of the experiment test, which eclipses the local micro-phenomenon occurring at the grain scale. Indeed, the fracture probability of brittle materials decreases for smaller sizes [74] as the miniaturization of the dimension reduces the density of critical defects that causes brittle facture in ceramics. Hence, as the experiment progresses and the probability of a brittle fracture decreases, the internal mechanisms in the grains will take place and plastic deformation can be noticed. Besides, and for an analogy, compression test performed on even bulky (couple of millimeters sized) brittle materials showed that there is a critical size where the deformation switches from brittle to ductile [76]. In

other words, having an extended and lasting plastic deformation perceivable in our experiments depends on three things: the intrinsic factors (orientation and grain size), the type and density of grain boundaries, and finally the size of the tested sample.

The strong brittleness of Ti(C,N) is mainly attributed to low cohesive strength at the grain boundaries as demonstrated before. Nevertheless, the question about the absence or existence of plasticity within single Ti(C,N) crystals at room temperature cannot be addressed in this investigation. In-situ TEM compression of single crystals would be an effective technique to approach this question. Still, we suggest that the absence or limited dislocation mobility is more intrinsically related. On one side, if we compare the carbides variants (which are comparable to their carbonitrides counterpart), we find that TiC has only one active slip system $\{110\}\ 1\bar{1}0$ [14] at low temperatures in contrast to ZrC which has two active slip systems active at room temperature $\{001\}\ 110$ and $\{1\bar{1}0\}\ 110$ [27]. On the other side, mechanical properties of TMCN are intrinsically related to the electronic structure formed by the ternary compound (Transition Metal, Carbon and Nitrogen), an assumption which was supported earlier by Bilyk [4]. The nature and relative strengths of metal-metal and metal-carbon/nitrogen bonds change with the valence electron concentration (VEC) in the lattice [19] which makes for example plastic deformation pathways, ductility and hardness vary from TiC to ZrC [27]. Jhi et al. have explained these complex electronic interactions for TiC_xN_{1-x} when nitrogen is replacing carbon in the interstitials sites. They established an evolution of the shear modulus C_{44} with VEC for TiCxN1-x ($0 \leq x \leq 1$), and found that maximum hardness is obtained for VEC = 8.4. Besides, they stated that C_{44} is a good parameter to quantify the resistance of plastic deformation and finally, expected that the same results will be valid also for other transition metal alloys [19]. Later, Ivashchenko et al. have obtained similar results and explanations for TiC_xN_{1-x} [21] and more interestingly for ZrC_xN_{1-x} as well [22]. Thus, as the same explanation of hardness dependence on the nature of bonding is valid for Ti(C,N) and Zr(C,N), and as C_{44} shear modulus is a good parameter to quantify the resistance of plastic deformation for transition-metal alloys [19], then if we compare the corresponding C_{44} values of each type of coating, we can have a direct idea about the ease of plastic deformation in each case. In doing so, the calculated values are $C_{44}(TiC_{0.5}N_{0.5}) = 188$ GPa [21], $C_{44}(TiC_{0.5}N_{0.5}) = 185$ GPa [23] and $C_{44}(ZrC_{0.5}N_{0.5}) = 158$ GPa [22], and we can see clearly that it is higher for the former. Finally, this means that the brittleness of Ti(C,N) is not only related to low cohesive strength between grains, but also to limited dislocation activation at room temperature.

4. Conclusions

Throughout different techniques and investigations, the deformation behavior and micro-mechanical properties at room temperature of Ti(C,N) and Zr(C,N) CVD coatings were evaluated. Both Ti(C,N) and Zr(C,N) exhibited high yield strength of 14 GPa. Results revealed that Ti(C,N) undergoes a pure intergranular crack propagation and grain decohesion. Zr(C,N), in addition to its high strength and other outstanding properties, has attested for unexpected plastic deformation at room temperature and formation of strain gradients, as revealed by EBSD analysis. The brittle behavior of Ti(C,N) is dominated by low cohesive strength along the grain boundaries and reduced dislocation activation at room temperature. Taking into consideration that macroscopic deformation is scaled even on the mesoscale [54], the results presented in this work may explain the enhanced performance of Zr(C,N) under cycling thermo-mechanical loads by the combination of high hardness, better cohesive strength and its intrinsic plasticity compared to Ti(C,N).

Acknowledgements

The authors acknowledge Jeanette Persson (Sandvik Coromant R&D) for producing the CVD coatings, André Tengstrand (Sandvik Coromant R&D) for writing the ANSYS code of FEM analysis, Sebastian Slawik and Sebastián Suárez (Saarland University) for the discussions. The European Commission is acknowledged for funding through the projects: Erasmus Mundus Doctoral Programme DocMASE; RISE Project CREATe-Network (GA N° 644013) and EFRE project AME-Lab (European Regional Development Fund C/4-EFRE-13/2009/Br). Part of this paper was presented at 19th Plansee Seminar 2017, Reutte, Austria.

References

[1] C. Mitterer, PVD and CVD hard coatings, in: V.K. Sarin, L. Llanes, D. Mari (Eds.), Compr. Hard Mater. - Vol. 2 Ceram, Elsevier, Amsterdam, 2014, pp. 449–468.
[2] J. Garcia, R. Pitonak, The role of cemented carbide functionally graded outer-layers on the wear performance of coated cutting tools, Int. J. Refract. Metals Hard Mater. 36 (2013) 52–59, https://doi.org/10.1016/j.ijrmhm.2011.12.007.
[3] Y.X. Wang, S. Zhang, Toward hard yet tough ceramic coatings, Surf. Coating. Technol. 258 (2014) 1–16, https://doi.org/10.1016/j.surfcoat.2014.07.007.
[4] I.I. Bilyk, Potentialities of carbonitrides as the hard constituent of sintered hard alloys, Powder Metall. Mater. Parts Coat 11 (1972) 466–470, https://doi.org/10.1007/BF00797922.
[5] W. Lengauer, S. Binder, K. Aigner, P. Ettmayer, A. Guillou, J. Debuigne, G. Groboth, Solid state properties of group IVb carbonitrides, J. Alloy. Comp. 217 (1995) 137–147.
[6] Q. Yang, W. Lengauer, T. Koch, M. Scheerer, I. Smid, Hardness and elastic properties of Ti (C x N 1- x), Zr (C x N 1- x) and Hf (C x N 1- x), J. Alloy. Comp. 309 (2000) L5–L9.
[7] J. Garcia, M.F. Moreno, J. Östby, J. Persson, H.C. Pinto, Design of coated cemented carbides with improved comb crack resistance, in: Proc. 19th Plansee Semin., Reutte, Austria, 2017.
[8] W.G. Fahrenholtz, G.E. Hilmas, Ultra-high temperature ceramics: materials for extreme environments, Scr. Mater. 129 (2017) 94–99, https://doi.org/10.1016/j.scriptamat.2016.10.018.
[9] W.S. Williams, Influence of temperature, strain rate, surface condition, and composition on the plasticity of transition-metal carbide crystals, J. Appl. Phys. 35 (1964) 1329–1338, https://doi.org/10.1063/1.1713614.
[10] G.E. Hollox, R.E. Smallman, Plastic behavior of titanium carbide, J. Appl. Phys. 37 (1966) 818–823, https://doi.org/10.1063/1.1708264.
[11] D.W. Lee, J.S. Haggerty, Plasticity and creep in single crystals of zirconium carbide, J. Am. Ceram. Soc. 52 (1969) 641–647.
[12] I.V. Gridneva, Y.V. Mil'man, G.A. Rymashevskii, V.I. Trefilov, S.I. Chugunova, Effect of temperature on the strength characteristics of zirconium carbide, Sov. Powder Metall. Met. Ceram. 15 (1976) 638–645, https://doi.org/10.1007/BF01159455.
[13] R. Darolia, T.F. Archbold, Plastic deformation of polycrystalline zirconium carbide, J. Mater. Sci. 11 (1976) 283–290.
[14] D.K. Chatterjee, M.G. Mendiratta, H.A. Lipsitt, Deformation behaviour of single crystals of titanium carbide, J. Mater. Sci. 14 (1979) 2151–2156.
[15] E. Breval, Microplasticity at room temperature of single-crystal titanium carbide with different stoichiometry, J. Mater. Sci. 16 (1981) 2781–2788.
[16] G. Das, K.S. Mazdiyasni, H.A. Lipsitt, Mechanical properties of polycrystalline TiC, J. Am. Ceram. Soc. 65 (1982) 104–110.
[17] A.P. Katz, H.A. Lipsitt, T. Mah, M.G. Mendiratta, Mechanical behaviour of polycrystalline TiC, J. Mater. Sci. 18 (1983) 1983–1992.
[18] V.M. Sura, D.L. Kohlstedt, State-variable analysis of inelastic deformation of TiC single crystals, J. Am. Ceram. Soc. 70 (1987) 315–320.
[19] S.-H. Jhi, J. Ihm, S.G. Louie, M.L. Cohen, Electronic mechanism of hardness enhancement in transition-metal carbonitrides, Nature 399 (1999) 132–134, https://doi.org/10.1038/20148.
[20] A. Zaoui, B. Bouhafs, P. Ruterana, First-principles calculations on the electronic structure of TiCxN1−x, ZrxNb1−xC and HfCxN1−x alloys, Mater. Chem. Phys. 91 (2005) 108–115, https://doi.org/10.1016/j.matchemphys.2004.10.056.
[21] V.I. Ivashchenko, P.E.A. Turchi, L.A. Ivashchenko, P.L. Skrynskii, Electronic origin of elastic properties of titanium carbonitride alloys, Metall. Mater. Trans. 37 (2006) 3391–3396, https://doi.org/10.1007/s11661-006-1031-9.
[22] V.I. Ivashchenko, P.E.A. Turchi, V.I. Shevchenko, First-principles study of elastic and stability properties of ZrC–ZrN and ZrC–TiC alloys, J. Phys. Condens. Matter 21 (2009), 395503, https://doi.org/10.1088/0953-8984/21/39/395503.
[23] W. Feng, S. Cui, H. Hu, G. Zhang, Z. Lv, Electronic structure and elastic constants of TiCxN1−x, ZrxNb1−xC and HfCxN1−x alloys: a first-principles study, Phys. B Condens. Matter 406 (2011) 3631–3635, https://doi.org/10.1016/j.physb.2011.06.058.
[24] R.F. Zhang, S.H. Sheng, S. Veprek, Origin of different plastic resistance of transition metal nitrides and carbides: stiffer yet softer, Scr. Mater. 68 (2013) 913–916, https://doi.org/10.1016/j.scriptamat.2013.01.040.
[25] S.K. Yadav, R. Ramprasad, A. Misra, X.-Y. Liu, Core structure and Peierls stress

of edge and screw dislocations in TiN: a density functional theory study, Acta Mater. 74 (2014) 268–277, https://doi.org/10.1016/j.actamat.2014.04.047.
[26] V. Krasnenko, M.G. Brik, First-principles calculations of the structural, elastic and electronic properties of MNxC1−x (M = Ti, Zr, Hf; 0 ≤ x ≤ 1) carbonitrides at ambient and elevated hydrostatic pressure, Solid State Sci. 28 (2014) 1–8, https://doi.org/10.1016/j.solidstatesciences.2013.11.012.
[27] S. Kiani, C. Ratsch, A.M. Minor, S. Kodambaka, J.-M. Yang, Orientation- and size-dependent room-temperature plasticity in ZrC crystals, Philos. Mag. A 95 (2015) 985–997, https://doi.org/10.1080/14786435.2015.1012568.
[28] T. Li, T. Liu, L. Zhang, T. Fu, H. Wei, First-principles investigation on slip systems and twinnability of TiC, Comput. Mater. Sci. 126 (2017) 103–107, https://doi.org/10.1016/j.commatsci.2016.09.028.
[29] J. Kim, Y.J. Suh, Temperature- and pressure-dependent elastic properties, thermal expansion ratios, and minimum thermal conductivities of ZrC, ZrN, and Zr(C 0.5 N 0.5), Ceram. Int. 43 (2017) 12968–12974, https://doi.org/10.1016/j.ceramint.2017.06.195.
[30] G. Dehm, H.P. Wörgötter, S. Cazottes, J.M. Purswani, D. Gall, C. Mitterer, D. Kiener, Can micro-compression testing provide stress–strain data for thin films? Thin Solid Films 518 (2009) 1517–1521, https://doi.org/10.1016/j.tsf.2009.09.070.
[31] T.-H. Fang, S.-R. Jian, D.-S. Chuu, Nanomechanical properties of TiC, TiN and TiCN thin films using scanning probe microscopy and nanoindentation, Appl. Surf. Sci. 228 (2004) 365–372, https://doi.org/10.1016/j.apsusc.2004.01.053.
[32] S. Bhowmick, R. Bhide, M. Hoffman, V. Jayaram, S.K. Biswas, Fracture mode transitions during indentation of columnar TiN coatings on metal, Philos. Mag. A 85 (2005) 2927–2945, https://doi.org/10.1080/14786430500155213.
[33] M.T. Tilbrook, D.J. Paton, Z. Xie, M. Hoffman, Microstructural effects on indentation failure mechanisms in TiN coatings: finite element simulations, Acta Mater. 55 (2007) 2489–2501, https://doi.org/10.1016/j.actamat.2006.11.043.
[34] Z.H. Xie, M. Hoffman, P. Munroe, A. Bendavid, P.J. Martin, Deformation mechanisms of TiN multilayer coatings alternated by ductile or stiff interlayers, Acta Mater. 56 (2008) 852–861, https://doi.org/10.1016/j.actamat.2007.10.047.
[35] Y. Sun, C. Lu, H. Yu, A. Kiet Tieu, L. Su, Y. Zhao, H. Zhu, C. Kong, Nanomechanical properties of TiCN and TiCN/Ti coatings on Ti prepared by filtered arc deposition, Mater. Sci. Eng. A 625 (2015) 56–64, https://doi.org/10.1016/j.msea.2014.11.093.
[36] A. Zeilinger, J. Todt, C. Krywka, M. Müller, W. Ecker, B. Sartory, M. Meindlhumer, M. Stefenelli, R. Daniel, C. Mitterer, J. Keckes, In-situ observation of cross-sectional microstructural changes and stress distributions in fracturing TiN thin film during nanoindentation, Sci. Rep. 6 (2016), https://doi.org/10.1038/srep22670.
[37] R. Warren, Measurement of the fracture properties of brittle solids by Hertzian indentation, Acta Metall. 26 (1978) 1759–1769.
[38] H. Pelletier, J. Krier, A. Cornet, P. Mille, Limits of using bilinear stress–strain curve for finite element modeling of nanoindentation response on bulk materials, Thin Solid Films 379 (2000) 147–155.
[39] J.J. Gilman, Chemistry and Physics of Mechanical Hardness, Wiley, Hoboken, N.J, 2009.
[40] D. Kiener, C. Motz, G. Dehm, Micro-compression testing: a critical discussion of experimental constraints, Mater. Sci. Eng. A 505 (2009) 79–87, https://doi.org/10.1016/j.msea.2009.01.005.
[41] H. Fei, A. Abraham, N. Chawla, H. Jiang, Evaluation of micro-pillar compression tests for accurate determination of elastic-plastic constitutive relations, J. Appl. Mech. 79 (2012), 061011.
[42] S. Korte, J.S. Barnard, R.J. Stearn, W.J. Clegg, Deformation of silicon – insights from microcompression testing at 25–500°C, Int. J. Plast. 27 (2011) 1853–1866, https://doi.org/10.1016/j.ijplas.2011.05.009.
[43] N. Kheradmand, H. Vehoff, A. Barnoush, An insight into the role of the grain boundary in plastic deformation by means of a bicrystalline pillar compression test and atomistic simulation, Acta Mater. 61 (2013) 7454–7465, https://doi.org/10.1016/j.actamat.2013.08.056.
[44] S. Korte-Kerzel, Microcompression of brittle and anisotropic crystals: recent advances and current challenges in studying plasticity in hard materials, MRS Commun. 7 (2017) 109–120, https://doi.org/10.1557/mrc.2017.15.
[45] Y. Zou, H. Ma, R. Spolenak, Ultrastrong ductile and stable high-entropy alloys at small scales, Nat. Commun. 6 (2015) 7748, https://doi.org/10.1038/ncomms8748.
[46] J.M. Wheeler, R. Raghavan, V. Chawla, M. Morstein, J. Michler, Deformation of hard coatings at elevated temperatures, Surf. Coating. Technol. 254 (2014) 382–387, https://doi.org/10.1016/j.surfcoat.2014.06.048.
[47] S. Liu, R. Raghavan, X.T. Zeng, J. Michler, W.J. Clegg, Compressive deformation and failure of CrAlN/Si3N4 nanocomposite coatings, Appl. Phys. Lett. 104 (2014), 081919.
[48] S. Liu, J.M. Wheeler, J. Michler, X.T. Zeng, W.J. Clegg, Plastic flow at the theoretical yield stress in ceramic films, Scr. Mater. 117 (2016) 24–27, https://doi.org/10.1016/j.scriptamat.2016.02.008.
[49] M. Schlögl, C. Kirchlechner, J. Paulitsch, J. Keckes, P.H. Mayrhofer, Effects of structure and interfaces on fracture toughness of CrN/AlN multilayer coatings, Scr. Mater. 68 (2013) 917–920, https://doi.org/10.1016/j.scriptamat.2013.01.039.
[50] Y. Mu, X. Zhang, J.W. Hutchinson, W.J. Meng, Measuring critical stress for shear failure of interfacial regions in coating/interlayer/substrate systems through a micro-pillar testing protocol, J. Mater. Res. 32 (2017) 1421–1431, https://doi.org/10.1557/jmr.2016.516.
[51] H. Zhang, B.E. Schuster, Q. Wei, K.T. Ramesh, The design of accurate micro-compression experiments, Scr. Mater. 54 (2006) 181–186, https://doi.org/10.1016/j.scriptamat.2005.06.043.
[52] D.P. Field, K.R. Magid, I.N. Mastorakos, J.N. Florando, D.H. Lassila, J.W. Morris, Mesoscale strain measurement in deformed crystals: a comparison of X-ray microdiffraction with electron backscatter diffraction, Philos. Mag. A 90 (2010) 1451–1464, https://doi.org/10.1080/14786430903397297.
[53] J.-J. Fundenberger, A. Morawiec, E. Bouzy, J.S. Lecomte, Polycrystal orientation maps from TEM, Ultramicroscopy 96 (2003) 127–137, https://doi.org/10.1016/S0304-3991(02)00435-7.
[54] N.P. Gurao, S. Suwas, Generalized scaling of misorientation angle distributions at meso-scale in deformed materials, Sci. Rep. 4 (2015), https://doi.org/10.1038/srep05641.
[55] T. Csanádi, P. Szommer, N.Q. Chinh, S. Grasso, J. Dusza, M. Reece, Plasticity in ZrB 2 micropillars induced by anomalous slip activation, J. Eur. Ceram. Soc. 36 (2016) 389–394, https://doi.org/10.1016/j.jeurceramsoc.2015.10.035.
[56] J.M. Wheeler, C. Niederberger, C. Tessarek, S. Christiansen, J. Michler, Extraction of plasticity parameters of GaN with high temperature, in situ micro-compression, Int. J. Plast. 40 (2013) 140–151, https://doi.org/10.1016/j.ijplas.2012.08.001.
[57] T. Csanádi, M. Bľanda, A. Duszová, N.Q. Chinh, P. Szommer, J. Dusza, Deformation characteristics of WC micropillars, J. Eur. Ceram. Soc. 34 (2014) 4099–4103, https://doi.org/10.1016/j.jeurceramsoc.2014.05.045.
[58] J.M. Tarragó, J.J. Roa, E. Jiménez-Piqué, E. Keown, J. Fair, L. Llanes, Mechanical deformation of WC–Co composite micropillars under uniaxial compression, Int. J. Refract. Metals Hard Mater. 54 (2016) 70–74, https://doi.org/10.1016/j.ijrmhm.2015.07.015.
[59] J.P. Best, J. Wehrs, X. Maeder, J. Zechner, J.M. Wheeler, T. Schär, M. Morstein, J. Michler, Reversible, high temperature softening of plasma-nitrided hot-working steel studied using in situ micro-pillar compression, Mater. Sci. Eng. A 680 (2017) 433–436, https://doi.org/10.1016/j.msea.2016.11.003.
[60] O.N. Senkov, G.B. Wilks, J.M. Scott, D.B. Miracle, Mechanical properties of Nb25Mo25Ta25W25 and V20Nb20Mo20Ta20W20 refractory high entropy alloys, Intermetallics 19 (2011) 698–706, https://doi.org/10.1016/j.intermet.2011.01.004.
[61] Y. Zou, S. Maiti, W. Steurer, R. Spolenak, Size-dependent plasticity in an Nb25Mo25Ta25W25 refractory high-entropy alloy, Acta Mater. 65 (2014) 85–97, https://doi.org/10.1016/j.actamat.2013.11.049.
[62] S.I. Wright, M.M. Nowell, D.P. Field, A review of strain analysis using electron backscatter diffraction, Microsc. Microanal. 17 (2011) 316–329, https://doi.org/10.1017/S1431927611000055.
[63] D.A. Hughes, Q. Liu, D.C. Chrzan, N. Hansen, Scaling of microstructural parameters: misorientations of deformation induced boundaries, Acta Mater. 45 (1997) 105–112.
[64] D.A. Hughes, D.C. Chrzan, Q. Liu, N. Hansen, Scaling of misorientation angle distributions, Phys. Rev. Lett. 81 (1998) 4664.
[65] Q. Liu, N. Hansen, Geometrically necessary boundaries and incidental dislocation boundaries formed during cold deformation, Scr. Metall. Mater 32 (1995) 1289–1295.
[66] A.M. Korsunsky, M. Sebastiani, E. Bemporad, Focused ion beam ring drilling for residual stress evaluation, Mater. Lett. 63 (2009) 1961–1963, https://doi.org/10.1016/j.matlet.2009.06.020.
[67] M. Sebastiani, C. Eberl, E. Bemporad, G.M. Pharr, Depth-resolved residual stress analysis of thin coatings by a new FIB–DIC method, Mater. Sci. Eng. A 528 (2011) 7901–7908, https://doi.org/10.1016/j.msea.2011.07.001.
[68] L. Clément, R. Pantel, L.F.T. Kwakman, J.L. Rouvière, Strain measurements by convergent-beam electron diffraction: the importance of stress relaxation in lamella preparations, Appl. Phys. Lett. 85 (2004) 651–653, https://doi.org/10.1063/1.1774275.
[69] N.P. Gurao, S. Suwas, Deformation behaviour at macro- and nano-length scales: the development of orientation gradients, Mater. Lett. 99 (2013) 81–85, https://doi.org/10.1016/j.matlet.2013.02.074.
[70] R.W. Harrison, W.E. Lee, Processing and properties of ZrC, ZrN and ZrCN ceramics: a review, Adv. Appl. Ceram 115 (2016) 294–307, https://doi.org/10.1179/1743676115Y.0000000061.
[71] L. Toth, Mechanical properties, in: Transit. Met. Carbides Nitrides, first ed., Academic Press, 1971, p. 279.
[72] R. Smallman, D. Green, The dependence of rolling texture on stacking fault energy, Acta Metall. 12 (1964) 145–154, https://doi.org/10.1016/0001-6160(64)90182-8.
[73] R.W. Armstrong, On size effects in polycrystal plasticity, J. Mech. Phys. Solids 9 (1961) 196–199, https://doi.org/10.1016/0022-5096(61)90018-7.
[74] E. Arzt, Size effects in materials due to microstructural and dimensional constraints: a comparative review, Acta Mater. 46 (1998) 5611–5626.
[75] J.R. Greer, J.T.M. De Hosson, Plasticity in small-sized metallic systems: intrinsic versus extrinsic size effect, Prog. Mater. Sci. 56 (2011) 654–724, https://doi.org/10.1016/j.pmatsci.2011.01.005.
[76] K. Kendall, Complexities of compression failure, in: Proc. R. Soc. Lond. Math. Phys. Eng. Sci, The Royal Society, 1978, pp. 245–263.

7.2 Paper II

Atom Probe Tomography investigations on grain boundary segregation in polycrystalline Ti(C,N) and Zr(C,N) CVD coatings

I. El Azhari, J. Barrirero, J. García, F. Soldera, L. Llanes, F. Mücklich

Scripta Materialia. 162 (2019) 335–340

https://doi.org/10.1016/j.scriptamat.2018.11.041

Scripta Materialia 162 (2019) 335–340

Contents lists available at ScienceDirect

Scripta Materialia

journal homepage: www.elsevier.com/locate/scriptamat

Regular article

Atom Probe Tomography investigations on grain boundary segregation in polycrystalline Ti(C,N) and Zr(C,N) CVD coatings

Idriss El Azhari [a,b,c,*], Jenifer Barrirero [a,c], José García [d], Flavio Soldera [a,c], Luis Llanes [b], Frank Mücklich [a,c]

[a] Functional Materials, Department of Materials Science and Engineering, Saarland University, Campus D 3.3, D-66123 Saarbrücken, Germany
[b] Materials Science and Metallurgical Department (CIEFMA), Barcelona East School of Engineering (EEBE), Universitat Politècnica de Catalunya, 08019 Barcelona, Spain
[c] Material Engineering Center Saarland (MECS), D-66125 Saarbrücken, Germany
[d] Sandvik Coromant R&D, SE-126 80 Stockholm, Sweden

ARTICLE INFO

Article history:
Received 16 August 2018
Received in revised form 30 October 2018
Accepted 21 November 2018
Available online 29 November 2018

Keywords:
CVD polycrystalline coatings
Atom Probe Tomography
Grain boundary segregation
Chlorine
Cobalt

ABSTRACT

Atom Probe Tomography (APT) was used to obtain a direct evidence of chlor segregation and cobalt diffusion at the grain boundaries (GBs) of polycrystalline coatings deposited by moderate temperature chemical vapor deposition (MT-CVD) on a WC-Co cemented carbide substrate. Reasons behind segregations are discussed, and its effects are correlated to the micromechanical properties of Ti(C,N) and Zr(C,N). It is concluded that chlorine segregation is a relevant factor for explaining the low cohesive strength at the GBs of Ti(C,N) leading to intergranular failure during micro-compression testing, while its absence in Zr(C,N) along with Co diffusion contribute to grain boundary strengthening.

Characterization of microstructure in terms of orientation, texture and interfaces is fundamental for understanding the physical properties and behavior of polycrystalline materials. Interfaces or grain boundaries (GBs) play a decisive role in controlling the overall mechanical properties of fine-grained materials [1]. Classical example is the empirical Hall-Petch law, which predicts the evolution of hardness as a function of grain size. Nowadays, concepts like GB engineering and even GB segregation engineering are emerging due to the observations that solutes or impurities tune greatly the structure, phase state and atomic bonding [2]. Regarding mechanical properties, segregation at the interfaces might reduce or enhance cohesion and bonding strength at GBs [2]. Within this context, the present study is a sequel to a recently published work [3], in which micromechanical properties of MT-CVD Ti(C,N) and Zr(C,N) coatings were studied by means of micropillar compression. A relevant finding of such work was that the brittle behavior of Ti(C,N) is dominated by low cohesive strength along the grain boundaries and pure columnar crack propagation, while Zr(C,N) coatings attested of a better cohesive strength and inter/transgranular failure. One plausible cause for such distinct behavior could be segregation of impurities at interfaces. For low temperature CVD processes, chlorine contamination is a concern [4–21], which stems from the widely used metal chloride as a precursor in CVD reactions (e.g. $TiCl_4$ is the most widely used inorganic precursor employed in the CVD of titanium-containing materials (TiN, TiC, TiO_2, Ti(C,N)) [22]). However, most authors have reported that chlorine is incorporated into the lattice [4,5,7,9–11,13,19,23], rather than to interfaces and no direct evidence has been provided. Therefore, APT is performed on Ti(C,N) and Zr(C,N) coatings to explore if segregation is occurring at GBs and discuss which effect this segregation could have on the mechanical properties of these coatings.

$Ti(C_{0.5},N_{0.5})$ and $Zr(C_{0.5},N_{0.5})$ were deposited by MT-CVD process on a WC-6wt%Co substrate at a constant temperature of 885 and 930 °C, respectively, in a hot wall reactor using $TiCl_4$, CH_3CN and H_2 as gas precursors. The thickness of the coating was 5 ± 0.2 μm. A TiN starting interlayer of 0.3 ± 0.02 μm was previously deposited to promote the nucleation of the carbonitride coating and to improve adhesion to the substrate. Prior to the preparation of APT samples, an embedded cross-section of the deposited coatings was mirror polished with 0.02 μm alumina suspension as the final step. Afterwards, APT sample preparation was conducted in a dual-beam focused ion beam/scanning electron microscopy workstation (FIB/SEM) Helios NanoLab 600™ (FEI). Specimens were extracted from a cross section view at the middle distance between the substrate and the top surface of the coating by the lift-out technique described in [24]. An electron beam induced Pt-capping layer was first deposited to protect the sample from gallium (Ga) implantation. After the lift-out and thinning of the samples, a low energy milling at 2 kV was performed to minimize Ga induced damage. Between 6 and 8 specimens were prepared and measured from each lift-out. Laser Pulsed APT was performed in a LEAP™ 3000XR (CAMECA)

* Corresponding author at: Functional Materials, Department of Materials Science and Engineering, Saarland University, Campus D 3.3, D-66123 Saarbrücken, Germany.
E-mail address: idriss.elazhari@uni-saarland.de (I. El Azhari).

https://doi.org/10.1016/j.scriptamat.2018.11.041
1359-6462/

at a repetition rate of 200 kHz, a specimen temperature of about 60 K, a pressure lower than 1×10^{-10} Torr (1.33×10^{-8} Pa) and a laser pulse energy of 0.5 nJ. The evaporation rate of the specimen was 5 atoms per 1000 pulses. Datasets were reconstructed and analyzed with the IVAS™3.6.14 software (CAMECA) based on the voltage curves. The evaporation field was estimated to be 40 V/nm for the Ti(C,N) specimens and 45 V/nm for Zr(C,N). This estimation was done with the help of the Kingham curves for Ti and Zr [25]. All specimens were reconstructed with an image compression factor of 1.65 and a k-factor of 3.3 [26].

In total, five APT datasets of the Ti(C,N) coating and four datasets of the Zr(C,N) coating were analyzed. Two datasets for each coating presented GBs, while the rest of the reconstructions showed homogeneous in-grain composition. All compositions presented in Table 1 were obtained after elemental decomposition analysis and background subtraction in IVAS software. Due to the high amount of molecular ions and multiple events during detection of carbides, the C content in the Ti(C,N) coating was corrected using two methods introduced in literature: ^{13}C-method [27] and 24 Da peak correction [28]. For the Zr(C,N) coating, no loss at the ^{12}C peak was observed and no correction at the 24 Da peak was necessary. Table 1 presents a weighted average of the in-grain composition of five APT specimens of Ti(C,N) and three specimens of Zr(C,N). The in-grain composition was calculated using the whole dataset for APT specimens with no GBs and in cubic regions of interest in specimens with GBs. The average compositions in the Co-rich and Cl-rich boundaries (Table 1) were measured inside 1 at.% Co and 1 at.% Cl isoconcentration surfaces for all specimens with GBs. The open source software Blender 2.76 with the open access plug-in AtomBlend were used for the images presented in this work.

Fig. 1 shows an APT reconstruction inside a Ti(C,N) grain of the polycrystalline CVD coatings. The dataset shows a homogenous distribution of Ti, C and N; thus, an absence of clustering between TiC and TiN compounds. This demonstrates the complete miscibility between the three elements in the lattice. Such result is consistent with first principles calculation of the formation energy of $Ti(C_x,N_{1-x})$ [29]. In addition, impurities like oxygen O, chlorine Cl and cobalt Co are present at very low concentration (<200 ppm especially for Cl and Co, further details are in Table 1). However, in Fig. 2 it is evidenced that segregation of Co and Cl takes place at the GBs in the polycrystalline Ti(C,N). Co and Cl show interlocked and demixed regions with an average concentration of around 2.2 at.% for each element (Table 1). Different perspectives of this co-segregation and demixing are presented in Fig. 2(b). Two concentration profiles crossing Co and Cl rich regions were calculated in cylindrical regions of interest and are presented in Fig. 2(c) and (d), respectively.

Similar to Ti(C,N), a homogeneous distribution of Zr, C and N was confirmed inside the grains of the Zr(C,N) coating. This is also in accordance with the first principle calculations of formation energy for $Zr(C_x, N_{1-x})$ [30]. Moreover, along with Ti, impurities of Cl and Co are detected with very low concentration.

The APT reconstruction of Zr(C,N) with GBs in Fig. 3 shows, in contrast to Ti(C,N), segregation of homogeneously distributed Co without Cl. Different perspectives of this homogeneous Co segregation are shown in Fig. 3(b), and concentration profiles crossing selected regions are displayed in Fig. 3(c) and (d). Table 1 summarizes the weighted average concentration in the grains and at the boundary for the analyzed specimens. The concentrations are consistent with the predicted $Tm_{0.5}$ ($C_{0.25}$,$N_{0.25}$) (Tm: Ti/Zr) that results from the use of acetonitrile (CH_3CN) as a CVD precursor and delivers constant C/N ratio [31]. The deviation of N content with respect to the expected stoichiometry can be related to the deposition conditions, presence of vacancies, as well as possible local compositional variations between the individual grains. Furthermore, a slight underestimation of N of 1–2 at.% cannot be excluded when using APT due to the high amount of multiple events during detection [32]. Existence of Ti impurities in Zr(C,N) can come either from the residual $TiCl_4$ (or sub-chloride) during prior TiN deposition or from dissolved Ti in the diffused Co. The latter assumption is discarded by considering that solubility of TiN in cobalt is very limited [33] and by the comparison of Ti compositions in the bulk and at the interfaces of Zr(C,N) (Table 1).

Chlorine contamination related to CVD processes, using metal chloride precursors, is well known and documented for Low Temperature (LT) CVD processes; like Plasma Assisted (PA) [4–13,23,34] and Low Pressure (LP) CVD [12,14–21]. However, its effects on MT-CVD process are underestimated or overlooked, given that chlorine content decreases considerably with higher temperatures and at MT-CVD temperature deposition range (700–950 °C) the Cl concentration is very low. As an example, it was reported for TiN deposited by LP-CVD that the chlorine content is decreasing from 7.2% at the deposition temperature of 450 °C down to 0.15% at 850 °C [20]. In this investigation, comparison between the Ti(C,N) and Zr(C,N) is key in understanding the segregation of chlorine and its resulting effect. This is possible since both coatings have similar B1 lattice structure and comparable physical properties [35,36], and share the same simplified CVD reaction deposition [37,38]:

$$T_mCl_4 + CH_3CN + 2_{1/2}H_2 \rightarrow T_mCN + CH_4 + 4HCl \quad (1)$$

where T_m is the transition metal Ti or Zr.

For Ti(C,N) PA-CVD, Kim et al. has shown that the chlorine content decreased largely with an increase of the temperature [6], and generally there is a consensus that the main parameter controlling the chlorine contamination in LT-CVD processes using metal chloride is the temperature [5,6,10,13–17,20,21,23,34]. Some authors even controlled the chlorine contamination by changing only the temperature, while keeping the other parameters constant [13,23,34]. This might be not only related to the effect of the thermal decomposition of the metal chloride, but also to the crucial role of the reductant H_2 (Eq. (1)) or hydrogen source in general. On the one hand, it was stated that without H_2 gas in the CVD chamber, the deposition in PA-CVD processes is not possible [4], and the thermal decomposition of the $TiCl_4$ to titanium subchlorides ($TiCl_3$, $TiCl_2$ and TiCl) is poor even at high temperatures (e.g. at ~1700 °C, decomposition of $TiCl_4$ does not exceed 10%) [22]. On the other hand, post-annealing treatment with hydrogen source (H_2 or NH_3) was proposed as a solution to reduce the chlorine contamination for TiN coating [17–19]. With the increase of temperature, HCl production is kinetically promoted as the reaction rate follows Arrhenius behavior [22]. As a result, active chlorine (which can be reabsorbed on interfaces of the growing film) is more desorbed and converted to highly stable HCl [22] which is the most stable form of chlorine [8]. Subsequently, the residual chlorine is cleaned from the system by improving formation of the stable HCl gas that will be evacuated afterwards.

Table 1
Atomic percentage for different areas in Ti(C,N) and Zr(C,N).

	Composition at.%	Ti	Zr	C	N	Co	O	Cl
Ti(C,N)	In the grain	51.55 ± 0.06	–	26.22 ± 0.05	22.00 ± 0.04	0.06 ± 0.01	0.16 ± 0.01	0.02 ± 0.01
	Co rich region at the boundary	48.59 ± 0.15	–	27.12 ± 0.13	21.40 ± 0.18	2.25 ± 0.06	0.16 ± 0.01	0.49 ± 0.03
	Cl rich region at the boundary	51.66 ± 0.43	–	24.46 ± 0.24	20.96 ± 0.20	0.39 ± 0.06	0.24 ± 0.01	2.28 ± 0.11
Zr(C,N)	In the grain	0.11 ± 0.01	49.74 ± 0.06	28.51 ± 0.04	21.60 ± 0.03	0.03 ± 0.01	–	0.01 ± 0.01
	Co rich region at the boundary	0.08 ± 0.01	49.09 ± 0.10	24.50 ± 0.06	23.55 ± 0.05	2.77 ± 0.03	–	0.01 ± 0.01

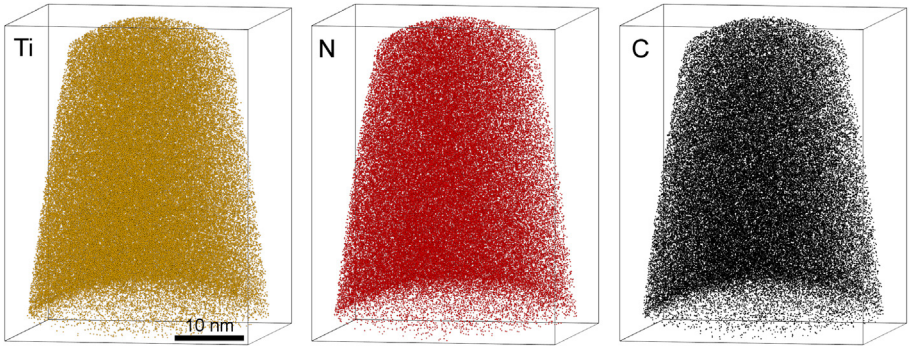

Fig. 1. Atomic maps inside a Ti(C,N) grain. Homogeneous distribution of Ti, N and C.

In this study, deposition of Zr(C,N) is conducted at 45 °C higher than Ti(C,N) since $ZrCl_4$ is more stable than $TiCl_4$ and requires higher activation energy to reach similar deposition rate as for the Ti(C,N). Therefore, it is suggested that the absence of chlorine segregation in the Zr(C,N) and its lower concentration inside the grain is due to higher temperature deposition, along with the lower metal chloride partial pressure [6], which is in this study two times lower for Zr(C,N) compared to Ti(C,N). All APT specimens obtained for this study showed consistent results with no Cl segregation at the GB of Zr(C,N). Despite the small number of analyzed GBs, it is considered that they are representative of the polycrystalline coating, since under the used parameters, the CVD deposition is uniform [39]. Therefore, the reactions (during deposition) and diffusion (during cooling step) that could lead to Cl segregation are considered rather homogeneous. Besides, the Zr(C,N) APT specimens show multiple triple junctions (Fig. 3). Triple junctions are high energy boundaries with a high number of vacancies and high diffusivity which would be the most energetically favorable sites for segregation to occur [40]. The absence of Cl segregation at these triple junctions is a strong evidence of the general absence of Cl at GBs in this coating.

Determining the chemical state or form of segregated chlorine at the GBs based on the APT is not a trivial question and beyond the capabilities of the technique. For TiN deposited through PA-CVD, it was proposed that the Cl is incorporated into the lattice structure forming a solid solution with Ti and N [4,5,7,9–11,13,19,23]. Stoiber et al. added that when chlorine exceeds the limit of solubility in the TiN lattice (3.2 at.%), it segregates afterwards at the GBs [23]; whereas Buiting et al. suggested that for LP-CVD TiN, chlorine is preferentially segregated at the GBs [15,16]. These conclusions were based on general correlations, e.g. the expansion of the lattice parameter with higher chlorine, decrease of N content with higher Cl contamination, relaxation of residual stresses, evolution of chlorine profiles content with change in grain size. However, in both cases no direct evidence was provided. In this

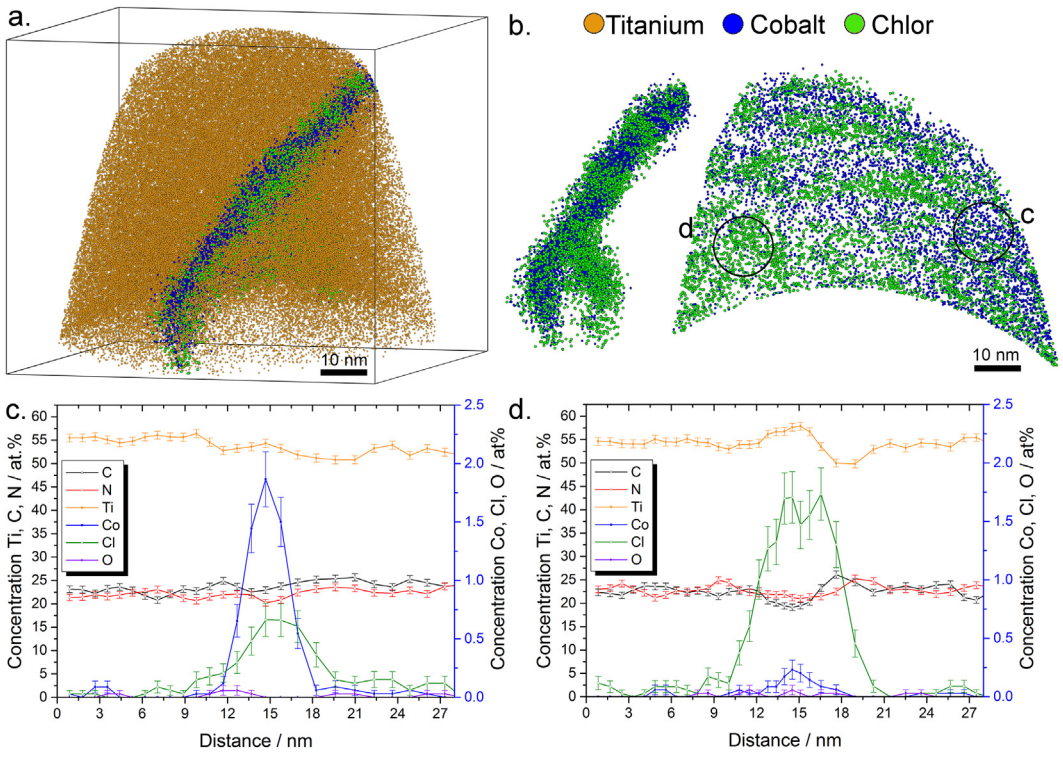

Fig. 2. (a) Atomic map of a GB in Ti(C,N) containing Co and Cl segregation. (b) Isolated Co and Cl segregations at the GB; two 90° rotated views are presented for clarity. Sections of cylinder c and d crossing Co rich and Cl rich are shown respectively. The segregation highlights the demixing of Co and Cl. (c) Concentration profile across a Co rich region at the boundary corresponding to cylinder c. (d) Concentration profile across a Cl rich region corresponding to cylinder d. These concentration profiles are calculated in cylindrical regions of interest with a direction perpendicular to the GBs. The sampling of the concentration profiles was adjusted to minimize statistical error using a fixed number of counts per sampling block.

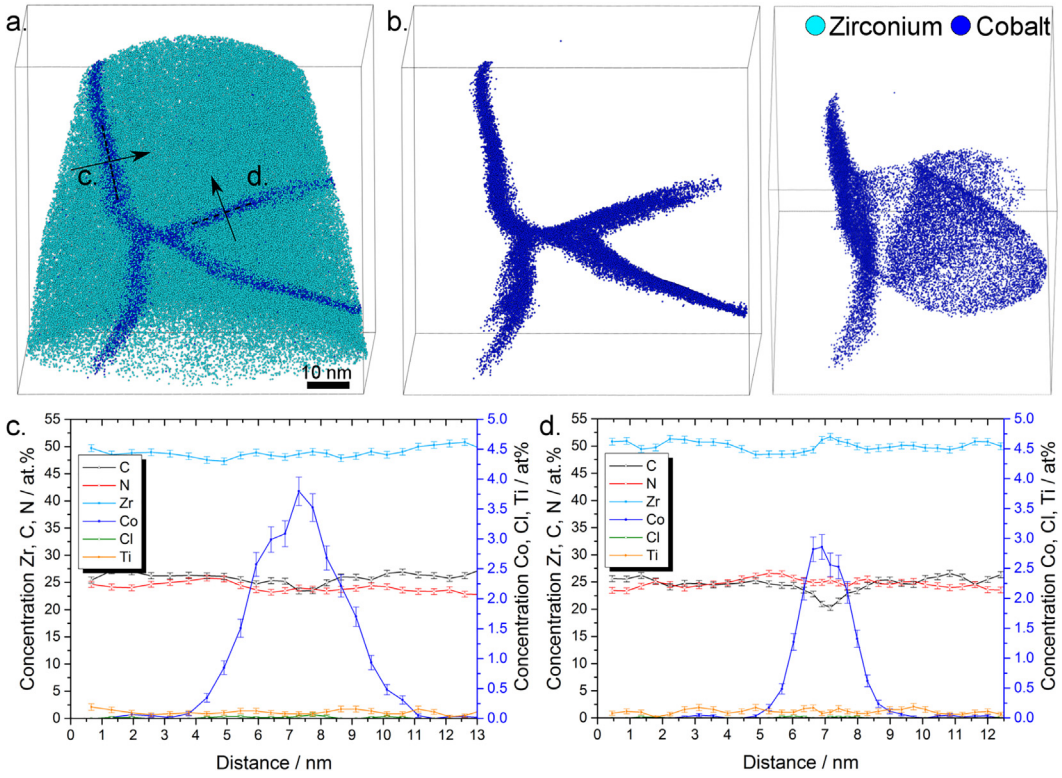

Fig. 3. (a) Atomic map of Co segregation at the GBs in Zr(C,N). (b) Isolated Co segregation at the GBs in two different perspectives for clarity. (c, d) Concentration profiles across the Co segregation at the GBs according to cylindrical regions of interests indicated by the arrows in panel (a).

study, Table 1 shows that there is nearly no solubility of Cl in Ti(C,N) (as the concentration is estimated about 200 ppm inside the grain) and the chlorine is rather segregated at the GBs up to 2.2 at.%. Additionally, Ti(C,N) has a finer grain size than Zr(C,N) [3] which is consistent with the role of chlorine in refinement of the microstructure [6,10,23]. Then, it is suggested that chlorine acts as an impurity, which is adsorbed on the crystal facets during film growth and segregates, yielding finally smaller grain sizes. Hence, chlorine can be considered as a structure forming factor during the film growth [23,41]. Additionally, concentration profile crossing chlorine rich region in Fig. 2(d) displays a slight drop in C and N content with an increase of Ti content and the average values in Table 1 reveal that titanium concentration is decreasing in the Co rich regions while it remains stable (or increases fractionally) in the Cl rich regions. This could be an indication that the chlorine (or active chlorine as mentioned earlier) may exist in the form of titanium subchlorides, which was already supported by previous works [8,14,16]. Additionally, for $Ti_{1-x}Al_xN$, it was also concluded that chlorine originates mainly from incomplete dissociation of the metal chloride $AlCl_3$ [8,12,21].

Comparison of the micromechanical properties for both coating from micro-compression tests is not an easy task [3], taking into account, beside their similarities, their differences in grain size, in the transition metal phase and microstructure. Nevertheless, the property that is contrasted in this study is the specific inter-columnar cracking for Ti(C,N) which can be caused either by the reduced dislocation activation at room temperature or lower cohesive strength at the GBs [3]. The APT investigations have provided support to the previous speculations about segregation of impurities as a potential cause of the GB brittleness for Ti(C,N), as given by its specific intergranular fracture during micro-compression tests (Fig. 4). However, Co segregates also in Zr(C,N) GBs which has better cohesive strength than Ti(C,N) and shows instead of a pure intercolumnar cracking rather a mixed trans/intergranular

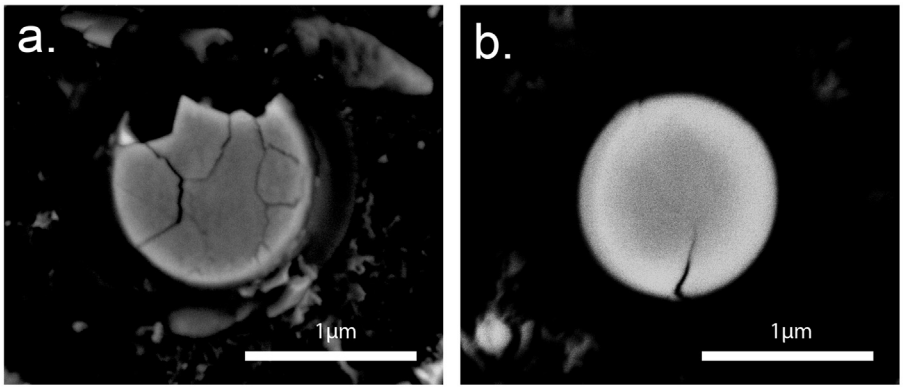

Fig. 4. Top view post-compression images of (a) Ti(C,N) and (b) Zr(C,N) micropillars. While Zr(C,N) shows indefinite crack propagation, Ti(C,N) fails at the GBs showing low cohesive strength leading to intercolumnar failure. (For more details refer to Ref. [3]).

crack propagation mode [3]. Then, what is the impact of both Cl and Co elements on the strength at the GBs?

Usually, segregation of chemical elements at GBs promotes embrittlement of the material. However, it was reported for particular cases that it can have a beneficial reverse effect of enhancing the ductility [42–45]. Accordingly, two approaches were established to understand this contradictory effect of impurities, either through the analysis of the effects of segregated elements on the electronic structure at the GB [46] or with calculation of the segregation energy [47]. Both methods require first principles calculations and analysis, which is out of the scope of the present study. Nevertheless, chlorine, with its intrinsic high electronegativity, would definitely have a dramatic negative effect on the interfacial cohesion and electronic structure between adjacent atoms at the GBs. The role of chlorine has been highlighted in the GB embrittlement of Ni-based superalloys [48] and sintered titanium dioxide (TiO_2) [49] which leads to intergranular fracture. For the LT-CVD titanium based coating, it is agreed on the deterioration of mechanical properties with the increase of chlorine content, i.e. decrease in hardness [5–12,23] and in adhesion to the substrate [6,8,10–12].

Diffusion of WC-Co substrate elements in the coating during CVD deposition has been already reported [50,51]. In this study, cobalt diffuses from the substrate to the coating crossing the TiN interlayer through the interfaces and segregates at GBs thereafter with concentrations of 2.77 at.% and 2.25 at.% for Zr(C,N) and Ti(C,N), respectively. Very low concentrations at the bulk have been resolved: 600 ppm and 300 ppm for Ti(C,N) and Zr(C,N), respectively. These results are aligned with earlier work of Akiyama et al. on a similar Ti(C,N) coating [51]. As for the absence of tungsten (W) in both coatings, it is related to the higher mobility of Co compared to W [51]. It might be expected that segregation of cobalt will have a negative effect on the mechanical properties especially at higher temperatures, where these coatings are expected to perform efficiently when low melting phases form at the interface, leading to the drop of high-temperature strength [52]. Still, it was reported that diffusion and segregation of elements (at the GBs) from the WC-Co substrate during the deposition enhances the adhesion to the substrate and wear resistance [50,51]. This may indicate that Co might have a strengthening effect on the interfaces, an assumption which is proved through first principles electron-structure calculations on the interface adhesion of Co/Ti(C,N) by Dudiy et al. [53]. The author explained the development of a strong Co-C(N) metal modified covalent bond at the interface which is even stronger than the bulk bonding between Ti-C(N) [53]. Considering the close physical properties between Ti(C,N) and Zr(C,N), similar effects for Zr(C,N) might be expected. Since both coatings have similar amount of Co segregating at the boundaries, it can be pointed out that one relevant factor contributing to the low cohesive strength and enhanced intergranular fracture of Ti(C,N), in comparison to Zr(C,N), is the segregation of chlorine at the GBs. Chlorine co-segregates alongside with cobalt and alters its homogeneous distribution at the boundaries (Fig. 2(b)).

Based on the combination of APT characterization and assessment of micromechanical response, the following conclusions can be summarized:

- Even at high deposition temperature of 885 °C for Ti(C,N) on a WC-Co substrate, chlorine segregates at GBs along with cobalt with demixing Cl and Co rich zones. Cl is suggested to stem from the titanium subchlorides, which adsorbs and segregates at the interfaces during crystal growth resulting in a finer microstructure.
- Zr(C,N) exhibited only Co segregation at the GBs which diffused from the substrate during CVD deposition. It is proposed that Co is enhancing the GB strength or at least not harmful toward it.
- Absence of Cl segregation in Zr(C,N) is attributed to the higher deposition temperature and lower metal chloride partial pressure.
- Chlorine segregation might be one of the factors contributing to the low cohesive strength at the GBs of Ti(C,N), which results in the specific intergranular fracture behavior evidenced under uniaxial compression of micropillars.

Acknowledgments

The authors thank Lucia Campo (Saarland University) for the help in APT experiments. Dr. Hisham Aboulfadl (Saarland University), Dr. Christoph Pauly (Saarland University) and Dr. Isabella Schramm (Ghent University) are thanked for the APT technical recommendation. Jeanette Persson and Linus von Fieandt (Sandvik Coromant) are kindly thanked for producing the CVD coatings. The Australian Centre for Microscopy and Microanalysis is acknowledged for providing AtomBlend plug-in. The European Commission is acknowledged for funding through the projects: Erasmus Mundus Doctoral Programme DocMASE, RISE Project CREATe-Network (GA No 644013) and EFRE project AME-Lab (European Regional Development Fund C/4-EFRE-13/2009/Br). The Atom Probe was financed by the DFG and the Federal State Government of Saarland (INST 256/298-1 FUGG). AB Sandvik Coromant is acknowledged for the partial financial support of the PhD thesis (I. El Azhari).

Appendix A. Supplementary data

Supplementary data to this article can be found online at https://doi.org/10.1016/j.scriptamat.2018.11.041.

References

[1] H. Gleiter, Prog. Mater. Sci. 33 (1989) 223–315.
[2] D. Raabe, M. Herbig, S. Sandlöbes, Y. Li, D. Tytko, M. Kuzmina, D. Ponge, P.-P. Choi, Curr. Opin. Solid State Mater. Sci. 18 (2014) 253–261.
[3] I. El Azhari, J. Garcia, M. Zamanzade, F. Soldera, C. Pauly, L. Llanes, F. Mücklich, Acta Mater. 149 (2018) 364–376.
[4] S. Li, W. Huang, H. Yang, Z. Wang, Plasma Chem. Plasma Process. 4 (1984) 147–161.
[5] T. Arai, H. Fujita, K. Oguri, Thin Solid Films 165 (1988) 139–148.
[6] S.B. Kim, S.K. Choi, S.S. Chun, K.H. Kim, J. Vac, Sci. Technol. Vac. Surf. Films 9 (1991) 2174–2179.
[7] K.-T. Rie, A. Gebauer, J. Woehle, Surf. Coat. Technol. 60 (1993) 385–388.
[8] K.H. Kim, S.H. Lee, Thin Solid Films 283 (1996) 165–170.
[9] K.-T. Rie, A. Gebauer, J. Wöhle, Surf. Coat. Technol. 86 (1996) 498–506.
[10] B. Arnold, I. Endler, Microchim. Acta 125 (1997) 83–87.
[11] K. Wetzig, I. Endler, Microchim. Acta 125 (1997) 121–125.
[12] S. Anderbouhr, V. Ghetta, E. Blanquet, C. Chabrol, F. Schuster, C. Bernard, R. Madar, Surf. Coat. Technol. 115 (1999) 103–110.
[13] K. Kawata, H. Sugimura, O. Takai, Thin Solid Films 407 (2002) 38–44.
[14] S.R. Kurtz, R.G. Gordon, Thin Solid Films 140 (1986) 277–290.
[15] M.J. Buiting, A.H. Reader, MRS Online Proc. Libr. Arch, 168, 1989.
[16] M.J. Buiting, A.F. Otterloo, A.H. Montree, J. Electrochem. Soc. 138 (1991) 500–505.
[17] N. Yokoyama, J. Electrochem. Soc. 138 (1991) 190.
[18] R.I. Hegde, R.W. Fiordalice, P.J. Tobin, Appl. Phys. Lett. 62 (1993) 2326–2328.
[19] R. Leutenecker, B. Fröschle, U. Cao-Minh, P. Ramm, Thin Solid Films 270 (1995) 621–626.
[20] N. Ramanuja, R.A. Levy, S.N. Dharmadhikari, E. Ramos, C.W. Pearce, S.C. Menasian, P.C. Schamberger, C.C. Collins, Mater. Lett. 57 (2002) 261–269.
[21] J. Wagner, V. Edlmayr, M. Penoy, C. Michotte, C. Mitterer, M. Kathrein, Int. J. Refract. Met. Hard Mater. 26 (2008) 563–568.
[22] F. Teyssandier, J. Electrochem. Soc. 145 (1998) 2167.
[23] M. Stoiber, E. Badisch, C. Lugmair, C. Mitterer, Surf. Coat. Technol. 163–164 (2002) 451–456.
[24] K. Thompson, D. Lawrence, D.J. Larson, J.D. Olson, T.F. Kelly, B. Gorman, Ultramicroscopy 107 (2007) 131–139.
[25] D.R. Kingham, Surf. Sci. 116 (1982) 273–301.
[26] P. Bas, A. Bostel, B. Deconihout, D. Blavette, Appl. Surf. Sci. 87–88 (1995) 298–304.
[27] M. Thuvander, J. Weidow, J. Angseryd, L.K.L. Falk, F. Liu, M. Sonestedt, K. Stiller, H.-O. Andrén, Ultramicroscopy 111 (2011) 604–608.
[28] J. Angseryd, F. Liu, H.-O. Andrén, S.S.A. Gerstl, M. Thuvander, Ultramicroscopy 111 (2011) 609–614.
[29] V.I. Ivashchenko, P.E.A. Turchi, L.A. Ivashchenko, P.L. Skrynskii, Metall. Mater. Trans. A 37 (2006) 3391–3396.
[30] V.I. Ivashchenko, P.E.A. Turchi, V.I. Shevchenko, J. Phys. Condens. Matter 21 (2009) 395503.
[31] Z.-J. Liu, P. Leicht, Y.-X. Liu, Z.-K. Liu, Surf. Coat. Technol. 201 (2006) 2818–2821.
[32] I. Povstugar, P.-P. Choi, D. Tytko, J.-P. Ahn, D. Raabe, Acta Mater. 61 (2013) 7534–7542.
[33] P. Ettmayer, H. Kolaska, W. Lengauer, K. Dreyer, Int. J. Refract. Met. Hard Mater. 13 (1995) 343–351.
[34] E. Badisch, C. Mitterer, P.H. Mayrhofer, G. Mori, R.J. Bakker, J. Brenner, H. Störi, Thin Solid Films 460 (2004) 125–132.
[35] W. Lengauer, in: R. Riedel (Ed.), Handb. Ceram. Hard Mater, Wiley-VCH Verlag GmbH, Weinheim, Germany 2000, pp. 202–252.
[36] Q. Yang, W. Lengauer, T. Koch, M. Scheerer, I. Smid, J. Alloys Compd. 309 (2000) L5–L9.

[37] H.O. Pierson, Handb. Chem. Vap. Depos. CVD, 2nd ed. Noyes Publications, USA, Park Ridge, 1999 231–259.
[38] S. Kudapa, K. Narasimhan, P. Boppana, W.C. Russell, Surf. Coat. Technol. 120 (1999) 259–264.
[39] C. Mitterer, in: V.K. Sarin, L. Llanes, D. Mari (Eds.), Compr. Hard Mater. - Vol. 2 Ceram, Elsevier, Amsterdam 2014, pp. 449–468.
[40] P. Stender, Z. Balogh, G. Schmitz, Phys. Rev. B 83 (2011).
[41] P. Barna, M. Adamik, Thin Solid Films 317 (1998) 27–33.
[42] K. Aoki, O. Izumi, J. Jpn. Inst. Metals 43 (1979) 1190–1196.
[43] C.L. White, R.E. Clausing, L. Heatherly, Metall. Trans. A. 10 (1979) 683–691.
[44] C. Liu, C. White, J. Horton, Acta Metall. 33 (1985) 213–229.
[45] T. Takasugi, O. Izumi, N. Masahashi, Acta Metall. 33 (1985) 1259–1269.
[46] M.E. Eberhart, D.D. Vvedensky, Phys. Rev. Lett. 58 (1987) 61.
[47] J.R. Rice, J.-S. Wang, Mater. Sci. Eng. A 107 (1989) 23–40.
[48] D.A. Woodford, R.H. Bricknell, Scr. Metall. 17 (1983) 1341–1344.
[49] R. Dittmann, E. Wintermantel, T. Graule, J. Eur. Ceram. Soc. 33 (2013) 3257–3264.
[50] S. Takatsu, K. Shibuki, Thin Solid Films 127 (1985) 283–292.
[51] K. Akiyama, E. Nakamura, I. Suzuki, T. Oshika, A. Nishiyama, Y. Sawada, Surf. Coat. Technol. 94 (1997) 328–332.
[52] A.P. Katz, H.A. Lipsitt, T. Mah, M.G. Mendiratta, J. Mater. Sci. 18 (1983) 1983–1992.
[53] S.V. Dudiy, B.I. Lundqvist, Phys. Rev. B 64 (2001).

Supplementary material

Atom Probe Tomography investigations on grain boundary segregation in polycrystalline Ti(C,N) and Zr(C,N) CVD coatings

Idriss El Azhari, Jenifer Barrirero, José García, Flavio Soldera, Luis Llanes, Frank Mücklich

Atom probe tomography sample preparation

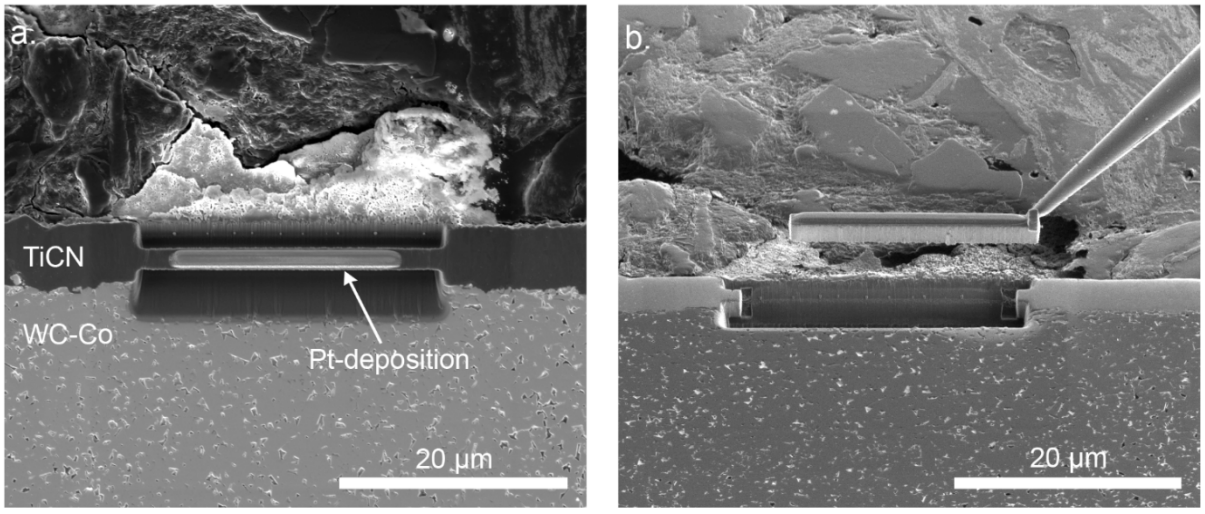

Fig. S1. SEM-FIB Lift-out at the Ti(C,N) coating for Atom Probe Tomography (a) Position of the wedge in the coating (secondary electrons image). (b) In-situ lift-out of the wedge (ions image).

Atom probe reconstruction and mass spectrum analysis

Peaks in the mass spectrum were ranged at FW10thM. In the figures below, one example of the mass spectrum for each sample with tables listing all ranged ions and compounds are presented.

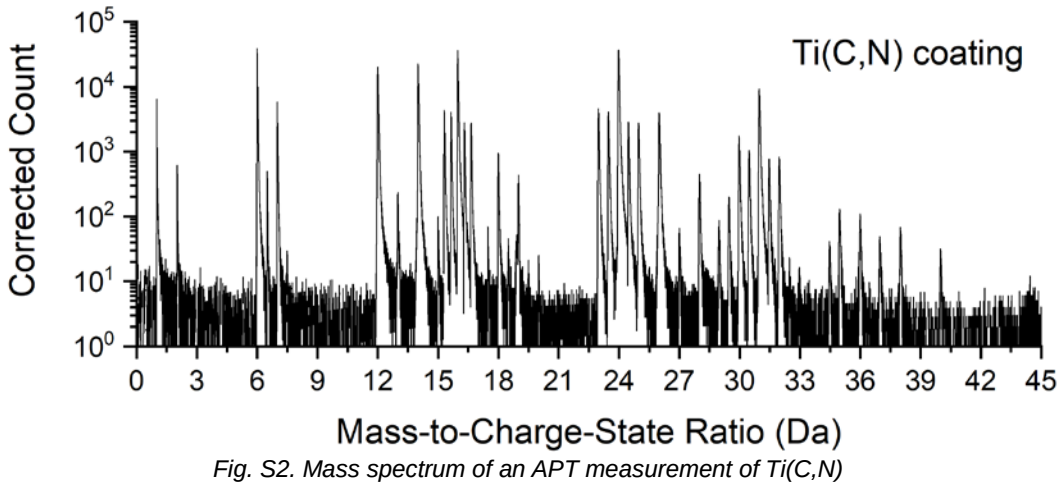

Fig. S2. Mass spectrum of an APT measurement of Ti(C,N)

Atom Probe Tomography investigations on grain boundary segregation in polycrystalline Ti(C,N) and Zr(C,N) CVD coatings (https://doi.org/10.1016/j.scriptamat.2018.11.041)

Table S1. Ti (C,N) - Ranged elements and compounds

	Charge states			Charge states	
C	+1	+2	**CN**	+1	
N	+1	+2	**C_2N**	+1	+2
Ti	+2	+3	**CN_2**	+1	+2
TiN	+2		**C_3**	+1	+2
TiO	+2		**N_2**	+1	
Co	+2		**O**	+1	
Cl	+1	+2			

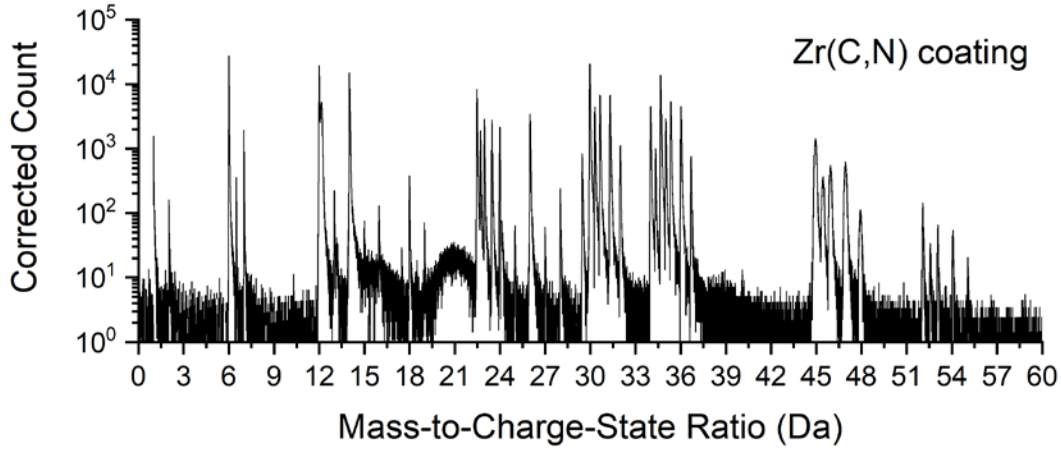

Fig. S3. Mass spectrum of an APT measurement of Zr(C,N)

Table S2. Zr (C,N) - Ranged elements and compounds

	Charge states				Charge states	
C	+1	+2		**C_4**	+2	
N	+1	+2		**Co**	+2	
Zr	+2	+3	+4	**Cl**	+2	
CN	+1			**C_2N**	+1	+2
C_2	+1			**ZrC**	+3	
C_3	+1	+2		**Ti**	+3	
ZrN	+2	+3		**ZrH**	+2	+3
N_2	+1			**H**	+1	

Elemental decomposition

Elements/compounds showing overlap in the spectrum are shown in the table below. Several overlaps are not crucial, since they involve small peaks; however, the decomposition between some overlaps such as ($Cl^{+,+2}$ / $C_3^{+,+2}$) or (N_2^+ / TiN^{+2}) for Ti(C,N); or (Zr^{+4} / C_4^{+2} / C_2^{+1}) and (ZrC^{+3} / ZrN^{+3}) are important to get more accurate results.

Table S3. Elemental decomposition Ti(C,N) Analysis

Mass-to-charge / Da	Overlaps	
18.5	**Cl (+2)**	**C_3 (+2)**
19	C_3 (+2)	C_2N (+2)
28	CN (+1)	N_2 (+1)
30	**N_2 (+1)**	**TiN (+2)**
31/31.5/32/32.5	TiO (+2)	TiN (+2)
37	**Cl (+1)**	**C_3 (+1)**
38/39	C_2N (+1)	C_3 (+1)
40/41	CN_2 (+1)	C_2N (+1)

Table S4. Elemental decomposition Zr(C,N) Analysis

Mass-to-charge / Da	Overlaps		
18.5	Cl (+2)	C_3 (+2)	
19/19.5	C_3 (+2)	C_2N (+2)	
24	**Zr (+4)**	**C_4 (+2)**	**C_2 (+1)**
25	C_4 (+2)	C_2 (+1)	
26	C_2 (+1)	CN (+1)	
30	N_2 (+1)	Zr (+3)	
30.3/30.6/31.3/32	Zr (+3)	ZrH (+3)	
34.6/35/35.3/35.6/36.6	**ZrC (+3)**	**ZrN (+3)**	
36	ZrC (+3)	ZrN (+3)	C_3 (+1)
37	ZrN (+3)	C_3 (+1)	
38/39	C_2N (+1)	C_3 (+1)	
45.5/46/47/48	Zr (+2)	ZrH (+2)	

After elemental decomposition, we performed the two corrections for carbides: **^{13}C-method** (M. Thuvander, J. Weidow, J. Angseryd, L.K.L. Falk, F. Liu, M. Sonestedt, K. Stiller, H.-O. Andrén, Ultramicroscopy 111 (2011) 604–608.) and **24 Da peak correction** (J. Angseryd, F. Liu, H.-O. Andrén, S.S.A. Gerstl, M. Thuvander, Ultramicroscopy 111 (2011) 609–614). In the former method, the $^{13}C^+$ and $^{13}C^{2+}$ isotopes are used to correct the $^{12}C^+$ and $^{12}C^{2+}$ peaks to fit the expected isotopic natural abundance. This correction compensates for the loss of counts in the ^{12}C isotope caused by the dead time of the detector during multiple events. The 24 Da peak method corrects for the peak overlap between Ti^{2+} and C_2^+ at the 24Da peak in the mass-to-charge spectrum as well as for the loss of counts due to the detector dead time. Since the Ti^{2+} isotopes at 23Da and 23.5Da do not have predicted overlaps, these peaks can be used for the peak decomposition. To correct for the loss of counts due to multiple hits, the abundance distribution between the single and multiple events at 23Da, 23.5Da and 24Da are compared and a corrected amount of multiple events at 24Da is calculated.

7.3 Paper III

Micromechanical investigations of CVD coated WC-Co cemented carbide by micropillar compression

I. El Azhari, J. García, M. Zamanzade, F. Soldera, C. Pauly, C. Motz, L. Llanes, F. Mücklich

Materials & Design. 186 (2020) 108283

https://doi.org/10.1016/j.matdes.2019.108283

Materials and Design 186 (2020) 108283

Contents lists available at ScienceDirect

Materials and Design

journal homepage: www.elsevier.com/locate/matdes

Micromechanical investigations of CVD coated WC-Co cemented carbide by micropillar compression

Idriss El Azhari [a,b,c,*], José García [d], Mohammad Zamanzade [e,f], Flavio Soldera [a,c], Christoph Pauly [a], Christian Motz [e], Luis Llanes [b], Frank Mücklich [a,c]

[a] Chair of Functional Materials, Department of Materials Science, Saarland University, Campus D 3.3, D-66123, Saarbrücken, Germany
[b] CIEFMA - Department of Materials Science and Metallurgy, Barcelona East School of Engineering (EEBE), Universitat Politècnica de Catalunya - BarcelonaTech, E-08019, Barcelona, Spain
[c] Material Engineering Center Saarland (MECS), D-66123, Saarbrücken, Germany
[d] AB Sandvik Coromant R&D, Lerkrogsvägen 19, SE-126 80, Stockholm, Sweden
[e] Chair of Materials Science and Methods, Department of Materials Science, Campus D 2.2, D-66123, Saarbrücken, Germany
[f] Mines Saint-Etienne, University of Lyon, CNRS, UMR 5307LGF, Centre SMS, F-42023, Saint-Etienne, France

HIGHLIGHTS

- During compression, stiffness of WC-Co micropillars is a convolution of elastic response and microplasticity events.
- Deformation of WC-Co micropillars depends on the microstructural assemblage and the distribution of both phases.
- Hybrid coating/substrate pillar shows enhanced micromechanical response, combining coating strength and substrate toughness.
- TiN interlayer provides excellent interfacial strength between the hardmetal substrate and the Zr(C,N) coating.

GRAPHICAL ABSTRACT

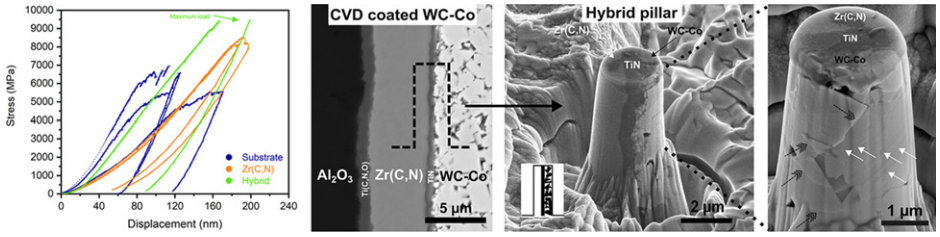

ARTICLE INFO

Article history:
Received 24 June 2019
Received in revised form 1 September 2019
Accepted 15 October 2019
Available online 21 October 2019

Keywords:
WC plasticity
Cobalt deformation
Zr(C,N) (ZrCN) CVD hard coating
TiN interlayer
Interfacial strength
EBSD

ABSTRACT

Deformation behavior of an industrial coated cemented carbide (WC-Co substrate coated with CVD multilayer of TiN/Zr(C,N)/Ti(C,N,O)/Al_2O_3) was investigated by means of micropillar compression method. In addition to the WC-Co substrate pillars, new composite pillar combination consisting of substrate, TiN interlayer and carbonitride hard coating were tested. The study targeted to document and analyze interactions between different phases and components (substrate, interlayer and coating) while subjected to compressive stress. It is found that deformation of the substrate depends mainly on the assemblage and the distribution of WC and Co phases within the pillar. The phase assemblage is subjected to changes after deformation which has an impact on the stiffness. Detailed analysis of plastic deformation within WC coarse grains pointed out that strain energy can be extensively dissipated in this phase by means of single and multiple slip. The composite/hybrid pillar formed by association of the substrate and the coating enhanced the ultimate strength in comparison to their respective individual components, highlighting the effective load-bearing response of coating and substrate acting as a coated system. This assessment was further supported by the excellent interfacial strength attested by the established TiN interlayer between the substrate and the coating.

* Corresponding author. Chair of Functional Materials, Department of Materials Science, Saarland University, Campus D 3.3, D-66123 Saarbrücken, Germany.
E-mail address: idriss.elazhari@uni-saarland.de (I. El Azhari).

https://doi.org/10.1016/j.matdes.2019.108283

1. Introduction

Developing new materials combining enhanced hardness and toughness is one of the most challenging issues for material scientists and engineers. In this regard, despite the fact that they were first introduced about one century ago [1], nowadays WC-Co cemented carbide (also referred as hardmetal in practice) remains the most successful composite material combining these two properties. Main reason behind is the optimal interface properties exhibited by the WC and cobalt couple, i.e. very low interfacial energy, nearly perfect wetting and very good adhesion in the solid state [2]. Surprisingly, it has been reported that carbide-carbide interfaces are indeed strengthened by Co segregation at the grain boundaries [3]. Furthermore, mechanical properties of these materials are widely tunable by selecting the appropriate chemical and microstructural parameters, i.e. WC grain size, metallic binder volume fraction, alloying, gradients, etc. [4]. As a result, WC-Co cemented carbides have consolidated as leading materials for manufacturing tools and components used in highly demanding applications like metal cutting or forming, mining drill bits and wear parts. From the late 60s, since the implementation of thin coatings onto cemented carbides as external layers, performance and service life of cemented carbide tools and parts were taken to a higher level and have been increasingly enhanced due to the protection offered by coatings against severe wear and significant thermo-mechanical loads [5,6]. Within this context, microstructural design optimization of substrate and coatings, as well as corresponding interlayers between them, have resulted in an ever-increasing functional performance of coated hardmetals. Extensive research has been carried out to study mechanical properties of coated systems in terms of hardness, scratch resistance, friction, wear, etc. [7]. However, only a few investigations have addressed the small-scale response of these materials regarding the local mechanical properties of their individual system components, i.e. substrate, coating and interlayer. Although nanoindentation is established as a standard and popular method to characterize mechanical properties of composite materials at the micrometer scale, multi-axial stresses and strains generated during contact loading are complex [8,9]. Accordingly, studying and analyzing the involved deformation mechanics becomes very difficult. Micro-compression emerges as a more adapted method for such micromechanical characterization, considering the relative uniform stress distribution [8] and the ease of processing micropillars. Moreover, successive annular milling of the pillars with focused ion beam (FIB) allows gradual relaxation of residual stresses [10,11]. Micropillar compression could eventually be deployed for evaluating mechanical properties such as elastic modulus and yield stress. However, special care has to be given to the experimental shortcomings which can corrupt the resulting data [12]. Still, this method has been used mainly to study single crystals and single-phased materials. Micromechanical testing of WC-Co composites is limited to few studies involving either micropillar compression [13–15], microbeam bending [16,17], micro/nano-scratch testing [18,19], or in-situ tensile testing [20,21]. Regarding micropillar compression, Csanádi et al. studied the deformation dependence upon crystal orientation for WC single crystals [13]. Similar testing approach was extended to WC-Co composites by Tarragó et al. [14] and Sandoval et al. [15], aiming to highlight yielding mechanisms within the constitutive phases and microstructural scale effects, respectively. Within the present study, the same approach was used to examine deformation behavior of a lower cobalt content WC-Co coated substrate. The post-mortem deformation was investigated using high-resolution electron microscopy and EBSD to depict microstructural changes of the different phases (WC grains and Co binder). Afterwards, micropillars milled within carbonitride coating and combined substrate/TiN-interlayer/carbonitride coating were similarly tested, and all results were compared together. In other words, complex interactions between phases (WC and Co) and different components (substrate, interlayer and coating) that likely take place under compression in real application are attempted to be replicated at the small-scale by micropillar compression. To the best knowledge of the authors, similar approach is implemented for different components of a cutting insert for the first time in this investigation. Zr(C,N) hard coating was chosen instead of the widely established Ti(C,N) due to its promising micromechanical properties [22,23], and its structural integrity when deposited on cemented carbides [24]. Besides, considering that mechanical integrity of the TiN interlayer (existing between substrate and coating) is crucial, special attention was paid to provide some insight into the interfacial strength of the system studied. Hence, the present study is divided into two main sections: investigation of deformation mechanisms of the substrate and then of the combination substrate/interlayer/coating which is here referred as a hybrid structure.

2. Materials and methods

2.1. Coated cemented carbide specimen

The investigated coated cemented carbide specimen is an industrial milling insert. It consisted of a fine grade WC-7.6 wt%Co substrate (mean carbide size of 0.8 μm) and a multilayer coating with the following upward sequence: TiN (0.3 μm), Zr(C,N) (4.5 μm), Ti(C,N,O) (0.6 μm) and α-Al_2O_3 (3 μm) as an outer layer (Fig. 1). These coatings were deposited through moderate temperature CVD process (MT-CVD) in an industrial hot wall reactor using metal chlorides precursors and temperatures ranging between 930 °C and 1000 °C. This multilayer architecture (coatings' sequence and thicknesses) is a standard sequence engineered for cemented carbides used in commercial milling inserts. The exclusive difference is the use of the recently developed Zr(C,N) wear resistant layer, instead of the widely used Ti(C,N). TiN starting interlayer is deposited on the hardmetal surface for three reasons: to promote nucleation of the carbonitride film, to act as a diffusion barrier layer and to improve adhesion to the substrate. Zr(C,N) is a hard layer intended to provide excellent combination of hardness and toughness, together with oxidation and wear resistance. Ti(C,N,O) guarantees a very good adhesion and anchoring between Zr(C,N) and alumina layer. Finally, top α-Al_2O_3 layer is a thermal barrier which mitigates both high heat flux generated during cutting and adhesive wear.

2.2. Pillar preparation

Pillars were milled in an embedded cross section of the coated cemented carbide. Cross section was prepared by grinding and polishing with diamond suspension from 9 to 1 μm. Final polishing with colloidal silica or fine alumina suspension was avoided as it has

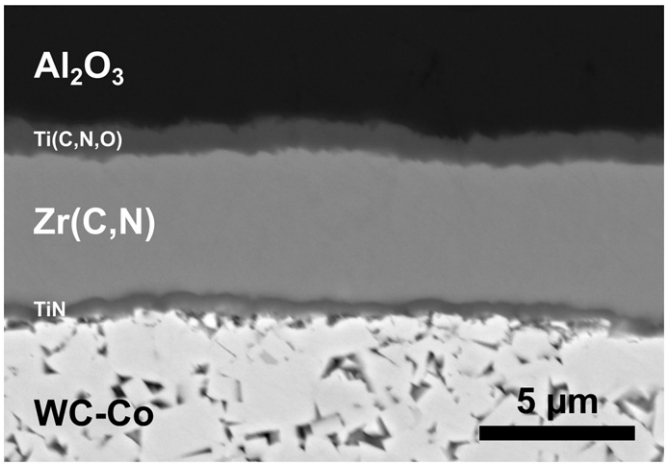

Fig. 1. Cross section of the coated cemented carbide cutting insert showing the different components.

been found to produce preferential material removal in the layers, and more noticeably in the cobalt phase, which is more pronounced for fine-grained substrate grades [25]. Then, pillars were carved on the different components of the coated insert using a FEI Helios Nanolab DualBeam 600 SEM/FIB (Scanning electron microscope/Focused ion beam) operating with gallium ion (Ga^+) beam. Three annular milling steps were conducted (with a decreasing current intensity from 21 nA, 0.92 nA and finally 0.28 nA) to achieve the final shape of the pillar with an approximate top diameter of 2 μm and an aspect ratio (diameter/height) of 1/3. Three pillars were milled from the substrate, two from Zr(C,N) and one hybrid pillar combining substrate, TiN and Zr(C,N) coating (Table 1). Diameter and taper angle of the pillars ranged between 2.1 and 2.3 μm and 4.4–5.5°, respectively. Besides, three additional hybrid pillars with an inclined interface were prepared in order to assess the interfacial strength of TiN interlayer (further details are given in section 3.2.2). Through the manuscript, "phases" refers to individual constituents within the substrate (WC, Co), and "components" refers to substrate, interlayer and coating.

Regarding pillar preparation, cross section orientation was adopted instead of the usual plain one for the following reasons:

- On a plain surface orientation, the hybrid pillar concept will be a top coating part based on a soft substrate, which will induce more deformation in the substrate. Besides, shear stress at the interface will be negligible.
- On the contrary, along the cross section, the substrate, the coating and their interfacial strength are tested, as the different stiffness exhibited by both components induces relevant shearing at interfaces. Moreover, with this orientation, different components can be investigated separately from the same prepared sample and within the same test. This is a clear advantage for reproducibility of the tests and comparison of the results.

2.3. Micro-compression tests

Micro-compression tests were carried out with the aid of a Hysitron Tribo-Indenter TI 900, equipped with a Performech controller and a 5 μm diameter diamond flat punch. Before compression, in-situ scanning probe microscopy (SPM) of the pillar with very low force and scan rate is conducted using the flat punch as a probe. The reasons behind are to precisely locate and center the flat punch relatively to the pillar and to check misalignment. The loading function is displacement controlled with a constant rate of 5 nm/s. Maximum load of the transducer that can be applied is around 35 mN. Engineering stress (ratio of applied force to top area of the pillar) and displacement were chosen as parameters for graphical representation of mechanical response, as precise determination of the actual height was highly uncertain due to irregularities around the pillar and to the uneven nature of the pillar's base surface. Therefore, by presenting displacement instead of engineering strain such source of uncertainty and error is ruled out. Moreover, due to the tapering angle, pillars do not have perfect cylindrical shape. Hence, strain is not uniform along the pillar but rather concentrated in the upper part. Dimensions of the pillars are comparable as the same milling sequence was used. Still, small variations of heights may exist, which can influence gradually the slope of stress-displacement curves. Along the manuscript, the term "stress" refers to the "engineering stress".

Table 1
Tested pillars - nomenclature used and corresponding description.

Pillar notation	Material - description
S1, S2, S3	WC-Co Substrate
C1, C2	Zr(C,N) Coating
Hybrid (Hyb)	WC-Co/TiN/Zr(C,N) - vertical interface
Hybrid-i (Hyb-i)	WC-Co/TiN/Zr(C,N) - inclined interface

2.4. Residual stresses

In coated cemented carbides, two types of residual stresses may be invoked. On one hand, CVD coatings are well-known to exhibit tensile residual stresses that are balanced by the "bulk-like" substrate. However, as small specimen micropillars are machined, these residual stresses are continuously relaxed with successive annular FIB milling to a significant extent [10,11]. On the other hand, regarding cemented carbides, there exist intrinsic residual micro-stresses between co-existing phases, i.e. WC and cobalt binder. Here, it is also known that residual stresses are compressive in the ceramic phase and tensile in the metallic one. These residual stresses do not vanish completely by FIB-milling of micropillars. However, as the study is focused on cemented carbide substrate as a "single component", such micro-residual stresses are not considered within the data analysis and beyond the scope of this investigation.

2.5. Electron backscattered diffraction (EBSD) analysis

Post-mortem EBSD analysis of a compressed pillar was conducted by extracting a thick lamella (~ 500 nm) with the FIB lift-out technique. Preparation protocol has been already detailed in a previous work by the authors [22]. In order to minimize possible damage induced by the Ga^+ ions employed, low current and acceleration voltage (11 pA and between 5 and 2 kV, respectively) were used during the final polishing of the lamella. Kikuchi patterns were obtained in reflection mode with an EDAX Hikari system at 20 kV acceleration voltage, 11 nA current and a 20 nm step size. Subsequently, raw data was processed and analyzed with OIM Analysis™ V7 software. It was implemented by defining a grain as an island of at least two adjacent points with a maximum misorientation of 5°. The confidence index (CI) was standardized across each grain to filter noise and poor data with a cut-off of CI = 0.09.

3. Results and discussion

3.1. Deformation of the substrate

3.1.1. Stress and displacement curves

Fig. 2 shows stress vs. displacement curves of the three WC-Co pillars studied. An increase in stiffness for the first 10–20 nm of displacement is noticed. This could be attributed to tiny particles trapped between the flat punch and the pillar top face or to slight misalignment induced by height difference at the top pillar surface of a couple of

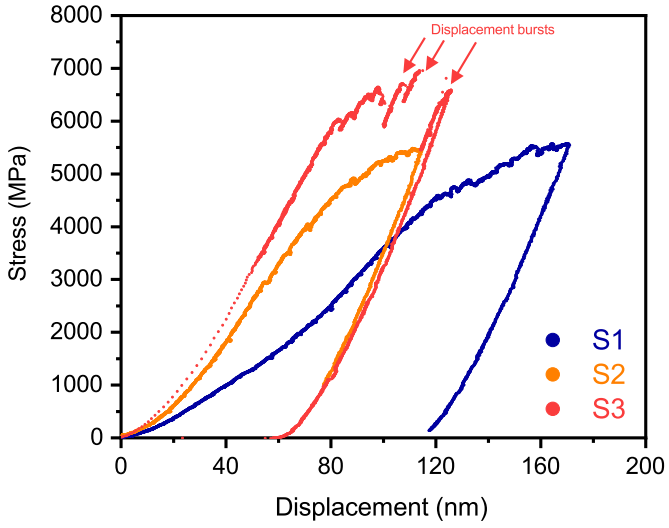

Fig. 2. Stress vs. displacement curves for substrate pillars S1, S2 and S3. Stress-displacement slope varies considerably from one pillar to another.

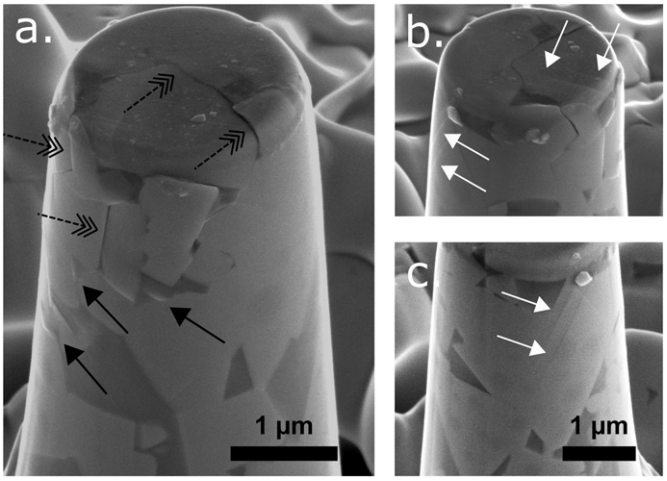

Fig. 3. Different views of yielding events in pillar S1 after compression. Dashed black arrows: WC sliding, black arrows: Cobalt extrusion and white arrows: Slip bands in WC.

nanometers. Then, during loading, the stress-displacement slope varies considerably, especially when comparing pillar S1 to pillar S3. This could be explained by considering that composite assemblage of WC grains in the Co matrix is different, regarding carbide contiguity, spatial distribution of both phases, effective grain size within the pillar and crystal orientation of carbides, in each case. As a result, each WC-Co pillar may respond to the applied strain differently [14]. However, discrepancies in stress vs. displacement response during unloading, related to the elastic recovery, are not discerned. Linear data points fitting of initial unloading segment gives the following slope values of $S_{S1} = 122$ MPa/nm, $S_{S2} = 124$ MPa/nm and $S_{S3} = 128$ MPa/nm for pillars S1, S2 and S3, respectively.

Due to the taper angle of the pillars, strain is not uniform, but rather concentrated in the top part. Pillar S1 shows extensive and multiple yielding phenomena at the top part, given in terms of binder extrusion, relative sliding between carbide grains and slip traces of single WC grains, as shown in Fig. 3. These yielding events are translated in the stress-displacement curve, where the post-initial loading segment is non-linear and is rather a mix of this complex yielding events. Hence, the term "pseudo-stiffness" will be used instead of stiffness as the response is a mixture of elasticity and micro-plasticity events. Propensity of WC to slide, rotate or plastically deform is related to the grain size and contiguity. In general, as it is also evidenced in Fig. 3, smaller carbides tend to slide and rotate, while coarser ones are prone to deform plastically through dislocation activity [26], which is obvious due to formation of slip traces. Regarding extrusion of the metallic binder, direct linking of this deformation mechanism to features within the stress-displacement curves is very difficult, as the response is a mixture of both phases where Co is restricted to smaller regions.

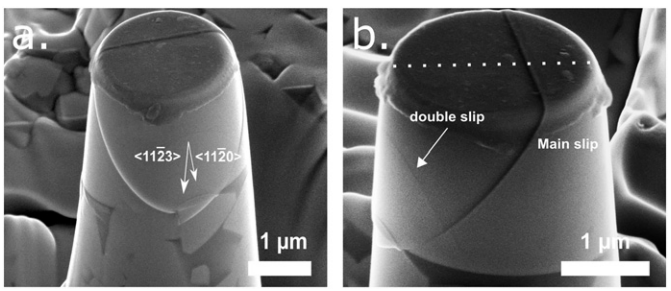

Fig. 4. (a) Front view of the pillar S3 after compression; (b) corresponding rotated view showing a crossing slip in WC phase. The dashed line marks the orientation of the extracted lamella which is perpendicular to the observed sliding.

For pillar S3, a significant sliding at the top is evidenced (Fig. 4 (a)). Moreover, from the rotated image in Fig. 4 (b), another line crossing the main sliding is observed, which could be an indication of multiple slip inside this grain. These events can be correlated to clear and discrete displacement bursts observed in the curves shown in Fig. 2, at stress levels of 6–7 GPa. This would be in agreement with previous results reported by Csanádi et al., regarding yield values of slip activation in monocrystalline WC pillars with comparable diameter to those studied here, during micro-compression testing [13]. The higher pseudo-stiffness and strength values, significant displacement bursts and the presumable slip activity discerned for pillar S3, triggered the interest for deeper investigations. A FIB lift-out is made for this pillar, then successive FIB cross-sectioning (according to the dashed line in Fig. 4 (b)) is carried out followed by high resolution SEM imaging. Fig. 5 (a) shows that the coarse WC grain in the pillar apex is supported by other WC grains, revealing then quite a high local contiguity underneath, until the base of the pillar. Hence, local assemblage could be described as a rigid continuous WC skeleton where the cobalt occupies just empty spaces between carbides. Consequently, a relatively higher pseudo-stiffness value should be expected. Aiming to gather further information, EBSD mapping was performed on multiple cross sections.

3.1.2. WC slip activity

To verify if the presumable slip in pillar S3 is actually related to dislocation activity or sliding at a grain boundary of two grains that would have perfect contiguity (Fig. 5 (b)), EBSD mapping was performed on several cross sections of the same lift-out. Several interesting observations can be stated. First, random and various orientations of different WC grains within the pillar are discerned in the inverse pole figure map (IPF) shown in Fig. 6 (a). From the same figure, it becomes clear that sliding at the pillar's top part occurred inside a single coarse grain, i.e. both sides neighboring slip trace exhibit same orientation (with a grain orientation spread of 0.35° which is close to baseline orientation noise). Second, the grain under consideration has a prismatic orientation to the plane of sectioning. In other words, the top surface of the pillar was near to parallel with the $\{10\bar{1}0\}$ type prismatic plane which is the favorable orientation for inducing slip during compression of WC single crystals [13]. In this regard, calculating the angle between the top face of the pillar and the slip trace, an approximate value of 130.5° is obtained. This value is close to the angle separating two intersecting prismatic planes (120°), considering that the disorientation of the grain toward a vertical $[10\bar{1}0]$ pole is 11° (Fig. 6 (c)). This means that the slip occurred likely along a prismatic plane. Confirmation to this statement is obtained by extracting exact orientation of the lattice and overlaying it to the image quality map in Fig. 6 (b), where the slip trace is parallel to the prismatic segment. Third, concerning the other crossing slip referred in Fig. 4 (b), its trace is not visible in the IQ map and calculation of the intersecting angle from the tilted view in Fig. 4 (b) is very difficult. Nevertheless, from its visible trace orientation, it seems that it probably arises from another prismatic plane of type $\{0\bar{1}10\}$.

In the literature, it is agreed that the predominant slip system of WC is along a prismatic plane from the family $\{10\bar{1}0\}<11\bar{2}3>$ [27–30]. Other authors have also reported $\{10\bar{1}0\}<0001>$ [26,31,32] and $\{10\bar{1}0\}<11\bar{2}0>$ system [26,32] which could dissociate into $<11\bar{2}3>$ partial dislocations [32]. Calculation of the slip direction based on the geometrical measurement of the sliding from SEM pictures is not reliable, due to the difficulty of determining the lateral displacement and to the higher measurement uncertainty. Alternatively, Schmid factor maps for the $\{10\bar{1}0\}$ slip plane were calculated (Fig. 7) for the three directions with compressive loading along the vertical axis. It appears that both $<11\bar{2}0>$ and $<11\bar{2}3>$ are very plausible directions with Schmid factor values of 0.48 and 0.38, respectively. This could lead to the conclusion that the slip took place along $<11\bar{2}0>$ direction. However, critical resolved shear stress should be taken into account to assess which of the two directions is prone to

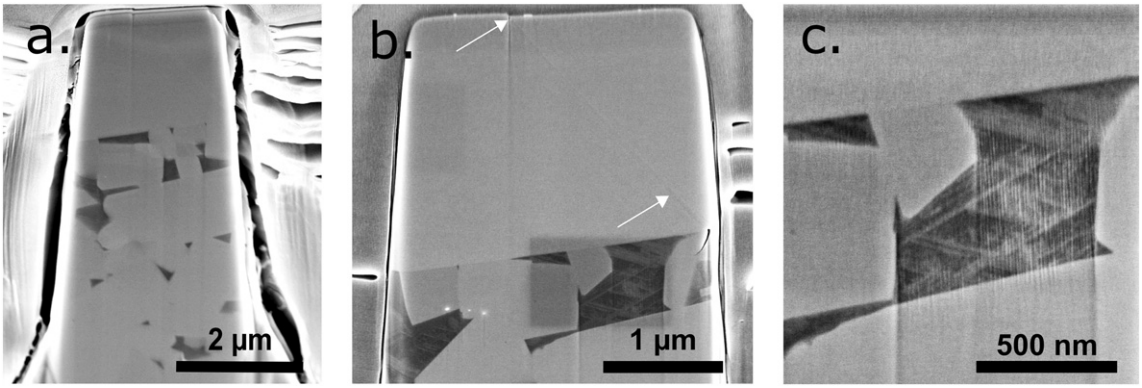

Fig. 5. (a) Post-mortem cross section at the middle of the pillar S3 showing a continuous WC skeleton from the top to the bottom of the pillar. (b) Another cross section showing smooth interface of the presumable slip plane in the top grain (white arrows). (c) Magnification of platelet structure inside the Co island showed in (b).

activate first. Fig. 4 (a) shows that there is a lateral displacement during grain slip which would not take place if the slip direction was $<11\bar{2}0>$. This directly points out $<11\bar{2}3>$ as the active slip direction in the case analyzed here.

3.1.3. Deformation of metallic binder, the cobalt phase

A larger EBSD scan (including the substrate below the pillar) was carried out in order to investigate the Co phase. In Fig. 8 (a), within the pillar, fcc-Co coexists mainly with small hcp-Co islands that are located near the interfaces of WC. Underneath the pillar, where the Co volume content and islands are larger, higher hcp fraction is noticed with direct contiguity to the carbides. This may suggest that phase transformation of Co begins at the interfaces with the carbides. Generally in cemented carbides, the dissolved W and C in the cobalt phase stabilize the fcc phase which is normally stable at higher temperatures [33,34]. It results in a predominance of the cubic phase [33], especially for fine-grained cemented carbides [35], which is the grade in this

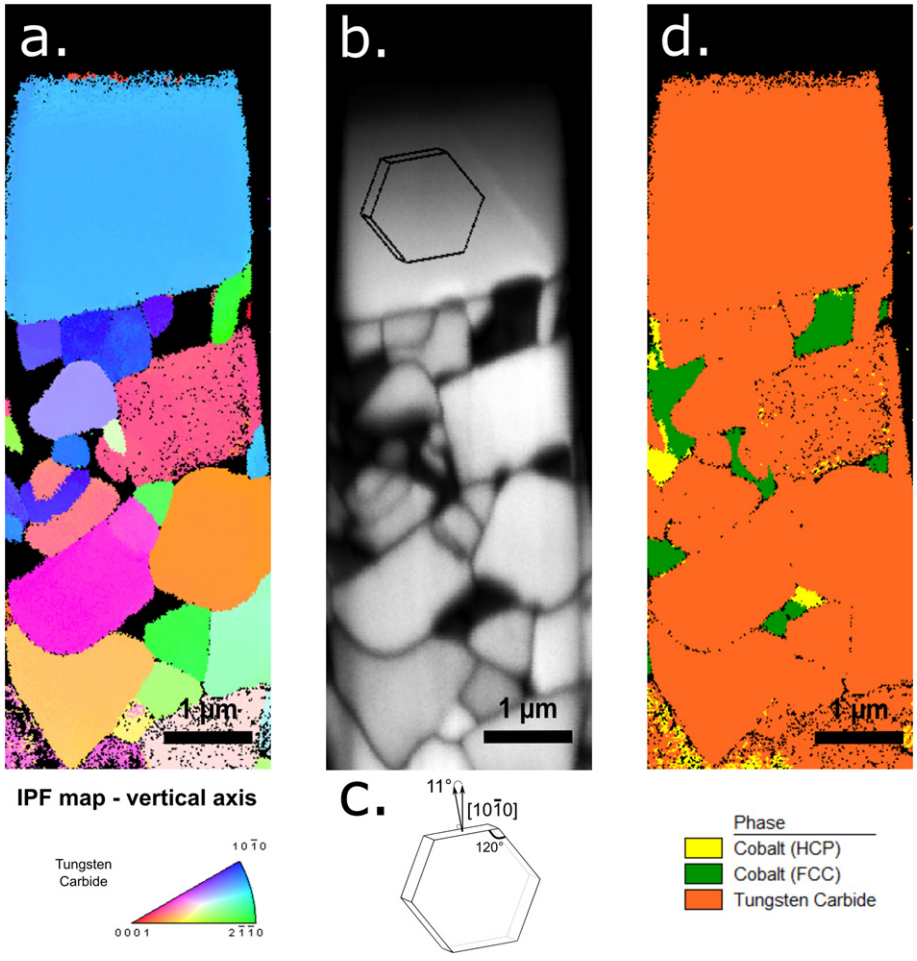

Fig. 6. (a) IPF map of the WC phase according to the vertical axis. (b) Corresponding image quality (IQ) map revealing that the slip trace in top grain is parallel to a prismatic plane. (c) Sketch of the disorientation angle between prismatic plane and the vertical axis. (d) WC and Co phase map.

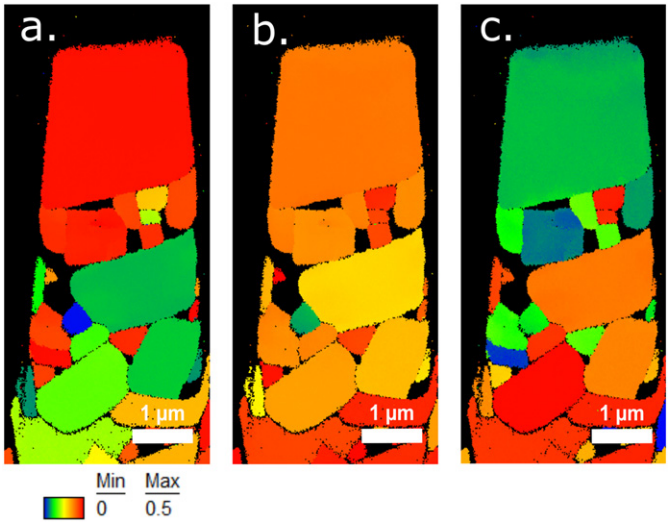

Fig. 7. Schmid factor maps of the WC phase considering the $\{10\bar{1}0\}$ slip plane according to the following directions (a) $<11\bar{2}0>$, (b) $<11\bar{2}3>$ and (c) <0001>.

study. Presence of hcp-Co phase in all the mapped cross sections (e.g. Figs. 8 and 6) could lead to the impression that phase transformation occurred during micro-compression as it is well established that Co binder endures phase transformation from fcc to hcp under strain [33,34,36,37]. Nevertheless, post treatment processes like grinding [38], substrate heating during CVD deposition and cooling down, top blasting and even lamella preparation using Ga^+ ion beam may also cause this phase transformation [39]. The latter factor could be discarded as precautions were adopted by using low acceleration voltage (between 5 and 2 kV) and low beam current at the final thinning step. However, the other factors could contribute to this phase transformation. Another lift-out was made at the substrate nearby pillar S3 to inspect the non-deformed state. As a result, both phases exist prior to micro-compression testing meaning that presence of hcp-Co is not strictly related to the deformation of the pillar. High resolution SEM images reveal intersecting platelet structures inside the Co island, which are reported to be related to deformation twinning and fcc-hcp martensitic phase transformation resulting in thin hcp lamellae in a fcc cobalt matrix [33,36,40]. An example is given in Fig. 5 (b) and (c) where most of the Co underneath the coarse grain is in the form of these platelet structures. Still, these structures cannot be resolved by EBSD, and the corresponding phase map in Fig. 6 (d) reveals only the fcc matrix for this particular Co island. Higher resolution technique - like transmission electron microscope (TEM) or automated crystal orientation mapping with TEM (ACOM-TEM) - could be capable of resolving these structures. At least, with pole figures shown in Fig. 8 (b), an orientation relationship between fcc and hcp phases is highlighted, where $(0001)_{hcp}$ // $\{111\}_{fcc}$ and $<11\bar{2}0>_{hcp}$ // $<110>_{fcc}$. This relationship has been also reported in references [33,40].

As can be seen, investigation of cobalt deformation mechanisms remains a challenge especially for low Co content and fine-grained cemented carbides due to the restricted and small Co islands. The initial allotropic phases (fcc/hcp) must be predetermined or controlled in order to assess precisely the impact of deformation on the phase transformation of Co. Various causes can induce this phase transformation and not only the applied stress during micro-compression. Nevertheless, we are assuming that phase transformation is initiated at the phase boundaries with WC grains.

3.1.4. Deformation mechanisms

For cemented carbide pillars, depending on the assemblage and the distribution of both WC grains and the metallic binder, distinct cases

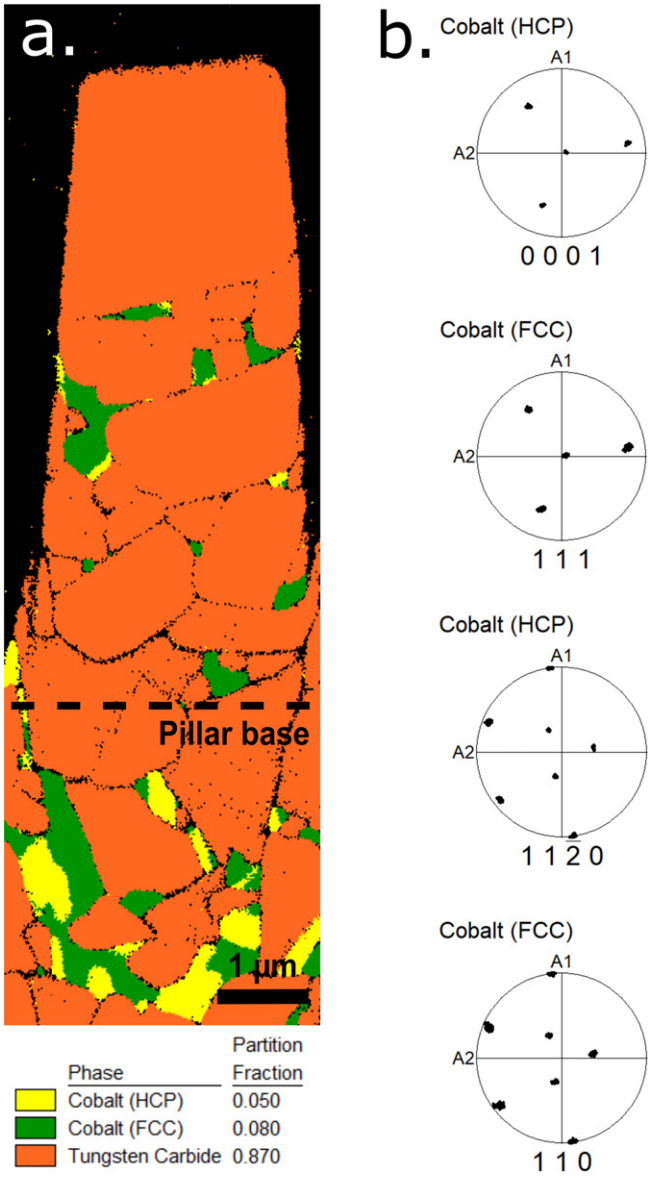

Fig. 8. (a) Phase map of pillar S3 and the substrate underneath. (b) Pole figures of Co fcc-hcp islands. An orientation relationship between fcc and hcp phases of cobalt is highlighted.

during loading stage, illustrated by pillar S1 and S3, have been demonstrated. Stress and strain concentrate at the top part as a result of the tapering angle [8]. For pillar S1 in addition to the Co flow, the upper part is composed of different WC grain sizes where the smaller ones tend to slide or rotate to each other considering that the interfaces (WC/WC and WC/Co) are preferential spots for plastic deformation [14,15]. Meanwhile, coarser grains tend to deform plastically by developing shear bands. The propensity to deform plastically with increasing grain size has been recently reported for WC-Co during indentation by Liu et al. [26] and it is generally related to the microstructural constraint or intrinsic size effect [41,42]. Meanwhile, the typical rigid WC skeleton of the carbides within pillar S3 resulted not only in higher pseudo-stiffness and strength, but also provided solid base for the top coarse grain that showcased extensive sliding. The latter is a result of multiple slips in prismatic planes followed by extensive shearing along the $\{10\bar{1}0\}<11\bar{2}3>$ slip system which is the predominant slip system for WC [27–30]. This could be described as if a single prismatic grain was compressed on the top of the supporting WC-Co pillar structure. However,

during the unloading phase, all three pillars showed similar and higher slope than their respective loading segment. The unloading segment is related to the elastic recovery and its slope is expected to be within values of single phases [14,15] where the WC is stiffer than Co. This distinct behavior of unloading stiffness increase can be also perceived in the work of Tarragò et al. [14]. In the present case, this tendency of higher and similar unloading slopes values could be explained by the attenuation or partial annihilation of the Co phase contribution, in the overall mechanical behavior, during compression. In other words, during loading, the cobalt is significantly deformed as it is the softest phase, and for instance, Co extrusion in pillar S1 was evidenced (Fig. 3 (a)). Moreover, Co phase is dispersed and restricted to small areas between bigger and harder WC grains. These are moving and sliding along with irreversible Co deformation until the formation of a rigid skeleton where the WC have enough contiguity to start carrying the load and deform. As a result, the phase assemblage and contiguity have changed after the compression and the elastic recovery during unloading arises mainly from WC phase.

Regarding deformation of WC and Co phases within a pillar structure (or micro-compression tests of WC-Co), in contrast to the previous study by Tarragó et al. where most of the described deformation mechanisms occurred in the Co phase and at the interfaces [14], the WC hard phase is in this study strongly concerned. This could be directly correlated to the lower cobalt content in the present study (7.6 wt% versus 15 wt%). As a result, the investigated pillars reached a higher yield strength. In Table 2, it can be observed that as the Co fraction increases the yield strength decreases and vice-versa. This would be in full accordance with what has been reported by Sandoval et al., stating that the yield strength increased with higher WC volume fraction as a result of pillar size reduction [15].

3.2. Deformation of coating and hybrid pillar

3.2.1. Stress and displacement curves

Aiming to investigate deformation mechanisms of both coating and combined coating/substrate system, three additional pillars were produced and tested. Two of them were milled at the Zr(C,N) coating, whereas the other one was carved at the TiN interlayer between the coating and the substrate in order to get a hybrid specimen containing about the same volume fraction of both coating and cemented carbide (Fig. 9).

Stress vs. displacement curves of these pillars are shown in Fig. 10. Opposite to the mechanical response determined for substrate pillars, mechanical response of the coating is quite reproducible. The loading segments of the two coating curves are quite similar and unloading slopes are equal ($S_{c1}=S_{c2}=79$ MPa/nm). Furthermore, a higher yield stress around 8 GPa was reached, before the first displacement burst occurred, which corresponded to crack initiation in the top face. Continuing the compression will lead to propagation of the crack along the pillar and catastrophic failure. The ultimate strength, as compared to the other components, reached the highest value in the case of the hybrid pillar. Here, stress even exceeded 9 GPa without exhibiting a displacement burst, then a plateau was reached corresponding to the maximum load that could be applied by the transducer during the micro-compression test (~ 35 mN). Post-mortem SEM images from the coating side did not reveal a visible defect or a crack formation in the coating part. Conversely, plastic deformation phenomena, such as sliding of

Table 2
Comparison of reported WC-Co micro-compression studies. Yield strength increases inversely with Co content.

Sample	d_{WC} (μm)	Pillar diameter (μm)	Yield strength (GPa)	Reference
WC-15 wt%Co	Coarse	2.5–3	0.6–3.1	[14]
WC-11 wt%Co	1.1	1–4	2.3–7	[15]
WC-7.6 wt%Co	0.8	2.1–2.3	4–7	Present study
WC (single crystal)	-	2	6–7	[13]

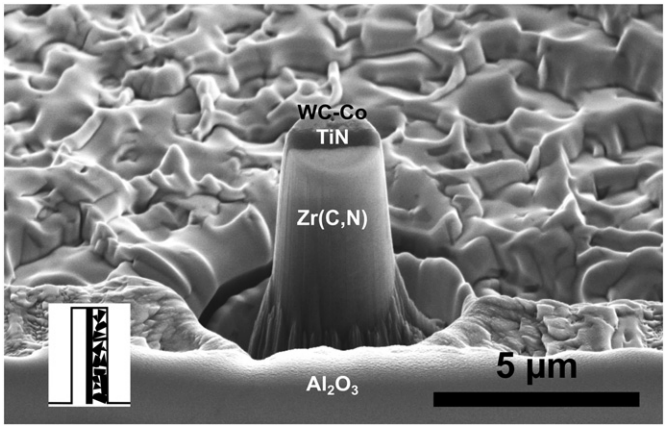

Fig. 9. Hybrid pillar carved at the interface with similar volume fraction of coating and substrate components. Inset: scheme of the components of the hybrid pillar showing (from left to right) Zr(C,N) coating, TiN interlayer and WC-Co substrate.

contiguous WC grains and slip lines within individual carbides, were discerned on the substrate side as it can be seen in Fig. 11.

Given this noticeable yielding in the substrate region in contrast to the coating in addition to the dissimilar loading behavior of these two components, significant shearing is expected at both interface sides of the TiN interlayer (substrate/TiN, TiN/coating) which would lead to interfacial failure. Yet, no decohesion or interfacial crack was evidenced in our experiments which highlights the excellent bonding properties of the TiN interlayer. Instead, the whole hybrid pillar deformed as one integral structure, and both components deformed with more leaning of the substrate part. This can be observed in Fig. 12 where SEM micrographs before and after compression were imaged with the same parameters. Accordingly, an inclination of the pillar at the substrate part is noticed. Buckling of the pillar can be caused by stability issues related to micropillar compression. Nevertheless, precautions were adopted by having an aspect ratio between 2 and 3 in addition to the absence of excessive misalignment [43]. Moreover, as this buckling concerns only this hybrid pillar, it is obvious that the heterogeneity of the structure, where the substrate side is softer than the coating, is responsible for the observed bending.

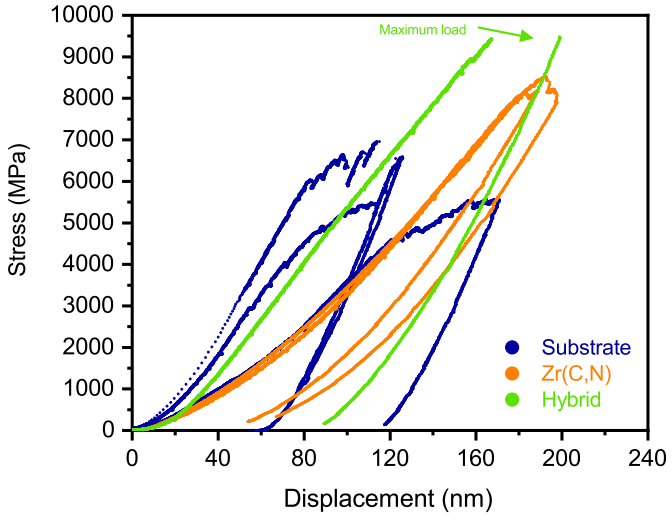

Fig. 10. Stress and displacement curves of substrate pillars (S1, S2, S3) (Yield strength ~ 4–7 GPa), Zr(C,N) coating pillars (Yield strength ~ 8 GPa), and hybrid pillar (Ultimate strength ~ 9 GPa). The plateau noticed for the hybrid pillar (green curve) is a result of reaching the maximum load of the transducer. Hybrid pillar exhibits the highest strength among all the tested specimens.

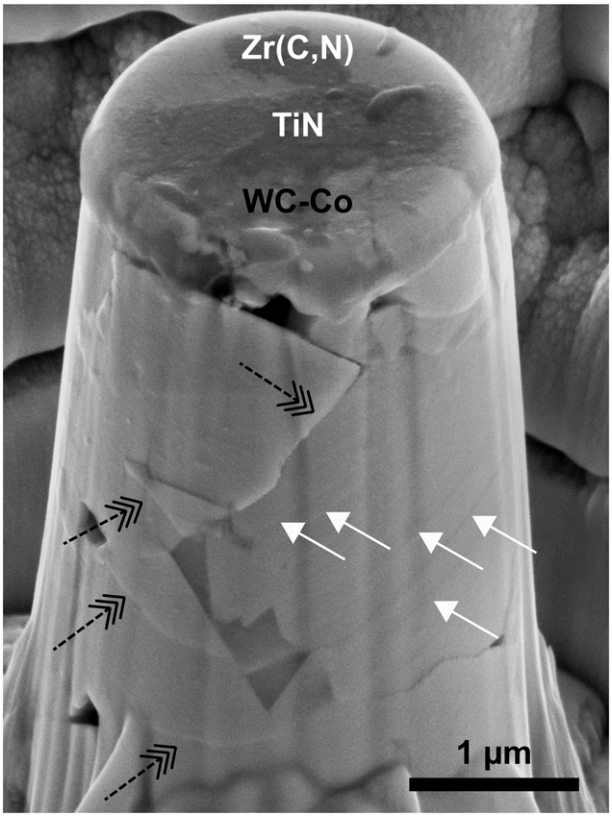

Fig. 11. Yielding events at the substrate region of the hybrid pillar: white arrows indicate slip bands in WC, while black dashed ones show sliding between WC grains.

In order to compare unloading stiffnesses between the components in Fig. 13, a rough estimate of the heights is evaluated by averaging minimum and maximum values exclusively for this purpose. It is found that the unloading stiffness of the hybrid pillar is within the values of those determined for both substrate and coating components.

To further explore the shearing resistance at the TiN interfaces, a supplementary test described below was conducted.

3.2.2. Interfacial strength at the TiN interlayer

Attempting to get further insights about interfacial strength of TiN interlayer, additional three pillars were milled at a cross section near the edge of the milling insert in order to have an inclined TiN interface trapped in sandwich between the Zr(C,N) and the substrate. The idea behind is to increase the shear stresses acting at the interfaces of the TiN during compression test. Optimal case would be to have a 45° inclination interface to maximize the shear stress. However, due to the complicated shape of the cutting insert, it is difficult to set the sample such to get the referred angle. The latter was ~ 70 ± 2° in the present study. A larger diameter (~ 3 μm) and higher aspect ratio was chosen in order to ensure that all three components will be contained (and visible) in the pillar (Fig. 14 (a)). Similar experimental protocols have been proposed and validated to calculate critical stress for shear failure of varied interfaces, e.g. between CrN coating and Si substrate [44] or between the matrix and the fiber of ceramic matrix composites [45]. Nevertheless, in the present study, the loading was a displacement-controlled function with a multicycle progressive loading, i.e. four loading-unloading cycles are applied with incremental higher displacement at each cycle. The target was to investigate occurrence of plastic deformation.

Unfortunately, before achieving pillar yielding, maximum transducer load was reached again, and the aimed critical shear stress could not be determined. Nevertheless, several important facts may be highlighted from these tests. First, failure events were not discerned at the interface. Second, as it can be seen in Fig. 14 (b), plastic deformation

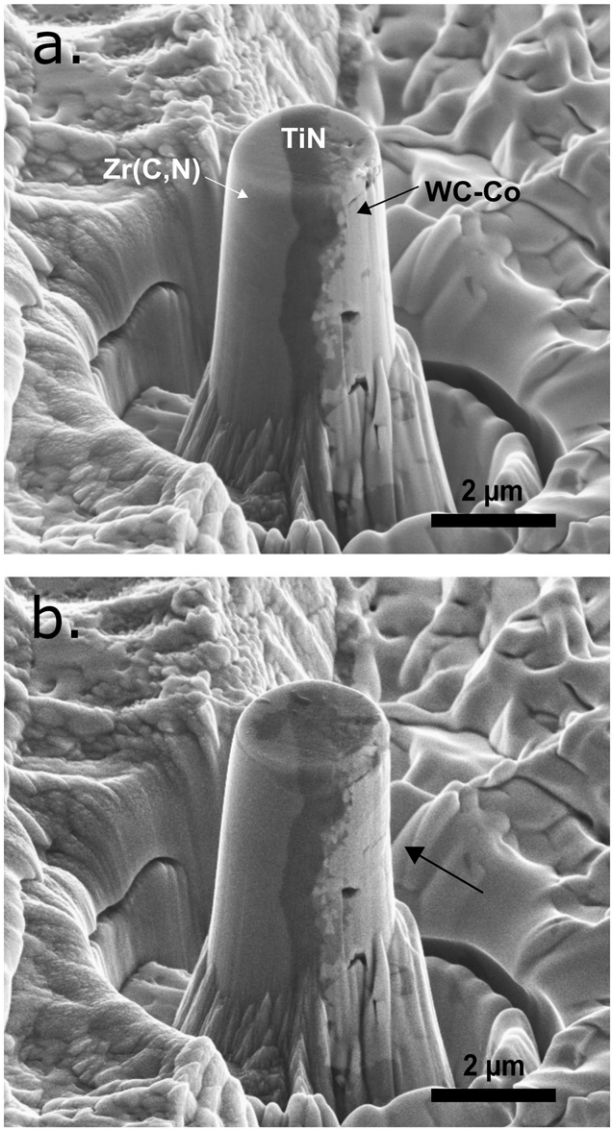

Fig. 12. (a) Side image of the hybrid pillar before compression. (b) Related post-compression image. Black arrow in (b) indicates yielding at the substrate side and leaning of the pillar to the right. This can be noticed also by taking the background surrounding the top part as a reference.

is taking place in the pillar after each cycle, as the loading and unloading segment are not similar. Third, "Pseudo-stiffness" is increasing after each loading cycle (Fig. 14 (b)), which is very similar to substrate pillars behavior in terms of unloading slope increase (Fig. 2). Accordingly, this result endorses the explanation about phase assemblage and contiguity changes of WC-Co after deformation (section 3.1.4). An approximation of the maximum shear stress which was exerted at the interface was calculated using the following formula [44,45]:

$$\tau = P \times \sin\theta \times \cos\theta / A$$

where τ: shear stress, P: maximum reached load, θ: interface angle and A: area of the pillar cross section. Estimated shear stress at the interface reached an approximate value close to 1.3 GPa, this could be taken as a lower bound estimation for its strength.

A TEM lamella was prepared in order to have a wider cross section at the TiN interface. STEM images showed absence of micro-pores or voids at TiN interfaces (Fig. 15). Furthermore, TiN presented a nanocrystalline structure with a clear contrast at the grain boundaries. This dark contrast is attributed to the segregation of diffusing substrate elements (W,Co) at

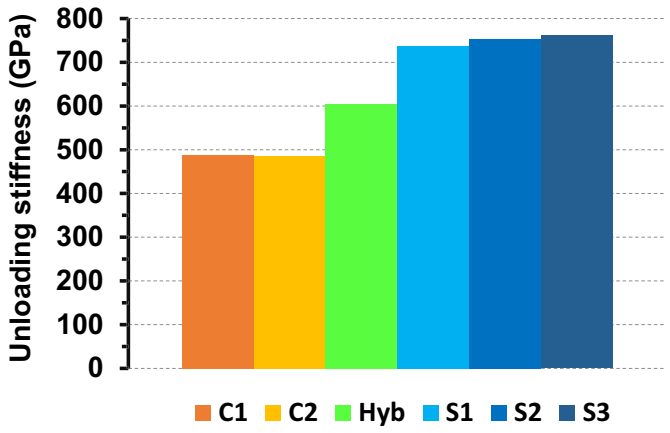

Fig. 13. Unloading stiffnesses of tested pillars, C: Coating – S: Substrate – Hyb: Hybrid. Unloading stiffness of the hybrid pillar is within the values of the corresponding components.

the grain boundaries [23,46], which are believed to enhance the adhesion of the coating [46]. As a result of the TiN nanocrystalline microstructure, no slip transmission from the WC grains to the interface is expected.

3.2.3. Strength of hybrid assemblage

The combination of coating and substrate outperformed their corresponding single component. It was seen that deformation of substrate pillars is ductile, contrary to coating one which is brittle. The hybrid pillar reached stresses as high as 9.4 GPa without showing a displacement burst and could probably advance to a superior strength if the transducer had a higher maximum load limit. The three components have deformed together, WC grains in the substrate deformed plastically, whereas the TiN and the Zr(C,N) hard coating bended with the substrate without developing a visible crack. Attention must be drawn to the fact that hybrid pillars behavior also depends on the assemblage of the substrate part. In the present case, like substrate pillar S3, coarse-grained assemblage and higher contiguity of WC grains were in favor for this superior behavior. From the coating perspective, this outstanding result could be attributed to the better cohesive strength (at grain boundaries) and ductility of Zr(C,N) in comparison with the widely used Ti(C,N) coating [22,23]. Indeed, it has to be taken into account that finer microstructure of Zr(C,N) along with TiN (within the hybrid pillar) increased volume fraction of grain boundaries in which substrate elements are segregating, and this feature may contribute to the increased strength [48]. Regarding the interfaces, no crack was evidenced at the interfaces of both components with TiN, which is a proof of the excellent interfacial strength that the TiN is guaranteeing between the cemented carbide and the hard coating. In fact, it has been reported that the addition of TiN interlayer has enhanced the adhesion strength between Ti(C,N) coating and WC-Co coating during cutting tests [46].

4. Summary

Throughout various experiments and characterization techniques the deformation mechanisms of different components of an industrial cutting insert have been investigated, the following conclusions were drawn regarding our experiments:

- Deformation of WC-Co micropillars prepared from the same substrate is strongly influenced by phase assemblage and distribution, grain size and orientation, nature of interfaces, etc., as we obtained distinct behavior during the loading of each pillar. The loading segment (or pseudo-stiffness) is a convolution of elastic response and microplasticity events. Moreover, loading and unloading behavior were dissimilar which could be explained by the local changes in phase assemblage at the end of loading segment resulting in a stiffness increase.
- In addition to the Co metallic phase, coarse WC grains can absorb considerable strain energy by deforming plastically as it has been showcased - in one example - by the extensive and multiple slip according to the established $\{10\bar{1}0\}<11\bar{2}3>$ system and initiation of several slip traces in different WC grains for the other examples.
- Investigation of cobalt phase deformation is challenging especially for low Co content and fine-grained cemented carbides. At least, we are assuming that phase transformation from fcc to hcp is initiated at the phase boundaries with WC grains.
- The hybrid pillar presented the highest strength among the tested pillars, the coating contributed with its strength while the substrate provided the necessary toughness, which enhanced its properties and outscored their individual components in terms of ultimate strength.
- Despite high shear stresses expected at interfaces of TiN interlayer during compression, the latter provided excellent interfacial strength between the substrate and the coating, which strengthen and bind both components together.

Data availability statement

The raw/processed data required to reproduce these findings cannot be shared at this time as the data also forms part of an ongoing study.

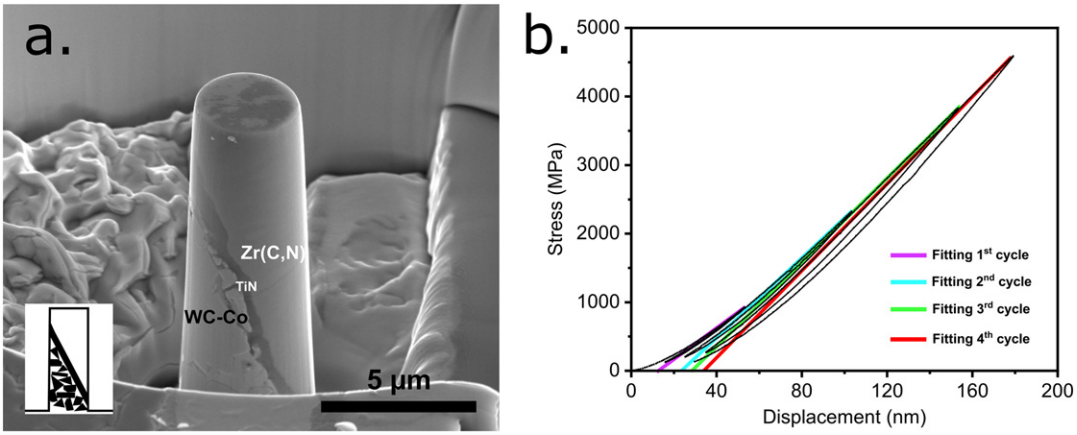

Fig. 14. a. Hybrid pillar with an inclined interface (Hyb-i) after compression. Inset: scheme of the hybrid pillar with an inclined interface. b. Corresponding multi-cycle stress-displacement curve highlighting plastic deformation after each cycle. Fitting of the loading's linear part is added for each cycle. Corresponding slopes are: 1st cycle = 22.4 MPa/nm; 2nd cycle = 29.3 MPa/nm; 3rd cycle = 30.9 MPa/nm; 4th cycle = 32 MPa/nm.

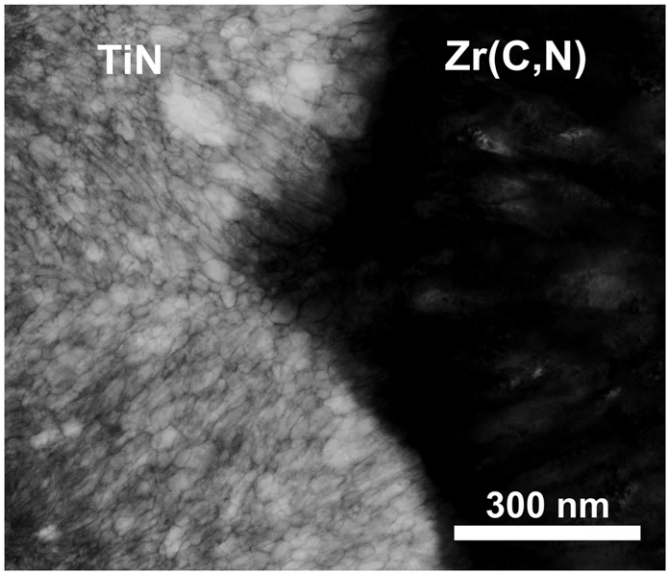

Fig. 15. Bright field STEM-in-SEM image at the TiN interface of the as-deposited state. TiN (left) and Zr(C,N) (right). Dark contrast around TiN grain boundaries denotes segregation of diffused substrate elements. Initial stages of the CVD deposition produce normally a fine-grained microstructure, and grain size will increase as the thickness increases [47].

CRediT authorship contribution statement

Idriss El Azhari: Conceptualization, Methodology, Investigation, Formal analysis, Visualization, Writing - original draft, Writing - review & editing. **José García:** Funding acquisition, Project administration, Resources, Supervision, Conceptualization, Writing - review & editing. **Mohammad Zamanzade:** Conceptualization, Investigation, Validation, Writing - review & editing. **Flavio Soldera:** Funding acquisition, Project administration, Investigation, Writing - review & editing. **Christoph Pauly:** Methodology, Investigation, Formal analysis, Validation, Writing - review & editing. **Christian Motz:** Resources, Validation, Writing - review & editing. **Luis Llanes:** Project administration, Supervision, Methodology, Conceptualization, Validation, Writing - original draft, Writing - review & editing. **Frank Mücklich:** Funding acquisition, Project administration, Resources, Supervision, Writing - review & editing.

Acknowledgement

Dr. Jeanette Persson (AB Sandvik Coromant R&D) is acknowledged for producing the coated specimens. The authors deeply acknowledge X-ray measurements performed by Sebastian Slawik (Saarland university). Dr. Florian Schäfer (Saarland University) is thanked for AFM measurements. Michael Engstler (Saarland University) is thanked for the help with image analysis. The European Commission is acknowledged for funding through the projects: Erasmus Mundus Doctoral Programme DocMASE, RISE Project CREATe-Network (No 644013) and EFRE project AME-Lab(European Regional Development Fund C/4-EFRE-13/2009/Br). AB Sandvik Coromant is acknowledged for the partial financial support of the PhD thesis (Idriss El Azhari). We acknowledge support by the Deutsche Forschungsgemeinschaft (DFG, German Research Foundation) and Saarland University within the funding programme Open Access Publishing.

References

[1] H.M. Ortner, P. Ettmayer, H. Kolaska, I. Smid, The history of the technological progress of hardmetals, Int. J. Refract. Metals Hard Mater. 49 (2015) 3–8, https://doi.org/10.1016/j.ijrmhm.2014.04.016.
[2] H.E. Exner, Physical and chemical nature of cemented carbides, Int. Met. Rev. 24 (1979) 149–173, https://doi.org/10.1179/imtr.1979.24.1.149.
[3] M. Christensen, G. Wahnström, Effects of cobalt intergranular segregation on interface energetics in WC–Co, Acta Mater. 52 (2004) 2199–2207, https://doi.org/10.1016/j.actamat.2004.01.013.
[4] J. García, V. Collado Ciprés, A. Blomqvist, B. Kaplan, Cemented carbide microstructures: a review, Int. J. Refract. Metals Hard Mater. 80 (2019) 40–68, https://doi.org/10.1016/j.ijrmhm.2018.12.004.
[5] S. Söderberg, M. Sjöstrand, B. Ljungberg, Advances in coating technology for metal cutting tools, Met. Powder Rep. 56 (2001) 24–30, https://doi.org/10.1016/S0026-0657(01)80174-0.
[6] K. Bobzin, High-performance coatings for cutting tools, CIRP J. Manuf. Sci. Technol. 18 (2017) 1–9, https://doi.org/10.1016/j.cirpj.2016.11.004.
[7] K.-D. Bouzakis, N. Michailidis, G. Skordaris, E. Bouzakis, D. Biermann, R. M'Saoubi, Cutting with coated tools: coating technologies, characterization methods and performance optimization, CIRP Ann 61 (2012) 703–723, https://doi.org/10.1016/j.cirp.2012.05.006.
[8] H. Fei, A. Abraham, N. Chawla, H. Jiang, Evaluation of micro-pillar compression tests for accurate determination of elastic-plastic constitutive relations, J. Appl. Mech. 79 (2012), 061011.
[9] M. Zamanzade, J.R. Velayarce, O.T. Abad, C. Motz, A. Barnoush, Mechanical behavior of iron aluminides: a comparison of nanoindentation, compression and bending of micropillars, Mater. Sci. Eng. A 652 (2016) 370–376, https://doi.org/10.1016/j.msea.2015.11.088.
[10] A.M. Korsunsky, M. Sebastiani, E. Bemporad, Focused ion beam ring drilling for residual stress evaluation, Mater. Lett. 63 (2009) 1961–1963, https://doi.org/10.1016/j.matlet.2009.06.020.
[11] M. Sebastiani, C. Eberl, E. Bemporad, G.M. Pharr, Depth-resolved residual stress analysis of thin coatings by a new FIB–DIC method, Mater. Sci. Eng. A 528 (2011) 7901–7908, https://doi.org/10.1016/j.msea.2011.07.001.
[12] G. Dehm, B.N. Jaya, R. Raghavan, C. Kirchlechner, Overview on micro- and nanomechanical testing: new insights in interface plasticity and fracture at small length scales, Acta Mater. 142 (2018) 248–282, https://doi.org/10.1016/j.actamat.2017.06.019.
[13] T. Csanádi, M. Bľanda, A. Duszová, N.Q. Chinh, P. Szommer, J. Dusza, Deformation characteristics of WC micropillars, J. Eur. Ceram. Soc. 34 (2014) 4099–4103, https://doi.org/10.1016/j.jeurceramsoc.2014.05.045.
[14] J.M. Tarragó, J.J. Roa, E. Jiménez-Piqué, E. Keown, J. Fair, L. Llanes, Mechanical deformation of WC–Co composite micropillars under uniaxial compression, Int. J. Refract. Metals Hard Mater. 54 (2016) 70–74, https://doi.org/10.1016/j.ijrmhm.2015.07.015.
[15] D.A. Sandoval, A. Rinaldi, J.M. Tarragó, J.J. Roa, J. Fair, L. Llanes, Scale effect in mechanical characterization of WC-Co composites, Int. J. Refract. Metals Hard Mater. 72 (2018) 157–162, https://doi.org/10.1016/j.ijrmhm.2017.12.029.
[16] M. Trueba, A. Aramburu, N. Rodríguez, I. Iparraguirre, M.R. Elizalde, I. Ocaña, J.M. Sánchez, J.M. Martínez-Esnaola, "In-situ" mechanical characterisation of WC–Co hardmetals using microbeam testing, Int. J. Refract. Metals Hard Mater. 43 (2014) 236–240, https://doi.org/10.1016/j.ijrmhm.2013.12.005.
[17] M.R. Elizalde, I. Ocaña, J. Alkorta, J.M. Sánchez-Moreno, Mechanical strength assessment of single WC-WC interfaces present in WC-Co hardmetals through microbeam bending experiments, Int. J. Refract. Metals Hard Mater. 72 (2018) 39–44, https://doi.org/10.1016/j.ijrmhm.2017.12.009.
[18] M. Gee, K. Mingard, B. Roebuck, Application of EBSD to the evaluation of plastic deformation in the mechanical testing of WC/Co hardmetal, Int. J. Refract. Metals Hard Mater. 27 (2009) 300–312, https://doi.org/10.1016/j.ijrmhm.2008.09.003.
[19] T. Csanádi, M. Novák, A. Naughton-Duszová, J. Dusza, Anisotropic nanoscratch resistance of WC grains in WC–Co composite, Int. J. Refract. Metals Hard Mater. 51 (2015) 188–191, https://doi.org/10.1016/j.ijrmhm.2015.03.005.
[20] T. Namazu, T. Morikaku, H. Akamine, T. Fujii, K. Kuroda, Y. Takami, Mechanical reliability of FIB-fabricated WC–Co cemented carbide nanowires evaluated by MEMS tensile testing, Eng. Fract. Mech. 150 (2015) 126–134, https://doi.org/10.1016/j.engfracmech.2015.07.007.
[21] X. Liu, H. Wang, L. Wang, C. Hou, X. Song, X. Liu, X. Han, In situ study of fracture behavior of ultrafine WC–Co cemented carbide, Mater. Res. Lett. 5 (2017) 55–60, https://doi.org/10.1080/21663831.2016.1208300.
[22] I. El Azhari, J. Garcia, M. Zamanzade, F. Soldera, C. Pauly, L. Llanes, F. Mücklich, Investigations on micro-mechanical properties of polycrystalline Ti(C,N) and Zr(C,N) coatings, Acta Mater. 149 (2018) 364–376, https://doi.org/10.1016/j.actamat.2018.02.053.
[23] I. El Azhari, J. Barrirero, J. García, F. Soldera, L. Llanes, F. Mücklich, Atom Probe Tomography investigations on grain boundary segregation in polycrystalline Ti(C,N) and Zr(C,N) CVD coatings, Scr. Mater. 162 (2019) 335–340, https://doi.org/10.1016/j.scriptamat.2018.11.041.
[24] I. El Azhari, J. García, F. Soldera, S. Suarez, E. Jiménez-Piqué, F. Mücklich, L. Llanes, Contact damage investigation of CVD carbonitride hard coatings deposited on cemented carbides, Int. J. Refract. Metals Hard Mater. (2019) 105050, https://doi.org/10.1016/j.ijrmhm.2019.105050.
[25] K.P. Mingard, B. Roebuck, J. Marshall, G. Sweetman, Some aspects of the structure of cobalt and nickel binder phases in hardmetals, Acta Mater. 59 (2011) 2277–2290, https://doi.org/10.1016/j.actamat.2010.12.004.
[26] X. Liu, J. Zhang, C. Hou, H. Wang, X. Song, Z. Nie, Mechanisms of WC plastic deformation in cemented carbide, Mater. Des. 150 (2018) 154–164, https://doi.org/10.1016/j.matdes.2018.04.025.
[27] S.B. Luyckx, Slip system of tungsten carbide crystals at room temperature, Acta Metall. 18 (1970) 233–236, https://doi.org/10.1016/0001-6160(70)90028-3.
[28] M.K. Hibbs, R. Sinclair, Room-temperature deformation mechanisms and the defect structure of tungsten carbide, Acta Metall. 29 (1981) 1645–1654, https://doi.org/10.1016/0001-6160(81)90047-X.
[29] V. Jayaram, R. Sinclair, D.J. Rowcliffe, Intergranular cracking in WC-6% Co: an application of the von mises criterion, Acta Metall. 31 (1983) 373–378, https://doi.org/10.1016/0001-6160(83)90214-6.

[30] T. Csanádi, M. Bl'anda, N.Q. Chinh, P. Hvizdoš, J. Dusza, Orientation-dependent hardness and nanoindentation-induced deformation mechanisms of WC crystals, Acta Mater. 83 (2015) 397–407, https://doi.org/10.1016/j.actamat.2014.09.048.
[31] J.D. Bolton, M. Redington, Plastic deformation mechanisms in tungsten carbide, J. Mater. Sci. 15 (1980) 3150–3156, https://doi.org/10.1007/BF00550388.
[32] T. Takahashi, E.J. Freise, Determination of the slip systems in single crystals of tungsten monocarbide, Philos. Mag. 12 (1965) 1–8, https://doi.org/10.1080/14786436508224941.
[33] V.K. Sarin, T. Johannesson, On the deformation of WC–Co cemented carbides, Met. Sci. 9 (1975) 472–476, https://doi.org/10.1179/030634575790444531.
[34] B. Roebuck, E.A. Almond, A.M. Cottenden, The influence of composition, phase transformation and varying the relative F.C.C. and H.C.P. phase contents on the properties of dilute Co-W-C alloys, Mater. Sci. Eng. 66 (1984) 179–194, https://doi.org/10.1016/0025-5416(84)90179-4.
[35] J.M. Marshall, M. Giraudel, The role of tungsten in the Co binder: effects on WC grain size and hcp–fcc Co in the binder phase, Int. J. Refract. Metals Hard Mater. 49 (2015) 57–66, https://doi.org/10.1016/j.ijrmhm.2014.09.028.
[36] C.H. Vasel, A.D. Krawitz, E.F. Drake, E.A. Kenik, Binder deformation in WC-(Co, Ni) cemented carbide composites, Metall. Trans. A. 16 (1985) 2309–2317, https://doi.org/10.1007/BF02670431.
[37] U. Schleinkofer, H.-G. Sockel, K. Görting, W. Heinrich, Microstructural processes during subcritical crack growth in hard metals and cermets under cyclic loads, Mater. Sci. Eng. A 209 (1996) 103–110, https://doi.org/10.1016/0921-5093(95)10098-9.
[38] J. Yang, J.J. Roa, M. Schwind, M. Odén, M.P. Johansson-Jõesaar, L. Llanes, Grinding-induced metallurgical alterations in the binder phase of WC-Co cemented carbides, Mater. Char. 134 (2017) 302–310, https://doi.org/10.1016/j.matchar.2017.11.004.
[39] H.G. Jones, A.P. Day, D.C. Cox, Electron backscatter diffraction studies of focused ion beam induced phase transformation in cobalt, Mater. Char. 120 (2016) 210–219, https://doi.org/10.1016/j.matchar.2016.09.004.
[40] X. Wu, N. Tao, Y. Hong, G. Liu, B. Xu, J. Lu, K. Lu, Strain-induced grain refinement of cobalt during surface mechanical attrition treatment, Acta Mater. 53 (2005) 681–691, https://doi.org/10.1016/j.actamat.2004.10.021.
[41] E. Arzt, Size effects in materials due to microstructural and dimensional constraints: a comparative review, Acta Mater. 46 (1998) 5611–5626.
[42] J.R. Greer, J.ThM. De Hosson, Plasticity in small-sized metallic systems: intrinsic versus extrinsic size effect, Prog. Mater. Sci. 56 (2011) 654–724, https://doi.org/10.1016/j.pmatsci.2011.01.005.
[43] H. Zhang, B.E. Schuster, Q. Wei, K.T. Ramesh, The design of accurate micro-compression experiments, Scr. Mater. 54 (2006) 181–186, https://doi.org/10.1016/j.scriptamat.2005.06.043.
[44] Y. Mu, X. Zhang, J.W. Hutchinson, W.J. Meng, Measuring critical stress for shear failure of interfacial regions in coating/interlayer/substrate systems through a micro-pillar testing protocol, J. Mater. Res. 32 (2017) 1421–1431, https://doi.org/10.1557/jmr.2016.516.
[45] C. Shih, Y. Katoh, K.J. Leonard, H. Bei, E. Lara-Curzio, Determination of interfacial mechanical properties of ceramic composites by the compression of micro-pillar test specimens, J. Mater. Sci. 48 (2013) 5219–5224, https://doi.org/10.1007/s10853-013-7311-z.
[46] K. Akiyama, E. Nakamura, I. Suzuki, T. Oshika, A. Nishiyama, Y. Sawada, A study of the adhesion between CVD layers and a cemented carbide substrate by AEM analysis, Surf. Coat. Technol. 94 (1997) 328–332.
[47] H.O. Pierson, Fundamentals of chemical vapor deposition, Handb. Chem. Vap. Depos. CVD, second ed.Park Ridge: Noyes Publications, USA 1999, pp. 36–58.
[48] S. Takatsu, K. Shibuki, Diffusion of cobalt into a TiC layer during chemical vapour deposition and its effects on the cutting performance of TiC/Al2O3-coated cemented carbides, Thin Solid Films 127 (1985) 283–292.

7.4 Paper IV

Contact damage investigation of CVD carbonitride hard coatings deposited on cemented carbides

I. El Azhari, J. García, F. Soldera, S. Suarez, E. Jiménez-Piqué, F. Mücklich, L. Llanes

Journal of Refractory Metals and Hard Materials. 86 (2020) 105050

https://doi.org/10.1016/j.ijrmhm.2019.105050

International Journal of Refractory Metals & Hard Materials 86 (2020) 105050

Contents lists available at ScienceDirect

International Journal of Refractory Metals & Hard Materials

journal homepage: www.elsevier.com/locate/IJRMHM

Contact damage investigation of CVD carbonitride hard coatings deposited on cemented carbides

I. El Azhari[a,b,c,*], J. García[d], F. Soldera[a,c], S. Suarez[a], E. Jiménez-Piqué[b], F. Mücklich[a,c], L. Llanes[b]

[a] Chair of Functional Materials, Department of Materials Science, Saarland University, Campus D 3.3, D-66123 Saarbrücken, Germany
[b] CIEFMA - Department of Materials Science and Metallurgy, Barcelona East School of Engineering (EEBE), Universitat Politècnica de Catalunya - BarcelonaTech, E-08019 Barcelona, Spain
[c] Material Engineering Center Saarland (MECS), D-66123 Saarbrücken, Germany
[d] AB Sandvik Coromant R&D, Lerkrogsvägen 19, SE-126 80 Stockholm, Sweden

ARTICLE INFO

Keywords:
Contact damage
Ti(C,N) Zr(C,N) CVD coatings
Residual stresses
X-ray synchrotron
WC-Co

ABSTRACT

The evolution of damage induced as contact load is increased has been investigated on single- and multilayered coated cemented carbides by means of spherical indentation. The main objective of the study was to assess the effect of the intermediate wear-resistant carbonitride layer on the contact damage resistance of industrial milling (multilayered) inserts. This was approached by evaluating systems consisting of a single carbonitride layer of different chemical nature: novel Zr(C,N) and conventional Ti(C,N) chemical vapor deposition (CVD) coatings. Deformation and damage phenomena were characterized using a wide range of advanced techniques: confocal laser scanning microscopy, scanning electron microscopy, focused ion beam and X-ray synchrotron. Zr(C,N) coated systems are found to exhibit a higher mechanical integrity than Ti(C,N) counterparts. Main reasons behind are the relatively different thermal residual stresses generated during CVD cooling, as a result of the dissimilar coefficient of thermal expansion between the coating and the substrate, as well as the intrinsic cohesive strength of the studied coatings. Such different mechanical response was also discerned to affect the interaction between cracking and layer assemblage in multilayer coated specimens. It then supports the beneficial effect of using Zr(C,N) as the intermediate wear-resistant layer toward enhanced performance of industrial milling inserts.

1. Introduction

WC-Co cemented carbides, also commonly referred to as hardmetals, are successful composite materials used in demanding applications like metal cutting and forming. For cutting applications, tool life and performance are significantly improved by using coatings as external protective layers, deposited by either chemical vapor (CVD) or physical vapor (PVD) deposition routes [1,2]. Wear resistant coatings are generally based on transition metal carbides, nitrides or carbonitrides, because of their hybrid ceramic and metal-like properties. This combination of characteristics has attracted considerable attention [3,4]; and thus, literature focused on development and application of these films is quite extensive (e.g. Refs. [1,5–7]). However, brittleness of these hard coatings is still an issue, and addressing this problem is a subject of high interest. In this regard, a recently developed Zr(C,N)/Al_2O_3 multilayer CVD coated milling insert has shown prolonged tool life in comparison to that exhibited by the well-established Ti(C,N)/Al_2O_3 coated inserts [8]. Aiming to get an in-depth understanding of such distinct response, a testing campaign has been launched to assess the effective influence of the carbonitride (CN) layer on the thermo-mechanical behavior of the coated tool. It has included X-ray synchrotron measurement of residual stresses developed under thermal cycling [8] as well as micromechanical characterization of polycrystalline Ti(C,N) and Zr(C,N) coatings [9,10]. In this regard, although theoretical and experimental studies dealing with mechanical properties of zirconium-based coatings are quite limited compared to titanium-based counterparts, there is a consensus that Zr(C,N) is a promising material in highly demanding applications [4,11,12].

The objective of the present study is to document and analyze the damage scenario resulting from contact loading on wear-resistant CVD hard coatings deposited on a hardmetal substrate. Referred damage is introduced in a controlled manner by means of spherical indentation. In contrast to sharp-like indenters, the use of a blunt indenter permits the delivery of concentrated stresses over a small area of specimen surface,

* Corresponding author at: Chair of Functional Materials, Department of Materials Science, Saarland University, Campus D 3.3, D-66123 Saarbrücken, Germany.
E-mail address: idriss.elazhari@uni-saarland.de (I. El Azhari).

https://doi.org/10.1016/j.ijrmhm.2019.105050
Received 5 July 2019; Received in revised form 5 August 2019; Accepted 5 August 2019
Available online 06 August 2019

such that damage evolution with increasing applied load may be assessed. Such experimental approach has proven to be successful in the evaluation of contact damage phenomena in hard and brittle bulk materials, such as ceramics [13], cemented carbides [14] and even polycrystalline diamond [15], as well as in coating-substrate systems, mainly PVD-coated hardmetals and tool steels [16–20]. Following this approach, spherical indentation experiments were conducted on specimens coated with CVD carbonitride layers of different chemical nature: Ti(C,N) and Zr(C,N). They were followed by extensive and detailed optical and scanning electron microscopy inspection of damage scenario in top- and cross-section views, i.e. at both surface and subsurface levels. Finally, findings on single-layered specimens are invoked to rationalize and understand damage features observed in industrial milling inserts (effective multilayered samples) when subjected to a similar testing protocol.

2. Materials and methods

2.1. Tested samples

The study was focused on coating/substrate systems consisting of single carbonitride [Ti(C,N)-s and Zr(C,N)-s] layers deposited onto a fine-grained WC-6wt%Co used as a substrate [2]. Films were deposited in a CVD hot wall reactor using metal chloride, acetonitrile and hydrogen reactant at temperatures between 885 and 930 °C (moderate temperature CVD process, MT-CVD). Differences between the two single-layer coated specimens studied are limited to the chemical nature of the carbonitride wear resistant layer, i.e. either Ti(C,N) or Zr(C,N). Schematic outlines of layer assemblage for the specimens investigated are given in Fig. 1, and corresponding thicknesses are listed in Table 1. Aiming to explore the practical relevance of this study, the investigation was extended to include testing of industrial milling cutting inserts. These specimens represent more complex multilayer [Ti(C,N)-m and Zr(C,N)-m] coating-substrate systems (details and corresponding layer assemblage outlines are also given in Table 1 and Fig. 1, respectively) in which an intermediate wear resistant carbonitride layer - similar to the ones tested here in single-layer coated specimens - is known to play a key role in the effective performance of the cutting tool under service conditions [8]. In this regard, it should be noticed that the thickness of single-layer variants was aimed to be close to the total thickness of the multilayer ones, i.e. 5–6 μm. It guarantees that similar coating thickness / spherical indenter radius ratios are involved during contact load tests (to be described below). However, it also implies that analysis of induced damage under contact loading should be limited to direct comparison between specimens with same layer assemblage, either single- or multilayer. Main reasons behind this statement are that both effective load-bearing and residual stress state within the carbonitride layer depend on its particular thickness, this being different in single- and multilayer assemblages which is about 5 and 3 μm, respectively.

2.2. Testing procedure

Contact loading tests of coated systems were carried out by means of spherical indentation. They were conducted using a servo-hydraulic testing machine (Instron 8500) and a hardmetal indenter with a curvature radius (r_{sph}) of 1.25 mm. Monotonic loads were applied using a trapezoidal waveform. Contact was initiated by applying a low preload (10 N), followed by load increase with a rate of 10 N/s (ramp) until reaching the selected maximum level. After holding maximum applied load during 20 s, the indenter was quickly unloaded. Maximum applied load ranged from 600 to 2400 N. Mechanical tests were conducted on specimens exhibiting two different surface topography conditions. One corresponded to “as-deposited”, i.e. surface exhibiting topography and roughness directly resulting from the coating deposition process. The other one is referred to as “polished”, i.e. the surface was previously subjected to gentle polishing with a 0.02 μm alumina suspension. This post-coating mechanical-like treatment was made attempting to enhance contact damage inspection by reducing the original roughness - of the “as-deposited” layer - that could hinder damage examination.

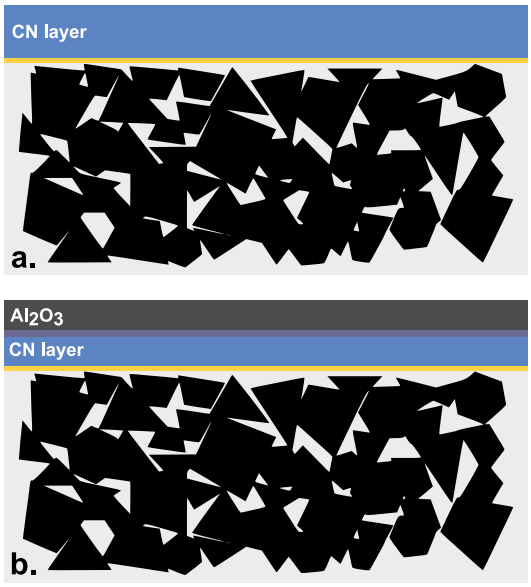

Fig. 1. Layer assemblage outline for the coating/substrate systems studied: a. Single-layer carbonitride [(C,N)-s] coated cemented carbide, including thin TiN interlayer (yellow) deposited on the substrate, prior to CN coating deposition. b. Multilayer [(C,N)-m] coated cemented carbide where in addition to referred TiN layer, a Ti(C,N,O) interlayer (dark blue) is deposited on the CN layer, prior to Al_2O_3 deposition. (For interpretation of the references to colour in this figure legend, the reader is referred to the web version of this article.)

Table 1
List of coated samples, and different corresponding layer assemblage, investigated.

Sample reference	TiN (0.3 μm)	CN Layer/ thickness	Ti(C,N,O) (0.6 μm)	α-Al_2O_3 (3 μm)
Ti(C,N)-m	✓	Ti(C,N)/3 μm	✓	✓
Zr(C,N)-m	✓	Zr(C,N)/3 μm	✓	✓
Ti(C,N)-s	✓	Ti(C,N)/5 μm	–	–
Zr(C,N)-s	✓	Zr(C,N)/5 μm	–	–

2.3. Characterization techniques

Residual imprints were characterized, in terms of dimensions and induced damage, by means of confocal laser scanning microscopy - CLSM (Olympus OLS4100). In order to assess the contact area during indentation, a sputtered gold film (about few nm in thickness) was deposited on the coated specimens before contact load testing [17]. Damage and cracking features at the subsurface were observed on cross-sections prepared using a Helios Nanolab 600 dual beam focused ion beam (FIB)/scanning electron microscopy (SEM) unit.

2.4. Residual stress measurements

Residual stresses were measured by means of X-ray diffraction, using energy-dispersive synchrotron diffraction. Measurement were performed at the Material Science Beamline EDDI (Energy Dispersive

Diffraction) of the Helmholtz-Zentrum at the storage ring BESSY in Berlin, Germany [21]. The target was to measure and analyze the residual stresses in single-layered coatings. The $\sin^2\psi$ method was used to determine residual stress values, on the basis of its numerical stability and insensitivity to experimental uncertainties.

3. Results and discussion

3.1. Single-layer coated cemented carbides: Ti(C,N)-s and Zr(C,N)-s

3.1.1. Contact damage

The induced damage was first evaluated directly at the surface, i.e. from a top-view perspective using both CLSM and SEM. In general, as maximum applied load increases, irreversible deformation of the coated system is observed through circumferential cracks at the coating surface. They were already discerned at the smallest load level applied, i.e. 600 N, for both single-layer coated specimens (Fig. 2). These cracks are induced by the tensile radial stresses and strains which increase with distance from the impression center [22], and reach maximum values near the contact edge area with the indenter [22–24]. Furthermore, radial cracks outside the imprint were also observed as an additional damage characteristic. However, different from the circular ones, these radial fissures emerge at quite different load levels, depending on the chemical nature of the carbonitride layer, i.e. 800 N for the Ti(C,N)-s specimen and barely at 2400 N for the Zr(C,N)-s one. They result from tangential tensions that develop at the periphery of the contact [25,26] at load levels higher than those usually required for promoting circumferential cracks. As imposed load increased, density and sharpness of cracks, particularly of the circumferential ones, were also higher (Fig. 2). Although clear circular-like cracks were revealed for both coatings, cracking path was more continuous for Zr(C,N)-s specimens than for Ti(C,N)-s ones, the latter exhibiting a rather disrupted aspect. This is illustrated in the closer view of induced damage shown in Fig. 3.

Within above framework, it may be stated that film cracking is governed by load transfer from the plastically deformed substrate into the coating, together with the effective fracture strength of the latter, i.e. that resulting from the compromising balance among intrinsic hardness (which is comparable between the two coatings [27]), residual stress state and mechanical integrity related to potential pre-existing cracking features. These two aspects will now be discussed.

3.1.2. Cracking-network induced after CVD cooling

As it was referred above, contact loading tests were conducted on surfaces corresponding to both “as-deposited” and “polished” conditions. As expected, mechanical response was nearly not different in both cases. However, the used testing protocol allowed us not only to visualize the damage induced after imposing load, but also to inspect surface condition of carbonitride layers before mechanical testing. Regarding the latter, it permitted to reveal a peculiar network of cracks homogeneously spread over the entire surface for Ti(C,N)-s specimen (Fig. 4a). This clearly was not the case for polished surface of Zr(C,N)-s specimen (Fig. 4b), which points out the cracking as an intrinsic result of final cooling during CVD process that follows deposition of the corresponding coatings.

Both carbonitride single layers deposited in this study exhibit a coefficient of thermal expansion (CTE) larger than that of the used hardmetal substrate (Table 2). As a consequence, coatings experience larger contractions than the substrate during cooling down after deposition. However, as a result of their corresponding dimensions, the layer has to follow the deformation of the substrate, resulting then on effective tensile loading of the coating [28]. Under high temperature deposition conditions (around 900 °C), the generated tensile stresses may exceed the coating strength, which would result in generation of a cooling cracking network that relieve the stresses [28–30]. Absence of CVD cooling cracks on the surface of “polished” Zr(C,N)-s specimen should then be attributed to the lower CTE of the layer, as compared to the one of Ti(C,N)-s sample. Therefore, CTE mismatch (with respect to the substrate) is lower in the former, and consequently the generated tensile stresses are reduced. Attention must then be drawn to the fact that Zr(C,N) exhibits the lowest CTE among all the carbonitrides of group IV [4].

An estimated value of the thermal stresses generated in the coating may be obtained according to [31]:

$$\sigma = (E_c/1 - \nu_c) \times (\alpha_c - \alpha_s) * \Delta T \quad (1)$$

where E_c, ν_c and α_c are Young's modulus, Poisson's ratio and CTE of the coating, respectively; α_s is CTE of the substrate and ΔT is the difference between room and deposition temperatures. Inserting the corresponding parameters (Table 2) within Eq. (1), thermal stress values of 1025 MPa and 1877 MPa are obtained for Zr(C,N)-s and Ti(C,N)-s specimens, respectively. Residual stresses measured by synchrotron analysis revealed notably lower mean values for Zr(C,N)-s sample (560 ± 40 MPa) and more noticeably for Ti(C,N)-s one (465 ± 30 MPa), for which the measured value is about 4 times lower than the estimated one. A plausible explanation is that stresses are relaxed after extensive cracking and formation of cooling cracks network for Ti(C,N)-s sample. Accordingly, for Zr(C,N)-s specimens, stress relaxation without extensive cracking would not be expected, considering that stresses are retained as long as the fracture strength is not reached [32]. Then, lower measured tensile stresses could be attributed to relaxation through non-elastic or plastic deformation [30]. However, this assumption should be ruled out since relaxation of around 400 MPa through namely plastic deformation appears to be unrealistic. The remaining presumption is the existence of compressive intrinsic residual stresses, which developed during deposition of the coating and prior to cooling down. For CVD thin films, possible origins of such stresses are defect incorporation into the films during evaporation, formation of non-equilibrium structures, grain boundary relaxation, etc. [30,33]. Following above ideas, the existence of prior intrinsic stresses cannot be discarded even for Ti(C,N)-s specimen. Nevertheless, a theoretical evaluation of these stresses is rather complex [33], and is out of the scope of this study.

Tensile residual stresses and cracking network resulting from CVD cooling are then aspects that may be invoked for understanding previous findings. On one hand, existence of tensile residual stresses should be responsible, at least partly, for the relatively low levels of applied load required for inducing circumferential cracking in both coated specimens. The fact that Zr(C,N)-s specimens do not show a higher cracking resistance than Ti(C,N)-s ones, as it could be expected from the relatively different calculated residual tensile stresses developed during deposition in both cases, may be rationalized by stress relief effects resulting from cracks emerging after CVD cooling stage in the latter. On the other hand, the referred CVD cooling cracking network must be directly associated with the quite early radial cracking exhibited by the Ti(C,N)-coated specimens. In this regard, it clearly affects cracking scenario resulting from both radial and circumferential stresses induced during contact load tests. Within this context, it may be postulated that bumpy crack path shown in Fig. 3a for Ti(C,N)-s specimen is indeed a consequence of the referred interaction. It reflects crack emergence from the existing CVD crack network (where cracks become thicker) and extension through effective fragmented units of the flawed layer, yielding even a visual impression of crack deflection phenomenon. As this combined action cannot exist in Zr(C,N)-s specimens, mainly because the absence of cracking event after CVD cooling stage, contact-induced fissures are discerned to follow a continuous path for these coated samples (Fig. 3b).

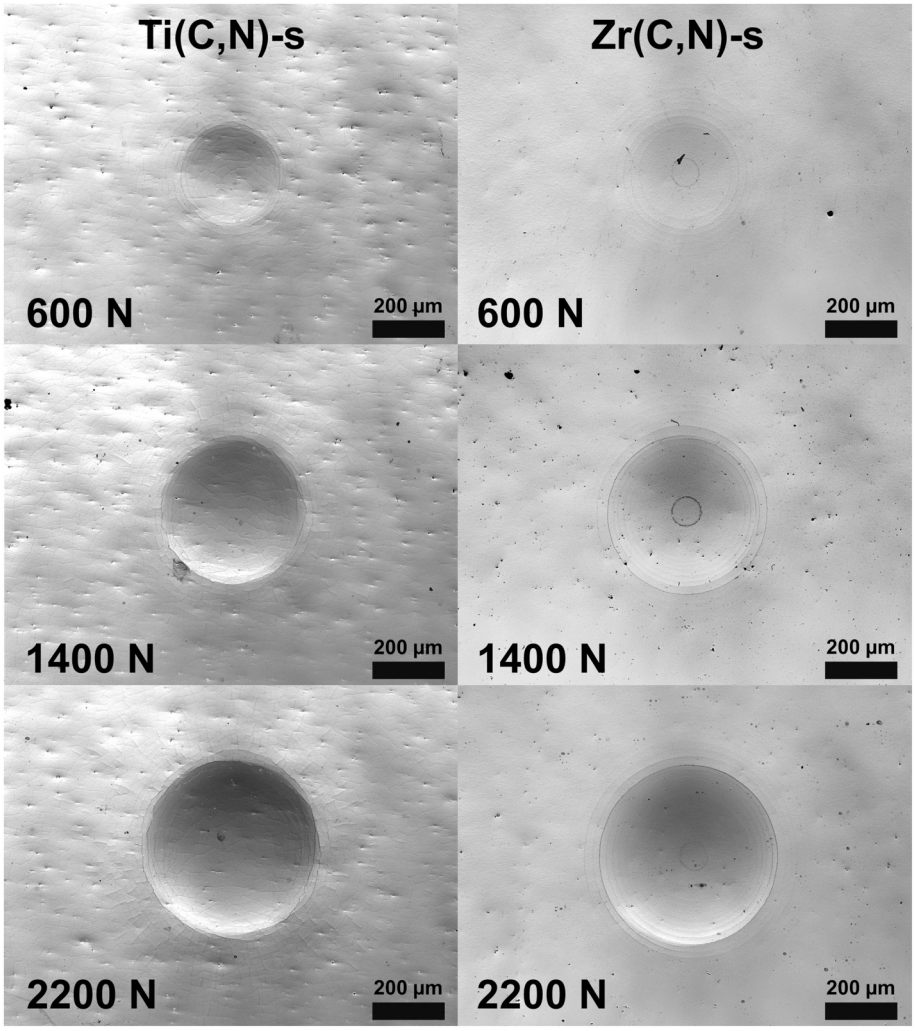

Fig. 2. Residual imprint and cracking damage evolution with increasing loads for Ti(C,N)-s and Zr(C,N)-s specimens.

3.1.3. Cracking mechanisms

Contact damage was also assessed at the subsurface level by means of cross-section inspection. It was done on FIB-milled trenches perpendicular to circular cracks. Through-thickness cracks, nucleating at the surface and propagating down into the substrate, are evidenced in both cases (Fig. 5a,b). However, crack path appears to be dissimilar: intergranular for Ti(C,N)-s specimens and transgranular for Zr(C,N)-s ones. This experimental fact is further supported by detailed in-plane SEM images of circumferential cracks taken on the surface of "as deposited" samples (Fig. 5c,d). They have permitted to evidence that

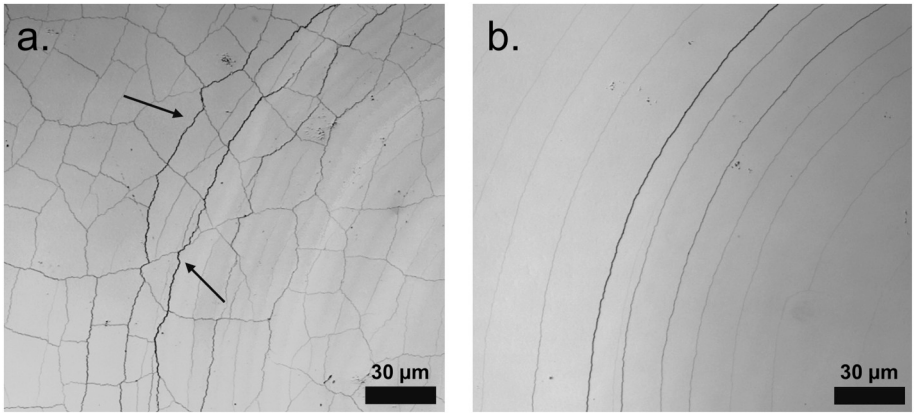

Fig. 3. Circumferential cracks induced after spherical indentation (with an applied load of 2200 N): a. choppy-like path (arrows), due to interaction with CVD cooling cracks network, in Ti(C,N)-s specimen. b. Continuous path, in absence of any CVD cooling cracks, in Zr(C,N)-s sample.

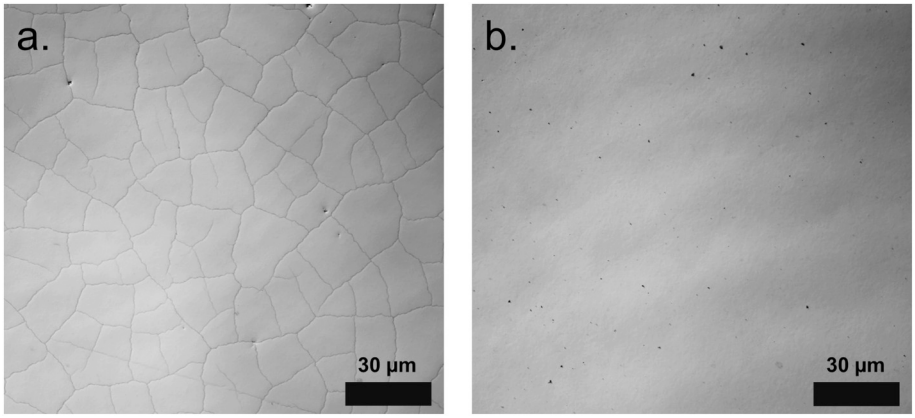

Fig. 4. a. Cracking network induced during CVD cooling observed for Ti(C,N)-s specimen after polishing. b. Absence of cooling cracks network for Zr(C,N)-s sample.

cracks propagate almost exclusively along the grain boundaries in the case of Ti(C,N)-s samples, whereas they mainly follow transgranular paths in Zr(C,N)-s ones. These results are in a complete agreement with findings previously reported by the authors regarding uniaxial compression response of micropillars milled out of same coatings studied here. There, it was evidenced that Ti(C,N) micropillars also fail exclusively along the grain boundaries, opposite to the more transgranular failure discerned for the Zr(C,N) ones [9]. This behavior was correlated to segregation of chlorine along the grain boundaries for the former, which is detrimental for the cohesive strength along the grain boundaries [10]. As a summary, the higher resistance exhibited by the Zr(C,N)-s samples may be rationalized on the basis of higher strain

Table 2
Mechanical and average thermal properties of CN coatings.

Component	E modulus (GPa)	Poisson's ratio	CTE ($10^{-6}\,K^{-1}$)	Deposition temperature (°C)
$Ti(C_{0.5*},N_{0.5*})$	463 [27]	0.193 [27]	9.2 [34]	885
$Zr(C_{0.5*},N_{0.5*})$	405 [27]	0.177 [27]	7.7 [34]	930
Substrate**	626	0.22	5.4	–

* Stoichiometry is subjected to slight variations. For more information, please refer to a recent work by the authors [10].
** Sandvik Coromant database.

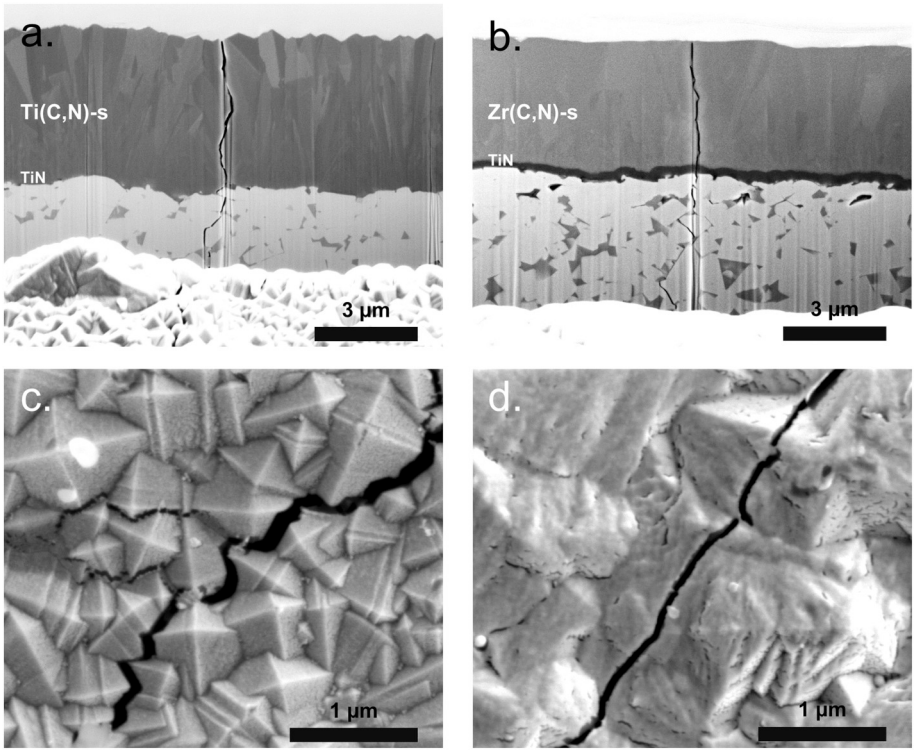

Fig. 5. a./b. FIB cross sections at circumferential cracks (located at the edge of residual imprints) induced by spherical indentation under an applied load of 2200 N for Ti(C,N)-s and Zr(C,N)-s samples, respectively. c./d. In plane SEM images of referred circumferential cracks for Ti(C,N)-s and Zr(C,N)-s specimens, respectively.

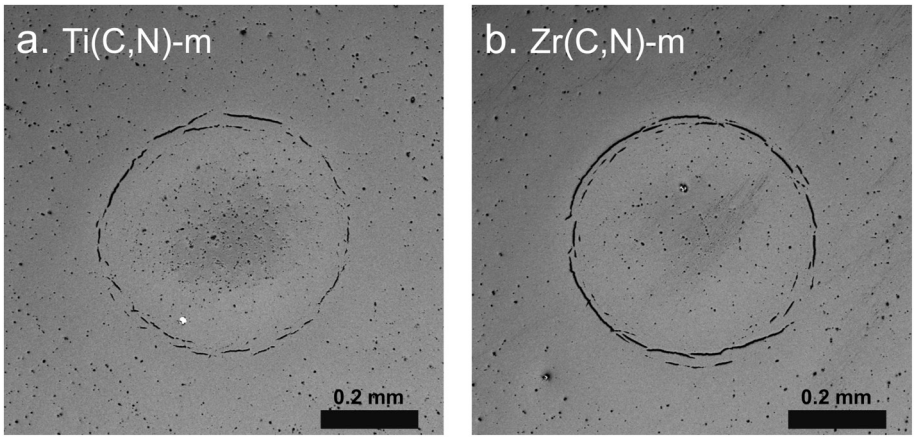

Fig. 6. Comparison of induced damage at the edges of residual imprints, revealed after polishing, for a. Ti(C,N)-m and b. Zr(C,N)-m. Applied load was 2400 N in both cases. Imprints were gently polished (after performing the test) to remove surface roughness hindering damage features. Observed surface corresponds to top Al_2O_3 layer.

energy dissipation for inducing irreversible deformation and/or damage, as compared to the Ti(C,N)-s one. For the latter, the intrinsic low cohesive strength at the grain boundaries together with the residual stress state (induced during CVD cooling) resulted in an extensive intergranular cracking network that affected the structural integrity of the Ti(C,N)-s coated system.

3.2. Multilayer coated cemented carbide: Ti(C,N)-m and Zr(C,N)-m

3.2.1. Contact damage

Multilayer coated specimens (corresponding to industrial milling inserts) were also subjected to contact loading, following testing and characterization protocols similar to the ones described above for single-layer coated systems. In general, related findings to those described for Ti(C,N)-s and Zr(C,N)-s samples were evidenced. On the one hand, as applied load was increased, circular cracks nucleated and developed at the edges of residual impressions. However, radial cracks were not discerned, at least up to highest applied load used in this study, i.e. 2400 N. On the other hand, relatively different crack paths, depending on the chemical nature of the - now - intermediate carbonitride layer involved, were discerned: nearly continuous and rather disrupted for Zr(C,N)-m and Ti(C,N)-m samples, respectively (Fig. 6). Regarding this result, cross sections for each system were performed to check whether the observed damage in Fig. 6 was resolved at the same depth level. Alumina thickness after polishing was found to be comparable, which pointed out that qualitative differences in cracking paths correspond to almost similar depth level (down from the surface). Thus, these differences may be directly ascribed to the distinct intermediate carbonitride layer, since it is the only difference existing between layer assemblages of multilayered specimens studied [Ti(C,N)-m and Zr(C,N)-m].

Inspection of FIB-milled cross-sections perpendicular to circular cracks permitted to have more insight. As shown in Fig. 7, several through-thickness cracks are evidenced. They are connected with some of the multiple small fissures discerned at the outer alumina layer. These cracks are observed to run down, following a straight path, until reaching the substrate. Density of microcracks is clearly higher in the alumina top layer than in the intermediate carbonitride ones.

3.2.2. Structural integrity of multilayer assemblage

A comparison between cracking scenario for single-layer and multilayer coated specimens is not simple. The presence of the external alpha-alumina (α-Al_2O_3) layer implies several effects. Among them, it should be highlighted that alpha-alumina exhibits higher hardness and brittleness than both CN coatings. It is noticed in Fig. 7, where multiple fine cracks are induced within the alumina as a result of spherical indentation. Furthermore, alumina top layer also presents CVD-related cracks nucleated during cooling from deposition temperature. Density and magnitude of this pre-existing cracking scenario would be directly dependent on effective tensile residual stresses induced within coatings as a result of the dissimilar CTE between the substrate and the deposited multilayers. From this viewpoint, cross-section inspection of non-tested “as-deposited” specimens (Fig. 8) indicates that it might be less developed for coated specimens involving an intermediate Zr(C,N) layer. This statement is based on the observation that cracks nucleated at the alumina surface film either do not develop into the intermediate Zr(C,N) layer or get blunted when crossing it. This is clearly not the case for Ti(C,N)-m sample. Hence, relative differences between CTEs of intermediate CN layers and the substrate, which is lower for Zr(C,N), may significantly reduce tensile stresses that drive cracks to propagate down throughout the multilayer assemblage. As a consequence, mechanical integrity got preserved for coatings including Zr(C,N) as intermediate layer. This experimental fact could then be recalled for explaining, at least partly, the different performance evaluated for industrial milling inserts as a function of the chemical nature of the used intermediate carbonitride layer.

4. Conclusions

Damage induced by spherical indentation on single- and multilayered coated cemented carbides has been studied. The more complex multilayer systems included an intermediate wear resistant carbonitride layer, similar to the ones tested here in single-layer coated specimens. The main variable under consideration is the chemical nature of the referred CN layer: Ti(C,N) or Zr(C,N). Film cracking under contact loading is governed by load transfer from the plastically deformed substrate into the coating, together with the effective fracture strength of the latter. Within this study, contact damage is assessed to depend upon the compromising balance between surface integrity (resulting from CVD process) and residual stress state, both of them linked to relative differences in CTE between coating and substrate. In this regard, in contrast to Zr(C,N)-s, Ti(C,N)-s is observed to develop a peculiar cooling cracks network fragmenting the carbonitride layer into small islands, hence damaging its structural integrity. Additionally, despite the different length scale, these contact damage tests are in a complete agreement with previous micromechanical tests in terms of crack propagation path which is intergranular for Ti(C,N)-s and mainly transgranular for Zr(C,N)-s. Such higher mechanical integrity together with higher cohesive strength at the grain boundaries may be recalled for rationalizing the enhanced performance reported for industrial milling cutting inserts containing an intermediate Zr(C,N) layer.

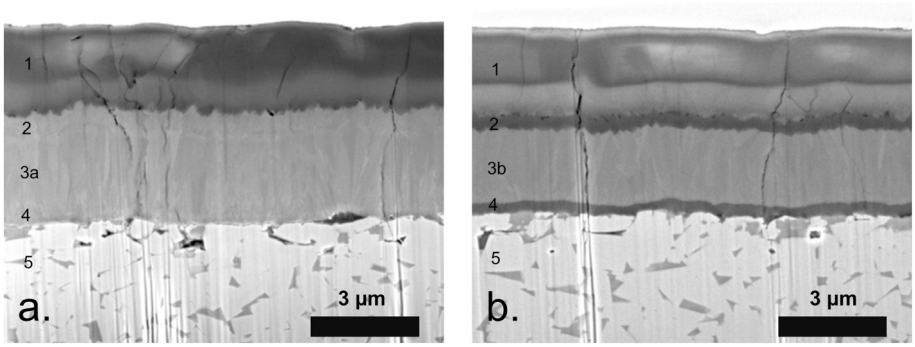

Fig. 7. FIB cross sections at circumferential cracks (located at the edge of residual imprints) induced by spherical indentation under an applied load of 2200 N (as-deposited samples): a. Ti(C,N)-m and b. Zr(C,N)-m. Numerical designation in micrographs corresponds to different layers, as follows: 1 - α-Al_2O_3; 2 - Ti(C,N,O); 3a - Ti(C,N); 3b - Zr(C,N); 4 -TiN; 5 - WC-Co substrate.

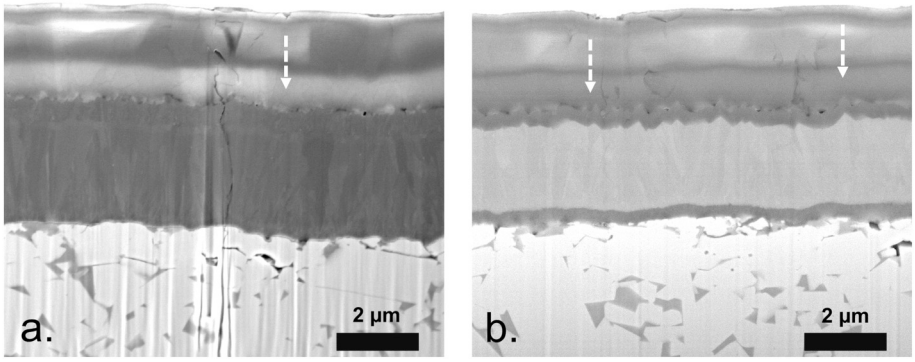

Fig. 8. FIB cross sections displaying propagation (or not) of pre-existing cracks at the Al_2O_3 top layer (induced during cooling after CVD) into intermediate CN ones for a. Ti(C,N)-m and b. Zr(C,N)-m specimens. The referred cracks appear to be stopped at the intermediate layer for Zr(C,N)-m specimen. Dashed arrow shows direction of propagation.

Acknowledgment

Dr. Jeanette Persson (AB Sandvik Coromant R&D) is acknowledged for producing the coating system layers. Dr. Fernando García Marro (CIEFMA/UPC, Barcelona), Kim Albo Selma (UPC, Barcelona) and Dr. Trifon Todorov (UPC, Barcelona) are deeply acknowledged for their assistance during contact damage testing. Dr. Christoph Pauly (Saarland university) is nicely thanked for the discussion. Mohamed Gharafi (formerly Cadi Ayyad university, Marrakesh) is thanked for finite element modeling attempts. The European Commission is acknowledged for funding through the projects: Erasmus Mundus Doctoral Programme DocMASE, RISE Project CREATe-Network (No 644013) and EFRE project AME-Lab (European Regional Development Fund C/4-EFRE-13/2009/Br). AB Sandvik Coromant is acknowledged for the partial financial support of the PhD thesis (Idriss El Azhari). German Academic Exchange Service (DAAD) and “GradUS global” program are thanked for the financial support to participate in the ICSHM11 conference.

References

[1] K.-D. Bouzakis, N. Michailidis, G. Skordaris, E. Bouzakis, D. Biermann, R. M'Saoubi, Cutting with coated tools: coating technologies, characterization methods and performance optimization, CIRP Ann. 61 (2012) 703–723, https://doi.org/10.1016/j.cirp.2012.05.006.

[2] J. García, V. Collado Ciprés, A. Blomqvist, B. Kaplan, Cemented carbide microstructures: a review, Int. J. Refract. Met. Hard Mater. 80 (2019) 40–68, https://doi.org/10.1016/j.ijrmhm.2018.12.004.

[3] L. Toth, Transition Metal Carbides and Nitrides, 1st ed, Academic Press, 1971.

[4] W. Lengauer, Transition mtal carbides, nitrides, and carbonitrides, in: R. Riedel (Ed.), Handb. Ceram. Hard Mater, Wiley-VCH Verlag GmbH, Weinheim, Germany, 2000, pp. 202–252, , https://doi.org/10.1002/9783527618217.ch7.

[5] A.T. Santhanam, Application of transition metal carbides and nitrides in industrial tools, in: S.T. Oyama (Ed.), Chem. Transit. Met. Carbides Nitrides, Springer Netherlands, Dordrecht, 1996, pp. 28–52, , https://doi.org/10.1007/978-94-009-1565-7_2.

[6] S. Söderberg, M. Sjöstrand, B. Ljungberg, Advances in coating technology for metal cutting tools, Met. Powder Rep. 56 (2001) 24–30, https://doi.org/10.1016/S0026-0657(01)80174-0.

[7] K. Bobzin, High-performance coatings for cutting tools, CIRP J. Manuf. Sci. Technol. 18 (2017) 1–9, https://doi.org/10.1016/j.cirpj.2016.11.004.

[8] J. García, M.F. Moreno, J. Östby, J. Persson, H.C. Pinto, Design of coated cemented carbides with improved comb crack resistance, Proc. 19th Plansee Semin., Reutte, Austria, 2017.

[9] I. El Azhari, J. Garcia, M. Zamanzade, F. Soldera, C. Pauly, L. Llanes, F. Mücklich, Investigations on micro-mechanical properties of polycrystalline Ti(C,N) and Zr(C,N) coatings, Acta Mater. 149 (2018) 364–376, https://doi.org/10.1016/j.actamat.2018.02.053.

[10] I. El Azhari, J. Barrirero, J. García, F. Soldera, L. Llanes, F. Mücklich, Atom probe tomography investigations on grain boundary segregation in polycrystalline Ti(C,N) and Zr(C,N) CVD coatings, Scr. Mater. 162 (2019) 335–340, https://doi.org/10.1016/j.scriptamat.2018.11.041.

[11] E. Silva, M. Rebelo de Figueiredo, R. Franz, R. Escobar Galindo, C. Palacio, A. Espinosa, S. Calderon, C. Mitterer, S. Carvalho, Structure–property relations in ZrCN coatings for tribological applications, Surf. Coat. Technol. 205 (2010) 2134–2141, https://doi.org/10.1016/j.surfcoat.2010.08.126.

[12] J. Kim, Y.J. Suh, Temperature- and pressure-dependent elastic properties, thermal expansion ratios, and minimum thermal conductivities of ZrC, ZrN, and Zr(C 0.5 N 0.5), Ceram. Int. 43 (2017) 12968–12974, https://doi.org/10.1016/j.ceramint.2017.06.195.

[13] B.R. Lawn, Indentation of ceramics with spheres: a century after hertz, J. Am. Ceram. Soc. 81 (1998) 1977–1994, https://doi.org/10.1111/j.1151-2916.1998.tb02580.x.

[14] A. Góez, D. Coureaux, A. Ingebrand, B. Reig, E. Tarrés, A. Mestra, A. Mateo, E. Jiménez-Piqué, L. Llanes, Contact damage and residual strength in hardmetals, Int. J. Refract. Met. Hard Mater. 30 (2012) 121–127, https://doi.org/10.1016/j.ijrmhm.2011.07.013.

[15] F. García-Marro, A. Mestra, V. Kanyanta, K. Maweja, S. Ozbayraktar, L. Llanes, Contact damage and residual strength in polycrystalline diamond (PCD), Diam. Relat. Mater. 65 (2016) 131–136, https://doi.org/10.1016/j.diamond.2016.03.004.

[16] E. Tarrés, G. Ramírez, Y. Gaillard, E. Jiménez-Piqué, L. Llanes, Contact fatigue behavior of PVD-coated hardmetals, Int. J. Refract. Met. Hard Mater. 27 (2009) 323–331, https://doi.org/10.1016/j.ijrmhm.2008.05.003.

[17] G. Ramírez, A. Mestra, B. Casas, I. Valls, R. Martínez, R. Bueno, A. Góez, A. Mateo, L. Llanes, Influence of substrate microstructure on the contact fatigue strength of coated cold-work tool steels, Surf. Coat. Technol. 206 (2012) 3069–3081, https://doi.org/10.1016/j.surfcoat.2011.12.012.

[18] J.J. Roa, E. Jiménez-Piqué, R. Martínez, G. Ramírez, J.M. Tarragó, R. Rodríguez, L. Llanes, Contact damage and fracture micromechanisms of multilayered TiN/CrN coatings at micro- and nano-length scales, Thin Solid Films 571 (2014) 308–315, https://doi.org/10.1016/j.tsf.2014.04.018.

[19] J. Yang, F. García Marro, T. Trifonov, M. Odén, M.P. Johansson-Jõesaar, L. Llanes, Contact damage resistance of TiN-coated hardmetals: beneficial effects associated with substrate grinding, Surf. Coat. Technol. 275 (2015) 133–141, https://doi.org/10.1016/j.surfcoat.2015.05.028.

[20] G. Ramírez, E. Jiménez-Piqué, A. Mestra, M. Vilaseca, D. Casellas, L. Llanes, A

comparative study of the contact fatigue behavior and associated damage micro-mechanisms of TiN- and WC:H-coated cold-work tool steel, Tribol. Int. 88 (2015) 263–270, https://doi.org/10.1016/j.triboint.2015.03.036.
[21] Ch. Genzel, I.A. Denks, J. Gibmeier, M. Klaus, G. Wagener, The materials science synchrotron beamline EDDI for energy-dispersive diffraction analysis, Nucl. Instrum. Methods Phys. Res. Sect. Accel. Spectrometers Detect. Assoc. Equip. 578 (2007) 23–33, https://doi.org/10.1016/j.nima.2007.05.209.
[22] J.S. Wang, Y. Sugimura, A.G. Evans, W.K. Tredway, The mechanical performance of DLC films on steel substrates, Thin Solid Films 325 (1998) 163–174, https://doi.org/10.1016/S0040-6090(98)00418-0.
[23] A. Abdul-Baqi, E. Van der Giessen, Numerical analysis of indentation-induced cracking of brittle coatings on ductile substrates, Int. J. Solids Struct. 39 (2002) 1427–1442, https://doi.org/10.1016/S0020-7683(01)00280-3.
[24] M. Kot, W. Rakowski, J.M. Lackner, Ł. Major, Analysis of spherical indentations of coating-substrate systems: experiments and finite element modeling, Mater. Des. 43 (2013) 99–111, https://doi.org/10.1016/j.matdes.2012.06.040.
[25] C.J. Studman, J.E. Field, The indentation of hard metals: the role of residual stresses, J. Mater. Sci. 12 (1977) 215–218, https://doi.org/10.1007/BF00566260.
[26] F.B. Abudaia, J.T. Evans, B.A. Shaw, Spherical indentation fatigue cracking, Mater. Sci. Eng. A 391 (2005) 181–187, https://doi.org/10.1016/j.msea.2004.08.068.
[27] Q. Yang, W. Lengauer, T. Koch, M. Scheerer, I. Smid, Hardness and elastic properties of Ti (C x N 1- x), Zr (C x N 1- x) and Hf (C x N 1- x), J. Alloys Compd. 309 (2000) L5–L9, https://doi.org/10.1016/S0925-8388(00)01057-4.
[28] H. Chien, C. Diaz-Jimenez, G.S. Rohrer, Z. Ban, P. Prichard, Y. Liu, The influence of residual thermal stresses on the mechanical properties of multilayer α-Al2O3/TiCxN1 − x coatings on WC/Co cutting tools, Surf. Coat. Technol. 215 (2013) 119–126, https://doi.org/10.1016/j.surfcoat.2012.07.088.
[29] C. Bjormander, CVD deposition and characterization of coloured Al2O3/ZrO2 multilayers, Surf. Coat. Technol. 201 (2006) 4032–4036, https://doi.org/10.1016/j.surfcoat.2006.08.035.
[30] J. García, H. Pinto, E. Ramos-Moore, C. Espinoza, J. Östby, R. Coelho, In-situ high temperature stress analysis of Ti(C,N) coatings on functionally graded cemented carbides by energy dispersive synchrotron X-ray diffraction, Int. J. Refract. Met. Hard Mater. 56 (2016) 27–34, https://doi.org/10.1016/j.ijrmhm.2015.12.001.
[31] C. Gao, Z. Zhao, X. Li, Modeling of thermal stresses in elastic multilayer coating systems, J. Appl. Phys. 117 (2015) 055305, , https://doi.org/10.1063/1.4907572.
[32] M. Gassner, N. Schalk, M. Tkadletz, C. Czettl, C. Mitterer, Thermal crack network on CVD TiCN/α-Al2O3 coated cemented carbide cutting tools, Int. J. Refract. Met. Hard Mater. 81 (2019) 1–6, https://doi.org/10.1016/j.ijrmhm.2019.02.006.
[33] M. Birkholz, C. Genzel, Residual stress analysis, Thin Film Anal. X-Ray Scatt, Wiley-VCH Verlag GmbH & Co. KGaA, Weinheim, FRG, 2006, pp. 239–295, , https://doi.org/10.1002/3527607595.ch6.
[34] K. Aigner, W. Lengauer, D. Rafaja, P. Ettmayer, Lattice parameters and thermal expansion of Ti(CxN1 − x), Zr(CxN1 − x), Hf(CxN1 − x) and TiN1 − x from 298 to 1473 K as investigated by high-temperature X-ray diffraction, J. Alloys Compd. 215 (1994) 121–126, https://doi.org/10.1016/0925-8388(94)90828-1.